Advancements in MRI-based Methods for Targeting Transcranial Focused Ultrasound

By

Sumeeth Vijay Jonathan

Dissertation

Submitted to the Faculty of the

Graduate School of Vanderbilt University

in partial fulfillment of the requirements

for the degree of

DOCTOR OF PHILOSOPHY

in

Biomedical Engineering

September 30, 2020

Nashville, Tennessee

Approved:

William A. Grissom, Ph.D. (Chair)

Charles F. Caskey, Ph.D.

Li Min Chen, M.D., Ph.D.

Dario J. Englot, M.D., Ph.D.

John C. Gore, Ph.D.

E. Duco Jansen, Ph.D.

To my parents

ACKNOWLEDGMENTS

I am grateful for so many people that have serendipitously entered my life. To Dr. Franconeri, thank you for entrusting me with ownership over the first project that I could truly call my own. I wandered into Cresap 112 twelve years ago not really knowing what research was; I left learning that it cannot be done without good mentorship. “Sumeeth – Call me Steve.” These few words left a profound impact on how I aim to act as a mentor myself one day.

To Dr. Carroll, thank you for showing me the highs – and (just as important) the lows – of a potential career in academic medicine. You taught me how to succeed as a graduate student by always treating me like one. To this day, leaving Chicago was one of the hardest decisions I have ever had to make.

To Dr. Grissom, you embody everything that a Ph.D. advisor should be. I spent the past five years working in your laboratory, but somehow you never made it feel like “work”. Thank you for always making the well-being of your students a priority – physically, mentally, and financially. I feel like graduate school was one string of excuses after another as to why I could not produce enough data; still, you never once questioned my decision to balance my dissertation project with other personal goals like clinical training and raising a family. Thank you for your patience. To Megan, Pooja, Julianna, Charlotte, Huiwen, Martin, Xinqiang, Zhipeng, Saikat, and past and future members of the Grissom Laboratory, thank you for reciprocating my looks of confusion during lab meeting when Will would go off on a spiel about something unrelated to focused ultrasound (RF pulse design, most likely). We are so fortunate to have had someone as kind as him invested in our training.

They say that if you are the smartest person in the room, you are in the wrong room. At VUIIS, then, I was always at home. To Dr. Gore, thank you for fostering an environment that puts its trainees first. You created the most collaborative place on Vanderbilt’s campus. To Tony, thank you for working in the trenches with me at the 7.0 T. You provided a breath of hilariously fresh air to countless experiments that failed to work. To Dr. Caskey, Vandiver, and Aparna, thank you for teaching me everything you know about ultrasound physics. I could not imagine a humbler group of scientists to collaborate with. To Drs. Grissom, Caskey, Chen, Gore, Englot, and Jansen, thank you for agreeing to serve on my thesis committee. I appreciate your support in me as a Ph.D. candidate and thoughtful criticisms of my dissertation project along the way.

To Melissa, thank you for always answering the phone. Your name was not on my MSTP acceptance letter, but I have no doubt in my mind that your advocacy on my behalf is the reason I am able to write this document today. To Drs. Dermody, Bills, Grundy, and Swift, thank you for taking a chance on me. I knew I was at home from the second I arrived in Nashville. To Drs. Williams (Chris & Megan), Estrada, Pozzi, Winder, York, Julie, and Bryn, thank you for investing your time in training the next generation of physician-scientists. The program I am leaving is not the same one I entered, but its culture has largely remained the same. To Pratik, Dan, Matt, and Hernan, thank you for being my de facto mentors throughout my training. Graduate school has far more documentation requirements than I was equipped to handle on my own. To Alex, Eileen, Gabby, Joey, John, Josh, Katherine, Kevin, and Shawn, it was a privilege to make this journey with you all. I am excited to see where our careers take us.

To Stephanie, before I came to Nashville, I did not imagine I would be sharing a life with you. Seven years later, I cannot imagine a life without you. There is nobody on Earth I would rather celebrate my successes and commiserate my failures with other than you. I love you, Stephanie. I will keep trying to be a better husband.

To Christopher, watching you grow up has been the greatest joy of my life. I hope that you have the opportunity to write a document like this one day. Always remember that your education is the one thing that no one can ever take away from you.

Finally, to Mom, Dad, and Sandeep, thank you for sacrificing everything for me. I am blessed to call you my family.

TABLE OF CONTENTS

Page

Chapter

LIST OF FIGURES

Chapter 1

Introduction

1.1 Synopsis

The overall goal of the work described in this dissertation is the development of improved magnetic resonance imaging (MRI)-based targeting methods for transcranial MR-guided focused ultrasound (MRgFUS). Transcranial MRgFUS is a mature technology with a number of neurological applications [1]. For example, non-invasive ablative thalamotomy is an FDA-approved treatment option for patients with essential tremor [2] or tremor-dominant Parkinsonism [3]. Recent human trials have been successful for blood-brain barrier (BBB) opening [4] and neuromodulation [5–8] via low intensity FUS.

Early efforts to deliver transcranial FUS were successfully performed through intact skull [9]. However, the widespread dissemination of this technology was limited for two reasons [10]:

1. The inability to adequately visualize the acoustic focus, and
2. The need for invasive craniotomy to overcome skull-induced aberrations.

The development of MRI-compatible, hemispherical phased array ultrasound transducers has enabled non-invasive, highly specific targeting of deep brain structures with transcranial MRgFUS [11, 12]. In addition, concurrent MRI guidance via MR thermometry pulse sequences is the standard practice for treatment monitoring during clinical ablation procedures [13, 14]. Unfortunately, established workflows for transcranial MRgFUS were largely designed for targets close to the geometric center of the brain (e.g., the thalamus) [15], where ultrasound transmission is optimal due to the incident waves being orthogonal to the skull surface. The lack of treatment monitoring strategies and aberration correction methods for off-center targets has fundamentally limited the treatment envelope of current transcranial MRgFUS targeting [16–18].

This dissertation has been structured to address these unmet needs, as follows:

Chapter 3: Volumetric thermometry with a 3D stack-of-stars echo-planar imaging (3D SoS EPI) pulse sequence. Current MR thermometry pulse sequences image temperature in a single 2D slice in order to maintain sufficient temporal resolution and temperature precision for treatment monitoring during thermal ablation. We implemented and evaluated a 3D SoS EPI pulse sequence to efficiently sample the imaged treatment volume. Volumetric temperature images are produced at frame rates as low as 0.38 s per volume using a previously validated temperature reconstruction algorithm that is tolerant to k-space undersampling.

Chapter 4: Optical tracking-guided MR-acoustic radiation force imaging (MR-ARFI) for targeting ultrasonic neuromodulation. We implemented and validated a workflow for both targeting and imaging the acoustic beam of a preclinical transcranial MRgFUS transducer prior to insonation for ultrasonic neuromodulation experiments in living non-human primates. We used optical tracking-based neuronavigation to project the expected focus location from the tracked location of the transducer relative to the subject being imaged, and used this information to plan the subsequent image acquisition of MR-ARFI scans which encode the acoustic pressure field generated by the transducer into an MR image.

Chapter 5: Rapid aberration correction of FUS acoustic pressure fields with a multi-voxel refocusing algorithm. Current MR-based refocusing algorithms require $4N$ MR-ARFI-derived intensity measurements (where N is the number of array elements) to refocus the acoustic pressure field in the presence of skull-induced aberrations, which is too long for practical in vivo use. We implemented a multi-voxel refocusing algorithm that fits a set of pre-calibrated acoustic pressure fields to the aberrated intensity measurements observed in vivo, and showed that many fewer MR-ARFI images can be used to refocus a programmatically aberrated pressure field.

Chapter 2

Magnetic resonance-guided focused ultrasound (MRgFUS)

2.1 Magnetic resonance imaging (MRI)

Atomic nuclei with an odd number of protons and/or neutrons possess a type of angular momentum called spin. These nuclei ("spins") generate a weak magnetic moment vector with a bulk magnetization that sums to zero. In the presence of an external magnetic field B_0, spins precess about B_0 at the Larmor frequency ω:

$$\omega = \gamma B_0, \tag{2.1}$$

where γ is the gyromagnetic ratio, which varies by atomic species. B_0 exerts torque on the magnetic moment of spins, which causes them to precess about the external magnetic field at the Larmor frequency like a spinning top. The interaction of the net magnetization moment vector $\mathbf{M}$ with an external magnetic field $\mathbf{B}$ is described phenomenologically by the Bloch equation:

$$\frac{d\mathbf{M}}{dt} = \mathbf{M} \times \gamma \mathbf{B} - \frac{M_x \mathbf{i} + M_y \mathbf{j}}{\mathrm{T2}} - \frac{(M_z - M_0)\mathbf{k}}{\mathrm{T1}}, \tag{2.2}$$

where M_0 is the equilibrium magnetization, and T1 and T2 are longitudinal (z) and transverse (xy) axis relaxation time constants, respectively [19]. A rotation of $\mathbf{M}$ by some angle away from the z-axis generates a component of magnetization in the transverse plane, where it is free to precess. The T1 spin-lattice time constant governs the rate of return of the magnetization to M_0 along the longitudinal axis following an excitation. It involves an exchange of thermal energy between spins and their surrounding lattice induced by dipole-dipole interactions. Conversely, the rate of decay of the transverse magnetization is characterized by the T2 spin-spin time constant, which results from local field fluctuations induced by interactions between dipoles (T2) and/or main magnetic field (B_0) inhomogeneities ($\mathrm{T2}^*$) that cause spins to precess at their own Larmor frequencies. This leads to a reduction in phase coherence between spins (dephasing), which manifests as a loss in transverse magnetization. T1 and T2 relaxation times are tissue-type specific, and thus produce image contrast in magnetic resonance imaging (MRI) [20].

The application of B_0 creates distinct energy levels populated by low energy spins that align with ($N-$) and high energy spins that align against ($N+$) the external field, according to the Boltzmann distribution:

$$\frac{N+}{N-} = e^{-\Delta E/kT} = e^{-h\frac{\gamma}{2\pi}B_0/kT}, \tag{2.3}$$

where ΔE is the energy difference between spin states, T is the temperature in Kelvin, k is Boltzmann's constant (1.38×10^{-23} J/K), and h is Planck's constant (6.63×10^{-34} J·s). At 1.0 T and 37 °C, $\frac{N+}{N-} \approx 1 - 7\times10^{-6}$ (e.g., for every 1 million spins in the high energy state, there are 1 million plus seven spins in the low energy state). One gram of H_2O contains 1 mol H_2O / 18 g H_2O × 2 mol H / 1 mol H_2O × 6.02×10^{23} protons / 1 mol H $\approx 7\times10^{22}$ hydrogen protons. In other words, a single gram of water contains $\frac{N+}{N-} \approx 2.5\times10^{17}$ or 250 million billion more protons in the low energy state than the high energy state. This large excess of spins is exploited with MR imaging. ^1H from water is the most abundant spin in the human body, and thus is encoded in most MR applications [21].

Spins exhibit resonance and undergo a transition between the two energy states when they absorb photon energy precisely equal to the energy difference between spin states (ΔE), which is determined by the Larmor frequency. For ^1H, $\gamma/2\pi$ is 42.58 MHz per Tesla. This lies in the radiofrequency (RF) range, which is non-ionizing. A time-varying RF magnetic field (B_1) is driven at the Larmor frequency to "excite" or tip spins into the transverse plane, according to Eq 2.2. Following excitation, receiver coils designed to detect magnetic flux changes in the transverse plane record a bulk time signal from a region of precessing spins. The excited spins have an amplitude distribution that is weighted by its spatial frequency content via additional magnetic gradient fields that impose a spatially-dependent frequency and phase when the signal is recorded. Thus, the recorded signal represents the 2D Fourier Transform of the excited spins at some spatial frequency. This information is used to reconstruct an MR image [22].

2.2 Ultrasound

Sound above the audible range (> 20 kHz) is called ultrasound. Like other types of acoustic waves, ultrasound is generated by mechanical disturbances that cause particles in a medium to vibrate, but with a short wavelength in tissue (about 1.5 mm at 1 MHz). Ultrasound is transmitted and received by an ultrasound transducer via piezoelectricity, which is the ability of certain materials to develop a mechanical stress in response to an applied voltage. An attractive property of piezoelectric transducers is the reciprocity of their functioning. Following ultrasound transmission, waves that are reflected back to the transducer generate an electrical signal that encodes the amplitude and phase of the received echo. Reflections from structures deep in tissue produce image contrast in ultrasound imaging [23].

In fluids, ultrasound propagates as a longitudinal wave, while other modes of propagation (e.g., shear waves) are possible in solids like bone. Longitudinal waves produce sinusoidal oscillations in the wave propagation direction:

$$u(x,t) = A\cos(kx - \omega t), \tag{2.4}$$

where A is the displacement amplitude, k is the wave number ($k = 2\pi/\lambda$ where λ is the wavelength), and ω is the angular frequency ($\omega = 2\pi f$ where f in the frequency in Hz). The phase advances by 2π radians every wavelength, which produces alternate compression (one positive half cycle of pressure) and rarefaction (negative pressure) of the particles in the same direction as the propagating wave. Moreover, ultrasound transmission is determined by the acoustic impedance Z of the supporting medium:

$$Z = \rho c, \tag{2.5}$$

where ρ is the density, and c is the sound speed. For human blood at 37 °C, c = 1584 m/s, ρ = 1.06 kg/m^3, and Z = 1.68 MRayls (1 Rayl = 1 kg/m^2/s). At a boundary where a large discontinuity in acoustic impedance is present, reflection occurs:

$$\mathrm{RF} = \frac{Z_1 - Z_2}{Z_1 + Z_2}, \tag{2.6}$$

where RF is a reflection factor for the amplitude of the reflected wave between adjacent tissues [24]. In most biological systems, air produces the largest mismatch in acoustic impedance. For example, when ultrasound propagates from blood to air in the lungs ($Z_{\mathrm{air}} = 4 \times 10^{-4}$ MRayl), $\mathrm{RF} \approx 0.99$ or

99% of the incident waves are reflected. Conversely, only 1% of ultrasound is reflected when propagating to muscle ($Z_{\text{muscle}} = 1.65$ MRayl) [25].

In diagnostic ultrasound applications, acoustic waves carry information about the body back to the imaging system consistent with the ALARA principle ("as low as reasonably achievable"). The FDA mandates limits on the maximum acoustic output levels for diagnostic ultrasound devices ($I_{\text{SPTA}} < 720$ mW/cm^2) [26]. Ultrasound-induced bioeffects like heating can be achieved with continuous-wave exposures greater than 100-1000 W/cm^2, which is exploited for non-invasive ablation treatment via high-intensity focused ultrasound (HIFU) devices [10, 15]. The biophysical basis for this and other therapeutic ultrasound applications is discussed in the next section.

2.2.1 Thermal effects

Acoustic pressure waves propagate through tissue with an incident intensity I_0 that reduces with distance z:

$$I(z) = I_0 e^{-\mu_a z}, \tag{2.7}$$

where μ_a is a tissue-specific attenuation coefficient in Np/cm. In most biological systems, attenuation is dominated by absorption. Absorption occurs due to the frictional forces present in the supporting medium which oppose the periodic motion of the moving particles exerting pressure (classical mechanism), as well as the delayed transfer of stored energy from the propagating wave to the medium (relaxation mechanism) [27]. Absorption increases with frequency f:

$$\alpha(f) = \alpha_0 f^b, \tag{2.8}$$

where α is the attenuation coefficient in dB/cm ($\alpha = 20\log(e)\mu_a \approx 8.7\mu_a$), α_0 is a tissue-specific constant, and b is a constant that is close to 1 for a range of tissue types [28]. Ultimately, some of the absorbed energy is converted to heat, which increases the temperature within the medium. In humans, bone absorbs ultrasound much more than soft tissue (e.g., 13.1 dB/cm/MHz in human skull bone vs 1.05 dB/cm/MHz in white matter) and is thus most susceptible to ultrasound-induced heating [25].

If the temperature is known, the thermal dose t_{43} can be used to predict bioeffects arising from different thermal histories:

$$t_{43} = \sum_{t=0}^{t_f} R^{43-T} \Delta t, \tag{2.9}$$

where t_f is the exposure time, T is the average temperature during time Δt, and R is a constant (R = 0.5 for $T > 43$°C and 0.25 for $T < 43$°C) [29]. A reference temperature of 43°C is typically chosen to convert different thermal exposures to "equivalent-minutes" spent at this temperature. A t_{43} of 240 minutes is the thermal dose required for total necrosis in most tissues [30].

2.2.2 Mechanical effects

2.2.2.1 Cavitation

Cavity formation in response to a time-varying acoustic pressure field is called cavitation. During rarefaction (negative pressure), the exerted pressure falls below the ambient pressure and causes cavitation nuclei (gas-filled bubbles) present in the supporting medium to expand. Bubble growth slows and is reversed during compression (positive pressure) [31]. Growth occurs if more gas diffuses into the bubble during expansion than leaves during contraction, through a process called rectified diffusion [32]. Stable cavities are bubbles that oscillate around some equilibrium size at relatively low pressures and exist for many cycles. In transcranial applications, preformed microbubbles may alter blood-brain barrier (BBB) permeability when they exhibit intravascular stable cavitation, with little effect to the surrounding brain parenchyma [33]. Conversely, transient cavities are generated by high pressures and exist for less than one cycle. These bubbles expand to many times their original size and then violently collapse, which is called inertial cavitation (a process driven by the inertia of the surrounding fluid). Inertial cavitation creates shock waves and can produce temperatures as high as 20000 °K [34].

The mechanical index (MI) was derived to predict the likelihood of cavitation events:

$$\mathrm{MI} = \frac{p_r}{\sqrt{f}}, \tag{2.10}$$

where p_r is the derated rarefactional pressure in MPa, and f is the frequency in MHz. The physical conditions to promote bubble growth are negligible when MI < 0.5 [35]. The threshold pressure for inertial cavitation decreases with both frequency and pulse duration, with bioeffects that range from no observable tissue damage (shorter pulses) to complete destruction (longer pulses) [36]. The inertial cavitation threshold is further reduced when microbubbles are present. Microbubbles also reduce the threshold for thermal damage by increasing the absorption of ultrasound in tissue [37].

2.2.2.2 Radiation force

Acoustic pressure waves, like other forms of wave motion, exert a radiation force (F) on absorbing or reflecting obstacles in their path as they propagate through tissue:

$$\mathrm{F} = \frac{2\alpha I}{c}, \tag{2.11}$$

where α is a tissue-specific attenuation coefficient, I is the temporal average intensity, and c is the speed of sound in the supporting medium. The radiation force arises when an energy gradient is produced by an attenuating medium and causes a momentum transfer from the propagating wave to the medium. In most biological systems, attenuation is dominated by absorption, and the contribution to the radiation force from other sources (e.g., scattering) is not considered [38, 39].

Acoustic radiation force imaging (ARFI) is a diagnostic imaging modality that images the viscoelastic response of tissue to an applied radiation force field [40]. The elastic modulus is a mechanical property of tissue subject to deformation via compression (Young's modulus) and shear (shear modulus). This is the source of image contrast in elasticity imaging methods like ARFI [41]. ARFI pulse sequences use a short, impulse-like pushing beam to produce transient deformations in tissue in the direction of wave propagation. A tracking beam encodes a spatial map of tissue displacement at a snapshot in time after excitation. This can be performed using a single commercial diagnostic ultrasound scanner at intensities that do not generate significant heating [42]. Tissue displacement is typically on the order of a few μm and is proportional to the temporal average intensity [43]. For a fixed force, displacement also increases with pulse duration and eventually reaches a steady state value [44]. While softer tissues produce larger displacements and take longer to reach steady state, it is not straightforward to relate displacement magnitude to a tissue-specific elastic modulus [45, 46]. ARFI thus provides a qualitative measure of tissue stiffness.

The radiation force also induces shear stresses in tissue which generate waves that propagate perpendicular (or transverse) to the direction of compression. The shear modulus G increases with the propagation speed c_T of these shear waves:

$$c_T = \sqrt{\frac{G}{\rho}}, \tag{2.12}$$

where ρ is the density of the medium. If ρ is known, the shear modulus can be computed by applying a radiation force field in tissue and monitoring the shear wave propagation front. Shear wave elasticity imaging is a quantitative method to image tissue stiffness [47].

2.3 Technological considerations for transcranial MRgFUS

2.3.1 Influence of skull bone

The human skull is made up of two dense cortical bones (inner and outer tables) surrounding a porous trabecular layer (diploe). Heterogeneity between these layers imparts a large range of skull acoustic properties. For example, the speed of sound in the skull ranges from 1500-3000 $\mathrm{m \cdot s^{-1}}$ (or twice that of brain tissue), and skull sound speed, density, and thickness vary both within and between individual subjects [48]. Ultrasound is also significantly attenuated by bone through various loss mechanisms, like absorption, mode conversion, reflection, and scattering [49]. These variations in skull acoustic properties cause acoustic pressure waves originating from different locations of the MRgFUS transducer to travel through the skull at variable speeds and with variable attenuations, so that they arrive at the acoustic focus out of phase and with different amplitudes. This results in focus aberration. Figure 2.1 illustrates how skull-induced aberrations of the acoustic pressure field can widen and distort the focus, which reduces spatial specificity. They also reduce treatment efficiency or the peak pressure generated at the focus per unit of input power [50, 51]. This can be overcome by supplying more power to the transducer, but this raises the risk of skull heating [52]. Transient changes in skull acoustic properties have even been observed with repeated sonications during treatment [53].

Other skull-related factors like the skull-density ratio (SDR) have been associated with treat-

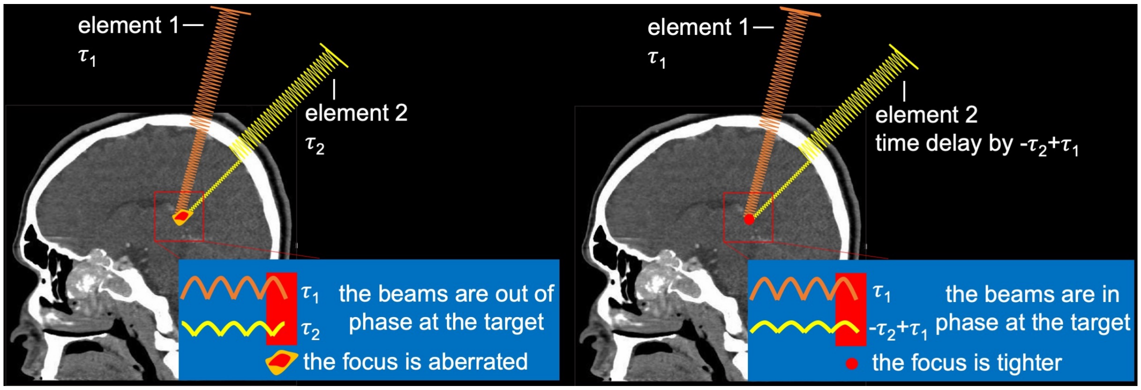

Figure 2.1: The human skull is a heterogeneous organ with a large range of acoustic properties. This causes acoustic pressure waves originating from different locations to travel through the skull in an incoherent fashion, which results in focus aberration. Correcting phases and amplitudes can be applied to maximize constructive wave interference at the target and overcome skull-induced aberrations. Image adapted with permission from [54].

ment outcomes [55]. The SDR is defined as the ratio in thickness between the trabecular and cortical layers of the skull. Generally, patients with low SDRs (i.e., larger cortical bones) are less favorable candidates for transcranial MRgFUS because of the higher power required to overcome attenuation [56, 57]. An SDR below 0.40 is an absolute contraindication to treatment for essential tremor via MRgFUS ablative thalamotomy [58]. Currently, this is the only medical contraindication to treatment (besides for patients who cannot undergo an MRI for other medical reasons and/or had a prior thalamotomy).

2.3.2 Frequency selection

Transcranial MRgFUS is typically performed at a frequency close to 1 MHz. Higher frequencies offer several advantages for transcranial applications [59]. Absorption increases with frequency (Eqn 2.7), which is ideal in clinical applications like ablation where heat deposition is the goal. In addition, the wavelength in tissue is smaller at higher frequencies (about 1.5 mm at 1 MHz), which maximizes spatial specificity. The cavitation threshold is also higher, since the pressure required to obtain a given MI decreases with frequency (Eqn 2.10). However, lower frequencies are desirable since they are less attenuated (Eqn 2.7) which enables greater tissue penetration. Also, the wavelength is negligible compared to the thickness of the human skull, which minimizes the impact of skull-induced aberrations [60, 61]. Low frequency FUS is thus less distorted when propagating through the skull, but at a cost of treatment efficiency, specificity, and safety.

2.3.3 Transducer geometry

The geometric focusing of a spherically curved transducer decreases with f-number:

$$f = \frac{F}{2a}, \tag{2.13}$$

where F is the focal length of the transducer (i.e., the radius of curvature), and a is the radius of the aperture. Transducers with a higher radius of curvature generate an acoustic focus deeper in tissue but with worse spatial specificity, since the lateral resolution of the beam decreases with f-number [62]. In transcranial applications, large apertures relative to the size of the human skull are used to distribute energy over the skull surface and minimize ultrasound-induced heating [63, 64]. A transparent membrane that circulates chilled water (15-20 °C) is placed between the transducer and the subject's scalp to further reduce skull heating. It also improves acoustic coupling [65].

Commercial transcranial MRgFUS systems use hemispherical phased array transducers with hundreds of elements to focus an acoustic pressure field [11, 12]. For example, the Insightec ExAblate Neuro is a 1024-element phased array transducer operated near 650 kHz (Fig 2.2). It has a focal length of 15.0 cm and a diameter of 30.0 cm ($f/0.5$), which enables targeting of deep brain regions in humans with high specificity and with concurrent MRI guidance [66]. Each element is electronically driven with its own voltage waveform, with the goal of keeping each complex-valued acoustic pressure wave matched in amplitude and phase at the targeted focus location. In this way, aberrations of the acoustic pressure field caused by the skull can be compensated. Specific aberration correction methods are discussed later in this chapter (Sec 2.4.2). Waves with suboptimal incidence angle transmission can also be shut off to improve treatment efficiency [67, 68].

A phased array transducer design enables flexible control of focusing and has fundamentally expanded the treatment envelope for transcranial applications of MRgFUS (the treatable volume within the cranial cavity) [16, 17]. For example, the acoustic focus can be steered away from the geometric focus location or multiple simultaneous foci can be generated in the acoustic pressure

Figure 2.2: The Insightec ExAblate 4000 ("Neuro") is a commercial transcranial MRgFUS system used in the US. It uses a 1024-element phased array ultrasound transducer operated near 650 kHz with a focal length of 15.0 cm and a diameter of 30.0 cm ($f/0.5$), which enables targeting of deep brain regions in humans with high spatial specificity and with concurrent MRI guidance. Currently, it is the only FDA-approved clinical device available for performing MRgFUS ablative thalamotomy in humans. Image courtesy of Insightec.

field using phase-only modulation algorithms [69]. This has demonstrated a reduction in treatment times during ablation [70]. Complex spatiotemporal distributions of intensity can be generated to pattern neuromodulation [71]. The beam can also be steered by mechanically translating and/or rotating the transducer bowl [72].

2.3.4 Image guidance with MRI

2.3.4.1 MR thermometry

The proton frequency frequency (PRF) or ω scales with the main magnetic field B_0, according to Eqn 2.1. The effective field at the nucleus is more precisely given by:

$$B_{\text{eff}} = B_0 + B_\sigma = (1+\sigma)\,B_0, \tag{2.14}$$

where B_σ is the field contribution due to a chemical shift of σ (in ppm). Chemical shift is a displacement of the PRF due to nuclear shielding, which is generated by the orbital motion of the surrounding electrons in response to B_0 [20]. σ is a shielding constant that is dependent on the chemical environment of the nucleus:

$$\sigma(\Delta\mathrm{T}) = \sigma_0 + \sigma_\mathrm{T}(\Delta\mathrm{T}), \tag{2.15}$$

where σ is a sum of temperature-independent contributions from σ_0 (e.g., B_0 inhomogeneities), and a temperature-dependent contribution from σ_T. For example, in water molecules, hydrogen nuclei are nominally shielded from B_0 by a chemical shift of σ_0. However, a hydrogen nucleus in a free water molecule is more effectively shielded than one that is hydrogen bonded to another water molecule. As temperature increases, hydrogen bonds weaken and break, which increases shielding via a reduction in σ_T. This reduces B_eff (Eqn 2.14), which in turn reduces the PRF. σ_T varies linearly with temperature ($\sigma_\mathrm{T}(\Delta\mathrm{T}) = \alpha\Delta\mathrm{T}$), with $\alpha = -0.01$ ppm/°C in pure water [73]. As a result, a change in the PRF leads to a phase accumulation ϕ that is proportional to temperature:

$$\Delta\mathrm{T} = \frac{\phi(t) - \phi(t_0)}{\gamma B_0 \alpha \mathrm{TE}}, \tag{2.16}$$

where TE is the echo time. PRF-based MR thermometry methods produce a relative temperature measurement by encoding phase images at a known temperature ($\phi(t_0)$) and during heating ($\phi(t)$) [74]. Notably, a number of other tissue parameters are also sensitive to temperature, like T1 and T2 relaxation times, diffusion, magnetization transfer, and proton density. However, most MR thermometry pulse sequences are based on the tissue PRF shift with temperature [13, 14]. With the exception of fat, extensive preclinical testing has shown that the PRF shift is tissue-type independent, even when tissue has been coagulated (between -0.009 and -0.01 ppm/°C, which is close to the pure water value). It is also linearly dependent on temperature over a clinically relevant range (-15 to 100 °C) [75].

The basic MR thermometry pulse sequence is a phase-sensitive T2-weighted gradient recalled echo (GRE) pulse sequence with TE $\approx$ T2* of the tissue. Ideally, MR thermometry provides high spatiotemporal resolution to monitor temperature in the targeted area. Specific image acquisition parameters depend on the application. For example, in low-temperature hyperthermia treatments (43-45 °C for minutes to hours), image update times of a minute can be adequate. However, update times of a few seconds are necessary in high-temperature ablation treatments (50-80 °C for a few seconds). The spatial resolution is chosen so that it is higher than the dimensions of the therapeutic focus (typically 1-3 mm in-plane), with volume coverage of both the ablation zone and a surrounding safety margin to monitor heating in the near- and far-fields of the transducer [13, 14]. Specific methods that can enable volumetric thermometry are discussed later in this chapter (Sec 2.4.1).

2.3.4.2 MR-acoustic radiation force imaging (MR-ARFI)

Magnetic field gradients are primarily used for spatial encoding in MRI (Sec 2.2.2), but they can also be used to sensitize MR images to incoherent (diffusion) or coherent (displacement, velocity, or acceleration) motion of spins. A change in the resonant frequency ω of precessing spins leads to a phase accumulation ϕ:

$$\phi(\mathbf{r}) = \int_0^{t_{\mathrm{end}}} \Delta\omega \, dt = \int_0^{t_{\mathrm{end}}} \gamma G(\mathbf{r},\tau)\,\mathbf{r}(\tau)\, d\tau, \tag{2.17}$$

where G is the spatially-varying and time-dependent magnetic field gradient applied at a spatial location $\mathbf{r}$ and time t. Motion-sensitizing gradients are typically bipolar in design and use two gradient lobes with equal area and opposite polarity. When spins are stationary and/or moving incoherently (e.g., random motion in molecular diffusion), no net phase accumulation occurs, since any phase accumulated during the first gradient lobe is unwound by the second lobe. This results in signal cancellation. Conversely, spins that move during the bipolar gradient accrue phase proportional to their net displacement Δx:

$$\phi(\mathbf{r}) = \gamma G_0 \delta \Delta x, \tag{2.18}$$

where $G_0 \delta$ is the area of one gradient lobe. In practice, two phase measurements with opposite gradient moments (i.e., inverted gradient polarities) are subtracted to minimize phase contributions from sources unrelated to motion (e.g., B_0 inhomogeneities) [22].

The radiation force generated by ultrasound produces transient tissue displacements in the direction of wave propagation, which is the source of image contrast in elasticity imaging methods like ARFI (Sec 2.2.2.2). Motion-sensitizing gradients synchronous with an ultrasound emission can be used to encode tissue displacements generated by the acoustic radiation force into the phase of an MR image. This technique is exploited by MR-acoustic radiation force imaging (MR-ARFI) [76]. MR-ARFI pulse sequences use the localized radiation force at the acoustic focus as a source for quasistatic displacement. It enables micron-scale sensitivity to tissue displacement on most MRI scanners (e.g., $\approx 4.6\ \mu$m per radian with 40 mT/m gradients that are 10 ms in duration). Thus, it is a promising approach for beam localization prior to transcranial MRgFUS procedures, especially for exposures that do not produce any measurable heating via MR thermometry (e.g., BBB opening, neuromodulation). Since radiation force-induced displacement is proportional to the temporal average intensity [43], MR-ARFI also provides a means to calibrate beam intensity for aberration correction in situ. This approach is discussed later in this chapter (Sec 2.4.2). MR-ARFI-derived displacement measurements have been validated against the canonical ultrasound imaging-based ARFI method ($R^2 = 0.67$ at 1.5 MHz), with no evidence of temperature elevation using relatively typical sonication parameters [77].

The basic MR-ARFI pulse sequence is a spin echo 2DFT pulse sequence with one set of bipolar motion-encoding gradients (MEGs). It only requires one sonication per TR, so the duty cycle is nominally low [76]. It has since been developed for rapid imaging of MRgFUS acoustic pressure fields, via EPI [78], keyhole [79], or spiral [80] k-space trajectories. In addition, repeated bipolar gradients [81, 82] and a variable trigger delay [83] have been proposed to minimize phase contributions from sources unrelated to ultrasound. The offset time between the start of the sonication and the MEGs ("trigger delay") can be optimized to best capture steady state displacement [84]. Higher phase sensitivity can be obtained via steady state free precession (SSFP) pulse sequences [85], though this method suffers from off-resonance distortions that worsen with field strength. Volumetric strategies for encoding 3D MR-ARFI displacement images have been proposed using 3D segmented EPI trajectories [86], with further efficiency gains using partial Fourier subsampling of k-space, parallel imaging, and beam steering to reduce the effective duty cycle at a given spatial location [87]. Simultaneous monitoring of temperature and displacement can be achieved by incorporating MEGs into GRE-based thermometry pulse sequences [88–90].

In vivo feasibility of transcranial MR-ARFI has been established in a few preclinical studies.

Two studies by one group showed evidence of transcranial displacement in living rat brains at 1.5 MHz. The location of the acoustic focus obtained with MR-ARFI was correlated with measurements obtained with a conventional MR thermometry pulse sequence during ablation treatment, and also with postmortem histological examination of the treated zones. These studies validated a workflow for beam localization via MR-ARFI prior to ablation treatment in small animals via high intensity transcranial MRgFUS therapy [91, 92]. Notably, studies in small animals generally benefit from higher gradient strength capabilities, which are not widely available in human MRI scanners (in those studies, 300 mT/m at 7 T main field strength). Another study in a larger living porcine model was performed using the 1024-element ExAblate 2000 through ex vivo human skull at 1.5 T (following craniectomy to replace existing skull). That study demonstrated sufficient sensitivity to MR-ARFI-derived displacement even at 220 kHz, where absorption is not relatively high for the radiation force to develop (Eqns 2.8 and 2.11) [93]. Two studies have demonstrated in vivo feasibility of transcranial MR-ARFI in non-human primates (NHPs) using single element MRgFUS transducers operated near 800 kHz. Ozenne et al [94] used acoustic simulations to predict transcranial ultrasound propagation prior to insonation of the NHP with MR-ARFI. Phipps & Jonathan [95] validated a method for preoperative stereotactic navigation via optical tracking to target the acoustic focus in specific cortical brain circuits [96]. Optical tracking is used to obtain the location of the MRgFUS transducer (freely movable) relative to the NHP brain (fixed) in MR image space coordinates, which is used to prescribe the MR-ARFI imaging slice and verify transcranial displacement. This method is the subject of Chapter 4. Both methods obtained displacement measurements of 1-1.5 μm, with no evidence of temperature elevation via MR thermometry.

2.4 Expansion of the treatment envelope

2.4.1 Volumetric temperature monitoring

MRI-derived temperature maps based on the proton resonance frequency (PRF) shift with temperature are predominantly used to guide transcranial MRgFUS treatment [13, 14]. Temperature maps are typically acquired using phase-sensitive 2D Fourier Transform (2DFT) gradient-recalled echo (GRE) pulse sequences with a long echo time (TE). To maintain adequate signal-to-noise ratio

(SNR) for temperature monitoring, most clinical MR thermometry implementations for transcranial MRgFUS image a single 2DFT slice. For example, MRgFUS ablative thalamotomy treatments for essential tremor use an in-plane spatial resolution of 1 mm × 1 mm, 3 mm thick slices, and a temporal resolution of 3.5 s [97]. While acoustic energy from MRgFUS is nominally focused to a single point in one slice, there is an ever-present risk that unintended heating may occur in the near- and far-fields of the transducer. Therefore, repeated sonications with different scanning planes are required to capture both the focal spot and the background with sufficient speed, precision, and volumetric coverage, leading to long treatment times and reduced patient safety.

State-of-the-art strategies for volumetric thermometry use pulse sequences that acquire k-space data more efficiently and/or temperature reconstruction methods that exploit undersampled k-space data, so that a full volume of data can be viewed at a high frame rate. Multi-slice echo-planar imaging (EPI) [98], segmented 3D EPI [99], and multi-slice excitation [100] sequences have been proposed for rapid temperature mapping. Multi-echo Cartesian [101, 102] and spiral [103–105] sequences have been shown to optimize SNR in the presence of off-resonance effects. Reduced field-of-view (FOV) sequences can mitigate aliasing artifacts that arise from the water bath inside the MRgFUS transducer, which improves scan efficiency [106]. Iterative temperature reconstruction approaches via temporal regularization [107–110] or fitting of constrained treatment models [111] have also enabled acceleration. Sparsity of the image domain data can be exploited for temperature reconstruction via compressed sensing [112]. Sparsity-promoting reconstruction methods have also been used in conjunction with multiband excitations for multislice thermometry sequencing with a single receive coil [113]. Generally, these approaches can be applied to any k-space trajectory. For example, Jonathan & Grissom [114] developed a method for volumetric thermometry using a 3D stack-of-stars pulse sequence, with temperature images reconstructed directly from undersampled k-space data using the k-space hybrid method. They obtained whole-brain volume coverage with image update times as low as 0.38 seconds. This method is the subject of Chapter 3. Radial methods have also been proposed for rapid encoding of multiecho acquisitions during T1-based thermometry [115, 116]. Notably, high acceleration parallel imaging-based techniques (which require multiple receive coils in close proximity to the body) are currently incompatible with transcranial MRgFUS since the coils must sit outside the transducer, far away from the head.

2.4.2 Skull-induced aberration correction

The influence of skull bone on ultrasound propagation was previously discussed in this chapter (Sec 2.4.1). Though ultrasound is strongly attenuated by the human skull, some energy is still able to propagate through it [48]. Early efforts to deliver transcranial FUS were successfully performed through intact skull, but not without damage to the overlying scalp, skull, and meninges [9]. Producing a lesion deep in the brain without damaging intervening nervous tissue required invasive craniotomy [117]. Ultrasound propagation benefitted from lower frequencies, but at a cost of spatial specificity [60]. The inability to focus ultrasound through intact skull limited the widespread dissemination of this technology until a hemispherical phased array transducer was developed for transcranial applications [11]. A large aperture is used to distribute energy over the skull surface and target focal regions deep in the brain. However, skull-induced aberrations of the acoustic pressure field remain a major technical barrier, especially at higher frequencies.

Phased array transducers generate an acoustic pressure field using hundreds of elements. Each element is electronically driven with its own voltage waveform so that each complex-valued acoustic pressure wave is matched in amplitude and phase at the targeted focus location. In this way, skull-induced aberrations that cause a mismatch between propagating waves can be compensated. State-of-the-art aberration correction methods for transcranial MRgFUS are described in the next section. These methods produce a set of amplitude and phase corrections that maximizes constructive wave interference at the target.

2.4.2.1 Time reversal mirrors

Historically, time reversal mirrors (TRMs) in the acoustic pressure field were the method of choice for correcting skull-induced aberrations. This method exploits the time invariance of the wave propagation equation. Briefly, if $p(\mathbf{r},t)$ is a pressure field solution to wave propagation, then so is $p(\mathbf{r},-t)$. TRMs use a monoelement transducer (e.g., a hydrophone) implanted near the targeted focus location so that the distorted wavefront can be sampled, time-reversed, and emitted by the phased array as it propagates through the skull. Waves that arrive first are transmitted last, and vice versa [118].

Studies in ex vivo human skulls have shown that TRMs can regain spatial specificity past the skull at high frequencies [119, 120]. Feasibility has been also been established in living rabbits with ex vivo human skull grafts [12, 121] and sheep with hydrophone insertion via lateral burr hole craniotomy [122]. These studies provided the formative evidence that focal lesioning with transcranial MRgFUS is possible using TRMs to correct skull-induced aberrations, sparing damage to intervening tissue. However, they are no longer of clinical interest because they require invasive craniotomy and/or a catheter-based approach to surgically implant a hydrophone near the target.

2.4.2.2 Ray-tracing

The use of preoperative computed tomography (CT) scans to estimate skull acoustic properties is the standard aberration correction method. The ray-tracing method computes element-wise phase corrections (ϕ) from the CT image:

$$\phi(i) = 2\pi f D(i)\left(\frac{1}{c_{\text{water}}} - \frac{1}{c_{\text{skull}}}\right), \tag{2.19}$$

where f is the frequency, D is the voxel-wise skull thickness in the path of transducer element i, and c is the effective sound speed (c_{water} = 1490 and c_{skull} = 2650 m/s). Ray-tracing is an analytical approach that computes phase corrections based on the approximate amount of time that each acoustic pressure wave takes to travel from the transducer to the targeted focus location, with knowledge of the skull thickness along a virtual ray cast between the center of each element and the target. Equation 2.19 is derived from a "single-layer" skull model that assumes a single sound speed over the thickness of skull traversed. For better performance, phase corrections that account for within-subject density variations can be computed using an empirical relationship between CT-derived Hounsfield units (proportional to density) and sound speed [123]. The ray-tracing method is currently used by commercial transcranial MRgFUS systems for aberration correction [124].

2.4.2.3 Virtual time reversal

Full-wave acoustic solvers can be used to simulate transcranial ultrasound propagation for aberration correction. These methods use a software implementation of the wave propagation equation, with the preoperative CT scan of the patient's skull registered to a model of the transducer in a computer simulation [125]. One method derives spatial maps of skull acoustic properties from tissue porosity (Φ), which decreases with Hounsfield units (HU):

$$\begin{aligned}
\Phi(\mathrm{HU}) &= 1 - \frac{\mathrm{HU}}{1000} \\
\rho(\Phi) &= \rho_{\mathrm{skull}} - (\rho_{\mathrm{skull}} - \rho_{\mathrm{water}}) \times \Phi \\
c(\Phi) &= c_{\mathrm{skull}} - (c_{\mathrm{skull}} - c_{\mathrm{water}}) \times \Phi \\
\alpha_{\mathrm{skull}}(\Phi) &= \alpha_{\mathrm{skull\,min}} + (\alpha_{\mathrm{skull\,max}} - \alpha_{\mathrm{skull\,min}}) \times \Phi^{\beta},
\end{aligned} \tag{2.20}$$

where ρ is the voxel-wise density (ρ_{water} = 1000 and ρ_{skull} = 2100 kg/m^3), c is the sound speed (c_{water} = 1500 and c_{skull} = 2900 m/s), α_{skull} is the absorption in the skull ($\alpha_{\mathrm{skull\,min}}$ = 1.33 and $\alpha_{\mathrm{skull\,max}}$ = 53.33 dB/cm/MHz), and β is a constant equal to 0.5 [126]. These equations assume a linear relationship between porosity (filled with water) and Hounsfield units, so Φ is close to 0 in most soft tissues and 1 in bone. Maximum values for ρ_{skull}, c_{skull}, and α_{skull} were originally derived by Fry and Barger in 1978 [48].

CT-based aberration correction via acoustic simulation is modeled after time reversal ("virtual time reversal"). In a simulation, a hydrophone is virtually embedded at the targeted focus location, and the distorted wave front is numerically sampled by the phased array as it propagates through the CT-derived simulation medium. The computed signals are time-reversed and emitted by the phased array in situ, with the patient's head positioned in the same configuration as in the simulation. The method in [126] was validated in a separate study, where peak pressure amplitudes reached 90% of what was obtained after optimal refocusing with an implanted hydrophone through an ex vivo human skull. No difference in beam width was observed. One 3D simulation took 2 hours to compute using a finite-difference time-domain (FDTD)-based acoustic solver [127].

Similar results have been reported with other software implementations of virtual time reversal for transcranial MRgFUS. Two studies independently showed that FDTD-based acoustic solvers provide superior refocusing compared to the canonical ray-tracing approach, but at a cost of computational complexity [124, 128]. Pseudo-spectral time domain (PSTD)-based simulation methods like the k-Wave Toolbox (http://www.k-wave.org) are widely used to simulate ultrasound propagation, with more efficient computation of acoustic spatial derivatives via FFTs for transcranial applications [129, 130]. The hybrid angular spectrum (HAS) method provides the shortest computation times for full-wave acoustic simulation [131]. In one study, HAS took 15 minutes to compute one 3D acoustic simulation for virtual time reversal, which represents an eight-fold speed improvement compared to FDTD [132]. A robust simulation framework has been developed using a HAS-based acoustic solver to prospectively determine patient-specific treatment efficiencies prior to transcranial MRgFUS [51, 133]. Element-wise simulation approaches may provide the most efficient strategy for acoustic modeling (2.5 s per element) [134].

The use of structural MRI scans for aberration correction actually predates the use of CT [135], but CT scans provide superior spatial resolution and contrast in bone and thus became the standard imaging method for estimating skull acoustic properties. Notably, ultrashort echo time (UTE) MRI pulse sequences are being developed as a potential substitute for CT scans in CT-based aberration correction algorithms for transcranial MRgFUS. UTE scans use ultrafast imaging strategies ($\approx$ μs after excitation) to encode the rapidly decaying MR signal in cortical bone. Studies in ex vivo human skulls have shown that UTE scans can be used to image skull bone and compute aberration corrections from UTE-derived bone masks. No significant differences were observed in beam size or location between UTE- and CT-based refocusing methods [136]. Segmentation of bone using UTE images to derive preoperative SDR values in patients accurately replicated CT-based segmentation methods in two separate studies [137, 138]. Thus, UTE images represent a feasible alternative to preoperative CT scans in transcranial MRgFUS clinical workflows. This and other MR-based methods offer several advantages for aberration correction over CT-based methods, which are discussed in the next section (Sec 2.4.2.4).

2.4.2.4 Energy-based adaptive focusing

For a phased array transducer of N elements, the complex-valued pressure contribution from an individual element n with an incident pressure P_n at the acoustic focus is:

$$P_n(t) = A_n e^{j2\pi f(t+\phi_n)}, \tag{2.21}$$

where f is the frequency, t is time, and A_n and ϕ_n are the amplitude and phase contributed from element n to the targeted focus location. In most MRgFUS applications, acoustic pressure waves interact with tissue via biophysical processes like heating and the radiation force, which are linked to the temporal average intensity (Sec 2.3). Unfortunately, relative phase differences between elements cannot be determined from a single time-averaged intensity measurement. Energy-based methods like iterative optimization [43] ($\approx 20N$ emissions) or adaptive focusing [139] ($4N$ emissions) can be implemented to estimate amplitude and phase shifts between elements from a set of intensity measurements performed in situ. The iterative method sweeps through a set of $[-\pi, +\pi]$ candidate phase shifts between a reference element and every other element in the array to identify a phase correction that maximizes wave intensity at the acoustic focus. Focal optimization is performed using radiation force-derived intensity measurements, which have been validated with MR-ARFI pulse sequences (Sec 2.3.4.2) for MR-based aberration correction [93].

Energy-based adaptive focusing is a more efficient aberration correction method that is based on the maximization of wave intensity for different spatially coded emissions. Four combinations of ultrasonic emissions are proposed per element: $\frac{1}{2}(V_0 + V_m)$, $\frac{1}{2}(V_0 - V_m)$, $\frac{\sqrt{2}}{2}(V_0 + jV_m)$, and $\frac{\sqrt{2}}{2}(V_0 - jV_m)$, where V_0 is one element chosen as a reference, and V_m is the mth element in the phased array. The intensity at the focus for the first element combination ($\frac{1}{2}(V_0 + V_m)$) is:

$$I_{1m} = \frac{\left|\frac{1}{2}[A_0 e^{j2\pi f(t+\phi_0)} + A_m e^{j2\pi f(t+\phi_m)}]\right|^2}{2\rho c}, \tag{2.22}$$

where ρ is the density, and c is the sound speed in the supporting medium. This gives:

$$\begin{aligned} I_{1m} &= \frac{1}{2\rho c}\left|\frac{1}{2}e^{j2\pi ft}(A_0 e^{\phi_0} + A_m e^{\phi_m})\right|^2 \\ &= \frac{1}{8\rho c}\left|A_0 e^{\phi_0} + A_m e^{\phi_m}\right|^2 \\ &= \frac{1}{8\rho c}\left|(A_0\cos(\phi_0) + j\sin(\phi_0)) + (A_m\cos(\phi_m) + j\sin(\phi_m))\right|^2 \\ &= \frac{1}{8\rho c}\left|(A_0\cos(\phi_0) + A_m\cos(\phi_m)) + j(A_0\sin(\phi_0) + A_m\sin(\phi_m))\right|^2 \\ &= \frac{1}{8\rho c}\left[A_0^2 + A_m^2 + 2A_0A_m\cos(\phi_m - \phi_0)\right]. \end{aligned} \tag{2.23}$$

Computing the focal intensity I_{2m} for the second element combination ($\frac{1}{2}(V_0 - V_m)$), it can be seen that:

$$I_{1m} - I_{2m} = \frac{1}{8\rho c}\left[4A_0A_m\cos(\phi_m - \phi_0)\right]. \tag{2.24}$$

For convenience, P_0 is assigned a relative amplitude $A_0 = \sqrt{2\rho c I_{11}}$ and phase $\phi_0 = 0$. Thus:

$$I_{1m} - I_{2m} = \mathrm{Re}\{P_m\}. \tag{2.25}$$

A similar expression can be derived for $\mathrm{Im}\{P_m\}$, from the third ($\frac{\sqrt{2}}{2}(V_0 + jV_m)$) and fourth ($\frac{\sqrt{2}}{2}(V_0 - jV_m)$) element combinations:

$$I_{4m} - I_{3m} = 2\,\mathrm{Im}\{P_m\}, \tag{2.26}$$

where I_{3m} and I_{4m} are the focal intensities for the third and fourth element combinations, respectively. In summary:

$$\begin{aligned} \mathrm{Re}\{P_m\} &= I_{1m} - I_{2m} \\ \mathrm{Im}\{P_m\} &= \frac{I_{4m} - I_{3m}}{2}. \end{aligned} \tag{2.27}$$

The relative amplitude and phase contributions from each element in the phased array can be estimated from the intensity of four spatially coded emissions per element with adaptive focusing. The amplitude and phase aberrations of the waves through an aberrator can be retrieved using this method. Applying a correcting phase of $\angle(A_0 A_m^*)$ to each element m in the phased array (e.g., producing the time-reversed wave) will nominally maximize constructive wave interference at the targeted focus location. Inverse amplitude corrections provide the best performance for refocusing (proportionally increasing the output of the array elements that yield better transmission through the skull) [140]. In total, $4N$ emissions are required to refocus the acoustic pressure field [139].

The radiation force generated in tissue produces transient displacements in the direction of wave propagation, which was previously discussed in this chapter (Sec 2.2.2.2). It is well accepted that radiation force-induced displacement is proportional to the temporal average intensity [43]. The use of MR imaging to guide adaptive focusing was achieved in [141] via MR-ARFI pulse sequences. A set of $4N$ spatially coded emissions are transmitted by the phased array, and the resultant displacement MR images (proportional to intensity) are used to estimate a set of amplitude and phase corrections using Equation 2.27. This method benefits from a Hadamard basis transformation to improve SNR at the acoustic focus, which is done by defining linear combinations of the array elements according to the Hadamard matrix [139].

The beam resulting from MR-guided adaptive focusing achieved near optimal refocusing in one study with an intact human cadaver head. The method required 1536 Hadamard-coded emissions (384 elements × 4) and took 2 hours of acquisition time to refocus the acoustic pressure field. This was the first demonstration of MR-ARFI-based refocusing in a clinical MRgFUS environment [142]. Ongoing work in this field is aimed at improving the efficiency of adaptive focusing, either by reducing acquisition times and/or the number of required intensity measurements to compute the complex-valued aberration corrections. Zernike polynomials have been proposed to replace the canonical Hadamard basis transformation. One study showed that the number of Zernike-derived emissions required to approximate a set of skull-induced aberrations represented a small fraction of the number of elements ($\approx 0.8N$). Unfortunately, the aberration corrections in that study were largely derived from simulations, so its performance in situ is unknown [143]. Another study showed that random calibration measurements could be fit in a least-squares sense to the complex-valued free-field pressure transmission matrix to further improve refocusing efficiency. Again, this study derived aberration corrections from simulated acquisitions of MR-ARFI, so its true benefit is unknown. Also, it did not recognize that displacement is proportional to temporal average intensity, which is a quantity that does not contain phase information [144]. Efficient adaptive focusing with MR-ARFI has been achieved with a rapid EPI pulse sequence acquisition. One study estimated aberration corrections from 64 groups of 4 elements (256 physical elements) in less than 10 minutes using an EPI pulse sequence optimized for MR-ARFI. However, it used a short TR of 44 ms to obtain a short acquisition time, which resulted in a high duty cycle (2.3%) and unacceptable heat deposition at the focus (4.86 °C) [145]. A hybrid MR-ARFI/simulation approach has also been proposed, but it requires a separate simulation step, and its benefit was minimal in the setting of skull-induced aberrations (< 0.1 rad improvement in phase) [146]. Ongoing work by Jonathan et al. has shown that aberration corrections may be estimated from many fewer pressure field measurements in situ after fitting to pre-acquired complex-valued pressure fields via magnitude least squares optimization. This method benefits from beam illuminations across the entire pressure field since aberrations are estimated from pressure measurements in multiple voxels jointly (the "multi-voxel" method). This method is the subject of Chapter 5.

Adaptive focusing with MR-ARFI offers several advantages for transcranial MRgFUS aberration correction. The standard aberration correction method uses a preoperative CT scan of the patient's skull to derive element-wise amplitude and phase corrections that refocus the acoustic pressure field through the skull. Eliminating the need for CT-based aberration correction would benefit treatment planning for several reasons. Both CT-based refocusing methods (ray-tracing, virtual time reversal) are parametric and require a priori knowledge of skull acoustic properties. Established methods use empirical assumptions of wave propagation that were largely derived from ex vivo human skull fragments [48, 123]. Studies have shown that the relationship between skull acoustic properties and CT-derived Hounsfield units is not straightforward, since it varies with photon energy and reconstruction method [147]. Comparisons between simulated and experimental treatment efficiencies have revealed the need for skull-specific acoustic models, which is limited by the availability of patient data to validate such models [50, 51, 53]. Depending on the acoustic solver that is used, CT-based refocusing can take hours to produce one set of amplitude and phase corrections per targeted focus location [126]. In addition, a registration step is required to align the CT referential frame to MR, which could introduce simulation errors if the transducer model is not properly aligned to the patient's skull in situ. Systematic variations in assigned medium properties result in significant changes in the simulated results [148, 149]. CT scans also contain ionizing radiation, which is undesirable in transcranial MRgFUS studies with healthy controls. Conversely, MR-guided adaptive focusing enables immediate feedback of focusing quality. It makes no assumptions of acoustic properties in the supporting medium, and thus can produce a set of amplitude and phase corrections for any aberrator configuration to refocus the acoustic pressure field in situ.

Chapter 3

Volumetric MRI thermometry using a three-dimensional stack-of-stars echo-planar imaging pulse sequence

3.1 Abstract

Purpose:

To measure temperature over a large brain volume with fine spatiotemporal resolution.

Methods:

A 3D stack-of-stars echo-planar imaging (3D SoS EPI) sequence combining EPI and radial sampling with golden angle spacing was implemented at 3 Tesla for proton resonance frequency-shift temperature imaging. The sequence acquires a 188x188x43 image matrix with 1.5x1.5x2.75 mm^3 spatial resolution. Temperature maps were reconstructed using SENSE image reconstruction followed by the image domain hybrid method, and using the k-space hybrid method. In vivo temperature maps were acquired without heating to measure temperature precision in the brain, and in a phantom during high-intensity focused ultrasound sonication.

Results:

In vivo temperature standard deviation was less than 1°C at dynamic scan times down to 0.75 seconds. For a given frame rate, scanning at a minimum TR with minimum acceleration yielded the lowest standard deviation. With a 3.0 second frame rate, the scan was tolerant to a small number of receive coils, and temperature standard deviation was 41% higher than a standard 2DFT temperature mapping scan, but provided whole-brain coverage. Phantom temperature maps with no visible aliasing were produced for dynamic scan times as short as 0.38 seconds. k-Space hybrid reconstructions were more tolerant to acceleration.

Conclusion:

3D SoS EPI temperature mapping provides volumetric brain coverage and fine spatiotemporal res-

olution.

3.2 Introduction

Temperature monitoring with magnetic resonance imaging (MRI) has enabled many emerging minimally invasive thermal therapies, including MR-guided focused ultrasound (MRgFUS) and radiofrequency, microwave, and laser interstitial thermal therapies. Of these, MRgFUS is a completely noninvasive method that uses an external transducer to focus high-power ultrasound into tissue for ablation [150]. MRgFUS has been used successfully in humans to treat uterine fibroids [151], bone metastasis-related pain [152], cancer [153–155], and deep brain tissue [2, 156–159]. Additionally, transcranial MRgFUS [160] has been used without ablation to disrupt the blood-brain barrier for improved drug delivery [161] and induce neuromodulation [6].

MRI-derived temperature maps based on the proton resonance frequency (PRF) shift with temperature are predominantly used to guide MRgFUS treatment [13]. Temperature maps are typically acquired using phase-sensitive 2D Fourier transform (2DFT) gradient-recalled echo (GRE) pulse sequences with a long echo time (TE). To maintain adequate signal-to-noise ratio (SNR) for temperature monitoring, most clinical MR thermometry implementations for transcranial MRgFUS image a single 2DFT slice [97]. While acoustic energy from MRgFUS is nominally focused to a single point in one slice, there is an ever-present risk that unintended heating may occur in the near- and far-fields of the transducer. Therefore, repeated sonications with different scanning planes are required to capture both the focal spot and the background with sufficient speed, precision, and volumetric coverage, leading to long treatment times and reduced patient safety.

Previous efforts in volumetric thermometry have used pulse sequences that acquire k-space data more efficiently and/or temperature reconstruction methods that exploit undersampled k-space data, so that a full volume of data can be viewed at a high frame rate. Multi-slice echo-planar imaging (EPI) [98], segmented 3D EPI [99], and multi-slice excitation [100] sequences have been proposed. Multi-echo Cartesian [101, 102] and spiral [103, 104] sequences have been shown to optimize SNR in the presence of off-resonance effects. Iterative temperature reconstruction approaches have also enabled acceleration via temporal regularization [107–110] or fitting constrained treatment models [111]; generally, these approaches can be applied to any k-space trajectory. Of note, high acceleration parallel imaging-based techniques (which require multiple receive coils in close proximity to the body) are currently incompatible with transcranial MRgFUS since the coils must sit outside the transducer, far away from the head.

In this work, we describe and validate a hybrid radial-Cartesian pulse sequence that acquires a 3D stack-of-stars k-space trajectory with EPI planes (3D SoS EPI) for volumetric thermometry. EPI is performed in the slice dimension to provide rapid slice sampling of a volume k-space. Successive EPI planes are spaced by the golden angle [162], so that radial spokes are approximately evenly distributed regardless of the width of the reconstruction window. This enables the length and positions of reconstruction windows to be set retrospectively. The center of k-space (which contains most of the dynamic image contrast) is acquired each TR, ensuring that peak heat will not be missed. Also, unlike other non-Cartesian trajectories, off-resonance phase is mostly accrued in the EPI phase-encode dimension where it is straightforward to correct [163]. This sequence has been demonstrated in neuroimaging applications other than thermometry [164–168].

Here, we reconstruct volumetric temperature maps from 3D SoS EPI using both non-Cartesian SENSE image reconstruction [169] followed by hybrid multibaseline subtraction and referenceless temperature map estimation [170], and the k-space hybrid method [111]. Each slice is reconstructed in parallel. In vivo experiments without heating and phantom experiments with heating were performed at 3 Tesla to characterize temperature precision across acceleration factors, repetition times and number of receive coils, and to compare the sequence with a 2DFT temperature mapping sequence [171]. We further show that heating-induced chemical shift (CS) pixel shifts that arise in the hot spot can be corrected retrospectively [163]. Aspects of this work have been presented previously in Ref. [172]

3.3 Methods

3.3.1 Pulse sequence

Figures 3.1 and 3.2 show the k-space sampling pattern of the 3D SoS EPI pulse sequence, which was implemented on a 3 T scanner (Philips Achieva, Philips Healthcare, Best, The Netherlands). Following slab excitation along the phase-encode axis, each TR acquires a 2D GRE-EPI plane using in-plane frequency-encoding (k_x-k_y) along a radial line and through-plane Cartesian phase-encoding (k_z). The plane is rotated between consecutive TRs by 111.25° about the phase-encoded (k_z) axis to acquire a 3D stack-of-stars k-space trajectory with golden angle spacing [162]. Gradient spoiling is applied at the end of each TR [173]. The sequence was implemented with parameters: 28.0×28.0 cm^2 in-plane (axial) FOV; 188×188 in-plane matrix size; 1.50×1.50 mm^2 in-plane voxel size; 43 slices; slice thickness 2.75 mm; TE 17 ms; phase-encode direction F/H; phase-encoding pixel bandwidth 31.9 Hz/px; frequency-encoding bandwidth 1904.9 Hz/px; spectrally-selective fat suppression. The encoded 43 slice imaging volume in the slab direction was 9 mm wider than the excited slab to prevent wrap-around artifacts. The minimum TR for the sequence was 47 ms. Second-order shimming was performed prior to acquisition. Prior to dynamic scanning, non-phase-encoded echoes are acquired for each rotated EPI plane to estimate line-to-line delays and phase shifts for ghost correction.

3.3.2 Temperature reconstruction

Temperature maps were reconstructed offline in MATLAB R2015a (MathWorks, Natick, MA, USA) using Vanderbilt University's parallel computing cluster (Advanced Computing Center for Research and Education, Vanderbilt University, Nashville, TN, USA). Figure **??**b shows the 3D SoS EPI temperature reconstruction pipeline. First, EPI ghost correction was performed on each EPI plane in the dynamic acquisition [174]. Next, each volume k-space was inverse Fourier transformed along the slice (z) dimension, creating a hybrid k-space/image domain (k_x-k_y-z) volume. One volume k-space in the reconstruction (i.e., one dynamic) spanned a contiguous set of radial lines; the acceleration factor/dynamic scan time was adjusted post-acquisition (e.g., fewer contiguous radial lines per dynamic for more acceleration/shorter dynamic scan time). Each slice's k-space data in the hybrid volume was then reconstructed in parallel using one Intel Xeon Westmere processing core (Intel Corporation, Santa Clara, CA) and 1 GB of RAM per slice.

Temperature maps were reconstructed using the hybrid multibaseline and referenceless method [170] after image reconstruction using conjugate gradient (CG)-SENSE [169], or were reconstructed directly from undersampled k-space data using the k-space hybrid method [111]. CG-SENSE image reconstructions used 30 iterations and nonuniform fast Fourier transforms [175]. Both temperature reconstruction approaches fit the same image domain hybrid multibaseline and

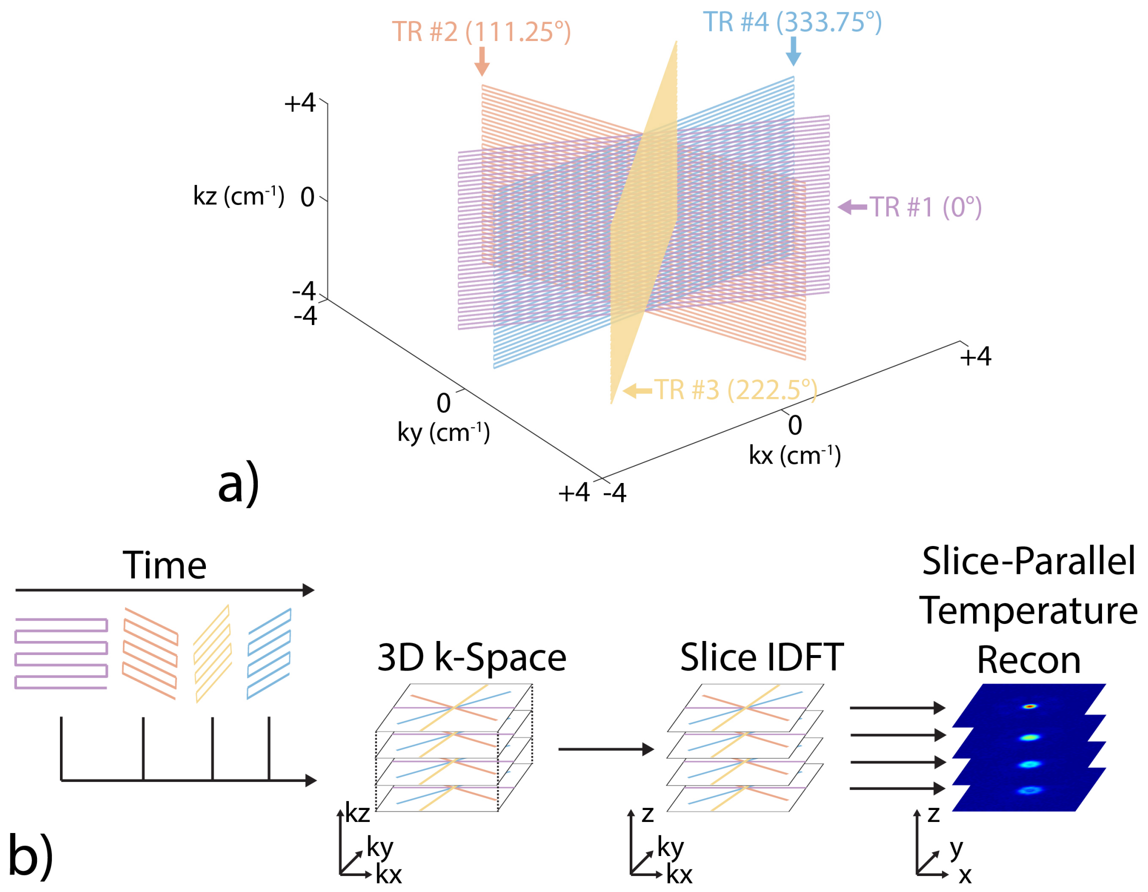

Figure 3.1: 3D SoS EPI k-space sampling pattern and temperature reconstruction pipeline. (a) 3D SoS EPI combines in-plane radial sampling and through-plane Cartesian EPI sampling. Each TR acquires one 2D GRE-EPI plane. Successive EPI planes are spaced by the golden angle (111.25°), producing radial spokes in a 3D stack-of-stars k-space trajectory. (b) One volume k-space or one dynamic in the reconstruction spans any contiguous set of radial lines in the acquisition. The length and position of the reconstruction window can be set retrospectively. In this illustration, data from four consecutive TRs forms a k-space volume, which is inverse Fourier transformed in the slice dimension (z) to produce a hybrid k-space/image domain volume (k_x-k_y-z). Slices are then processed in parallel to reconstruct temperature maps using CG-SENSE with hybrid multibaseline subtraction and referenceless thermometry, or with k-space hybrid thermometry.

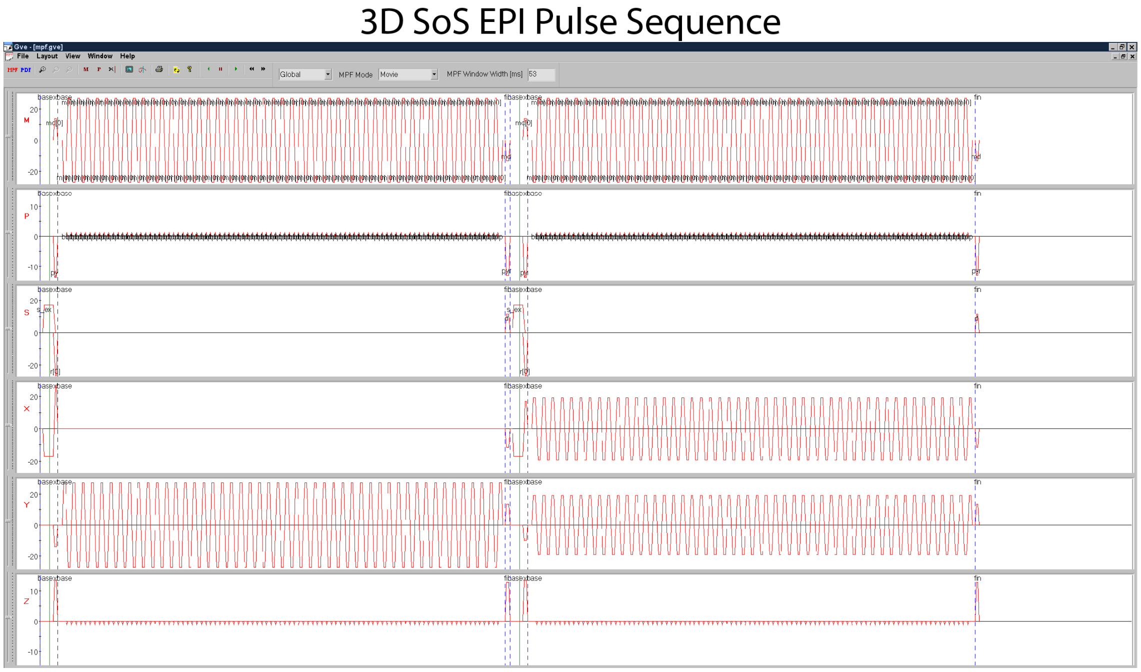

Figure 3.2: 3D SoS EPI pulse sequence (Philips PPE Output). 3D SoS EPI is a hybrid radial/Cartesian EPI pulse sequence. The first two dynamics of the pulse sequence are shown. Each dynamic acquires a 2D GRE-EPI plane, with successive EPI planes spaced by the golden angle (111.25°) to produce a 3D stack-of-stars k-space trajectory.

referenceless image model, but in k-space hybrid, the Fourier transform of the model is directly fit to the k-space data, skipping the image reconstruction step. Temperature maps were reconstructed using one of two temperature reconstruction methods:

1. The hybrid multibaseline subtraction and referenceless method [170] after image reconstruction using conjugate gradient (CG)-SENSE [169], or
2. The k-space hybrid method [111].

CG-SENSE image reconstructions used 30 iterations and nonuniform fast Fourier transforms [175]. Both temperature reconstruction approaches fit the same hybrid multibaseline and referenceless image model, but in k-space hybrid, the Fourier transform of the model is directly fit to the k-space data, skipping the image reconstruction step. The hybrid multibaseline and referenceless image model is given by:

$$y_j(\boldsymbol{w},\boldsymbol{c},\boldsymbol{\theta}) = \left(\sum_{l=1}^{N_b} b_{l,j} w_l\right) e^{\imath(\{\boldsymbol{A}\boldsymbol{c}\}_j+\theta_j)}, \tag{3.1}$$

where y_j is the complex-valued MR signal at voxel j, $\{\boldsymbol{b}_l\}_{l=1}^{N_b}$ are complex baseline library images reconstructed from fully-sampled k-space data acquired prior to treatment, w_l are baseline image weights, $\boldsymbol{A}$ is a matrix of smooth (e.g., low-order polynomial) basis functions, $\boldsymbol{c}$ is a polynomial coefficient vector, and $\boldsymbol{\theta}$ is a heating-induced phase shift, which is negative for a temperature increase [13]. The role of the baseline library images $\{\boldsymbol{b}_l\}_{l=1}^{N_b}$ is to capture physiological and anatomical amplitude and phase variations across respiratory and cardiac cycles. The polynomial phase shift $\boldsymbol{Ac}$ models phase changes induced by smooth magnetic field shifts, such as center frequency drift and those caused by respiration. The phase shift $\boldsymbol{\theta}$ that results from targeted heating is modeled as a focal shift separate from these other phase components. In both the CG-SENSE plus image domain hybrid and k-space hybrid algorithms, the model in Eq. 3.1 is fit to the acquired data in a least-squares sense using an alternating minimization algorithm, in which the variables $\boldsymbol{w}$, $\boldsymbol{c}$, and $\boldsymbol{\theta}$ are alternately updated while holding the others fixed. Sparsity of $\boldsymbol{\theta}$ is exploited by the algorithms to separate it from the non-sparse polynomial phase shift, and reflects the fact that in a targeted thermal therapy like MRgFUS, temperature rises will occur in a minority of image voxels. Once fit, the phase shifts in $\boldsymbol{\theta}$ are converted to temperature changes in degrees Celsius according to:

$$\Delta T = -\frac{\theta}{\gamma \alpha B_0 TE}, \tag{3.2}$$

where γ is the gyromagnetic ratio in radians per second per Tesla, $\alpha = -0.01$ ppm/°C is the PRF change coefficient, B_0 is the main field strength in Tesla, and TE is the echo time in seconds [13]. Further details are provided in Refs. [170] and [111]. Experimental data sets described below and MATLAB code to process data sets can be downloaded from https://bitbucket.org/wgrissom/epi_stackofstars_thermometry.

3.3.3 In vivo experiments

To evaluate temperature precision in vivo, 5 healthy volunteers (3F/2M) were scanned without heating with the approval of the Institutional Review Board at Vanderbilt University. An 8-channel head coil array was used for reception.

First, a 3D SoS EPI scan was collected in each subject to measure temperature standard deviation (using the approach described below) across acceleration factors/dynamic scan times: no acceleration (300 radial lines; 14.1 s per dynamic), 2× (150 lines; 7.1 s), 4.7× (64 lines; 3.0 s), 9.4× (32 lines; 1.5 s), 18.8× (16 lines; 0.75 s), and 37.5× (8 lines; 0.38 s). These scans used the sequence's minimum TR of 47 ms and a 14° flip angle (the Ernst angle, assuming a brain T_1 of 1400 ms at 3.0 T). The scans lasted 2 minutes (2450 radial lines were acquired). For each acceleration factor, temperature maps were reconstructed from consecutive non-overlapping temporal windows. To investigate the tradeoff between TR and acceleration factor for a fixed dynamic scan time, 3D SoS EPI scans were then acquired at three TRs (47, 90, and 180 ms). Subjects were scanned at the Ernst angle (14° for TR = 47 ms, 20° for TR = 90 ms, and 28° for TR = 180 ms) and for 2 minutes per acquisition (2450 radial lines for TR = 47 ms, 1250 lines for TR = 90 ms, 650 lines for TR = 180 ms). From each data set, temperature maps were reconstructed from non-overlapping temporal windows with an acceleration factor set to achieve a dynamic scan time of 3 seconds (64 radial lines per dynamic for TR = 47 ms, 34 lines for TR = 90 ms, 17 lines for TR = 180 ms). 100 temperature maps spaced 1 second apart were reconstructed for each data set. Most current MRgFUS systems use the scanner's single-channel body coil for receive, and the number of number of receive coils that can be placed close to the head for high SNR and sensitivity encoding will likely remain limited in the near future. For this reason, we also investigated the dependence of temperature precision on the number of coils by compressing the multicoil data from 8 to 6, 4, 2, and 1 coil(s) by truncating the singular values of the data matrix before temperature reconstruction [176]. Coil-compressed images and temperature maps were reconstructed from the 47 ms TR data set with 4.7× acceleration/3.0 second dynamic scan time. We note that the SNR in these compressed reconstructions will still be higher than that of a body coil scan, so the results will primarily characterize how temperature precision depends on the spatial encoding provided by a multicoil array. Also note that in the one-coil case, the SENSE reconstruction becomes a single-coil iterative reconstruction, with no sensitivity encoding. In addition to the single-shot 3D SoS EPI scans above, images were acquired in one subject using two and three interleaved EPI shots to qualitatively evaluate reduction of off-resonance distortions with additional shots. This increased the phase-encoding pixel bandwidth from 31.9 Hz/px (single-shot) to 61.9 Hz/px (two shots) and 99.0 Hz/px (three shots). No other scan parameters were changed.

To compare the temperature precision of 3D SoS EPI against a standard 2DFT temperature mapping sequence and illustrate differences in volume coverage, 2DFT scans were also acquired in each subject with representative parameters [171]: 28.0×28.0 cm^2 FOV; 188×96 image matrix; 1.50×3.0 mm^2 voxel size; 1 slice; slice thickness 2.75 mm; TE/TR 12 ms/35 ms; flip angle 13°; phase-encode direction A/P; frequency-encoding pixel bandwidth 60 Hz/px; spectrally-selective fat suppression; dynamic scan time 3.3 s. The scans were repeated in three slice orientations (axial, sagittal, and coronal). Temperature standard deviation was calculated using the same hybrid multibaseline and referenceless processing applied to the CG-SENSE plus image domain hybrid 3D SoS EPI reconstructions. Subjects were scanned for 2 minutes/40 dynamics. The first 4 images were used in the 2DFT baseline library, so that approximately the same total time was spent on baseline acquisition for 2DFT and 3D SoS EPI. The resulting 2DFT maps were compared to those reconstructed from a TR = 47 ms 3D SoS EPI acquisition with 4.3× acceleration/69 lines per dynamic, so that the dynamic scans were matched (3.3 seconds per dynamic).

For the above experiments, in vivo temperature errors and subsequently temperature standard deviation were calculated using the hybrid model validation procedure described in [111]. Briefly, the hybrid image model in Equation 3.1 was twice fit to each frame of data. The first 300 radial lines of each 3D SoS EPI acquisition were used to reconstruct a baseline image for this model using CG-SENSE. All reconstructions used a single baseline, so $\boldsymbol{w}$ was fixed to 1, and a first-order polynomial basis (drift and two linear terms) [170]. In the first fit, only the polynomial coefficients $\boldsymbol{c}$ were updated, while the temperature phase shifts $\boldsymbol{\theta}$ were held fixed at zero. In the second fit, the estimate of $\boldsymbol{c}$ from the first fit was held fixed, and only $\boldsymbol{\theta}$ was updated, with no sparsity penalty or other regularization. Using this approach, all residual temperature errors after fitting the baseline and referenceless components of the model are captured in $\boldsymbol{\theta}$. The temperature error maps were then used to calculate through-time temperature standard deviation maps [104], and to calculate temperature standard deviation across all brain voxels, time points, and subjects. Temperature standard deviation was computed in brain tissue only as determined using an automatic segmentation algorithm [177]. The through-time standard deviation maps were upsampled onto a 1.50 mm^3 isotropic grid for display.

3.3.4 Phantom heating experiments

A cylindrical tissue-mimicking gel phantom was sonicated using a Philips Sonalleve MR-HIFU system (Philips Healthcare, Vantaa, Finland) operated at 1.1 MHz and 110 W for 30 s. A single point 14.0 cm from the transducer was targeted with A/P FUS beam propagation. A 3D SoS EPI scan was acquired during the sonication with a TR of 47 ms, no fat suppression and A/P phase-encoding, but otherwise the same parameters as the in vivo scans. A five-element HIFU abdominal coil array was used for reception. The phantom was allowed to cool for 10 minutes between consecutive sonications. Temperature maps were compared across acceleration factors. Temperature maps from 3D SoS EPI were further compared to 2DFT temperature maps. The same imaging parameters from the in vivo scan were used for 2DFT, except without fat suppression and with R/L phase-encoding. For all acceleration factors, temperature maps were reconstructed using a single baseline, 6 TR/282 ms window spacing, and a zeroth-order polynomial basis. ℓ_1 sparsity and roughness regularization parameters were tuned for these reconstructions to be $\lambda = 2\times10^{-5}$ and $\beta = 2^{-14}$, respectively [111]. The hybrid model parameters $\boldsymbol{w}$, $\boldsymbol{c}$, and $\boldsymbol{\theta}$ were all initialized to zeros in the first dynamic, and were thereafter initialized to the previous dynamic's values. At peak heat, CG-SENSE plus image domain hybrid 3D SoS EPI temperature maps were reconstructed with and without chemical shift compensation applied in the EPI phase encode dimension [163].

3.4 Results

3.4.1 In vivo experiments

Figure 3.3a shows 3D SoS EPI through-time temperature standard deviation maps versus acceleration factor in one subject. Temperature uncertainty increased with acceleration factor for both reconstruction methods, but increased more rapidly for CG-SENSE plus image domain hybrid. Figure 2b plots temperature standard deviation calculated over all brain voxels, time, and all 5 subjects. The k-space hybrid reconstructions achieved uncertainty less than 1°C up to an acceleration factor of 18.8×, corresponding to a dynamic scan time of 0.75 seconds. The CG-SENSE plus image domain hybrid reconstructions achieved uncertainty less than 1°C up to 2× acceleration, and 1.13°C uncertainty at 4.7×, corresponding to a dynamic scan time of 3.0 seconds. Figure 3.4a shows through-time temperature standard deviation maps versus TR in one subject, reconstructed with a fixed 3 second dynamic scan time. Figure 3.4b plots temperature standard deviation calculated over all brain voxels, time, and subjects. Temperature uncertainty increases with increasing TR for both CG-SENSE plus image domain hybrid and k-space hybrid reconstructions. These results indicate that it is better to acquire more data with a minimum TR than to use a longer TR to obtain higher signal amplitude in each readout. Again, k-space hybrid reconstructions have consistently lower uncertainty than CG-SENSE plus image domain hybrid. Figure 3.5a shows through-time standard deviation maps versus number of receive coils for one subject, and Figure 3.5b plots temperature standard deviation calculated over space, time and all 5 subjects. Figure 3.5b shows that the overall precision of both reconstructions degraded as the number of coils decreased, though due to significantly increased blurring in the CG-SENSE reconstructions for 2 coils and 1 coil (visible in the magnitude images of 3.5a), the through-time standard deviations of CG-SENSE plus image-domain hybrid improved in those cases. In all cases, k-space hybrid temperature precision was better than 1°C, and except for the one coil reconstruction, CG-SENSE plus image domain hybrid temperature precision was better than 1.25°C.

Figure 3.6a compares 3D SoS EPI and 2DFT temperature standard deviation. Temperature uncertainty at the edge of the brain was higher in 2DFT, due to its higher sensitivity to physiological noise (e.g., brain pulsation during the cardiac cycle, respiration, subject motion). These uncertainties are averaged down in 3D SoS EPI since the center of k-space is sampled every TR. Average temperature standard deviation was calculated in ROIs that excluded blood vessel artifacts, zipper-like artifacts across the frequency-encoded dimension that may be due to external interference, and uncertainties around the edge of the brain in the 2DFT maps. Excluding these artifacts, computed across 5 subjects and 3 slice orientations, 3D SoS EPI had approximately 48% higher temperature uncertainty than 2DFT (0.27°C for 2DFT vs. 0.40°C for 3D SoS EPI). However, this tradeoff in temperature precision enables full brain coverage with 3D SoS EPI, as illustrated in Figure 3.6b.

Figure 3.7 illustrates off-resonance distortions in 3D SoS EPI versus multishot factor. Geometric distortions (white arrows) are present in brain regions where field inhomogeneities are significant. Off-resonance causes signal to shift in the slice dimension. Distortions are reduced when multiple shots are used, which increases the pixel bandwidth from 31.9 Hz/px (single-shot) to 61.9 Hz/px (two shots) and 99.0 Hz/px (three shots). At 3.0 T, the PRF changes by 1.27 Hz

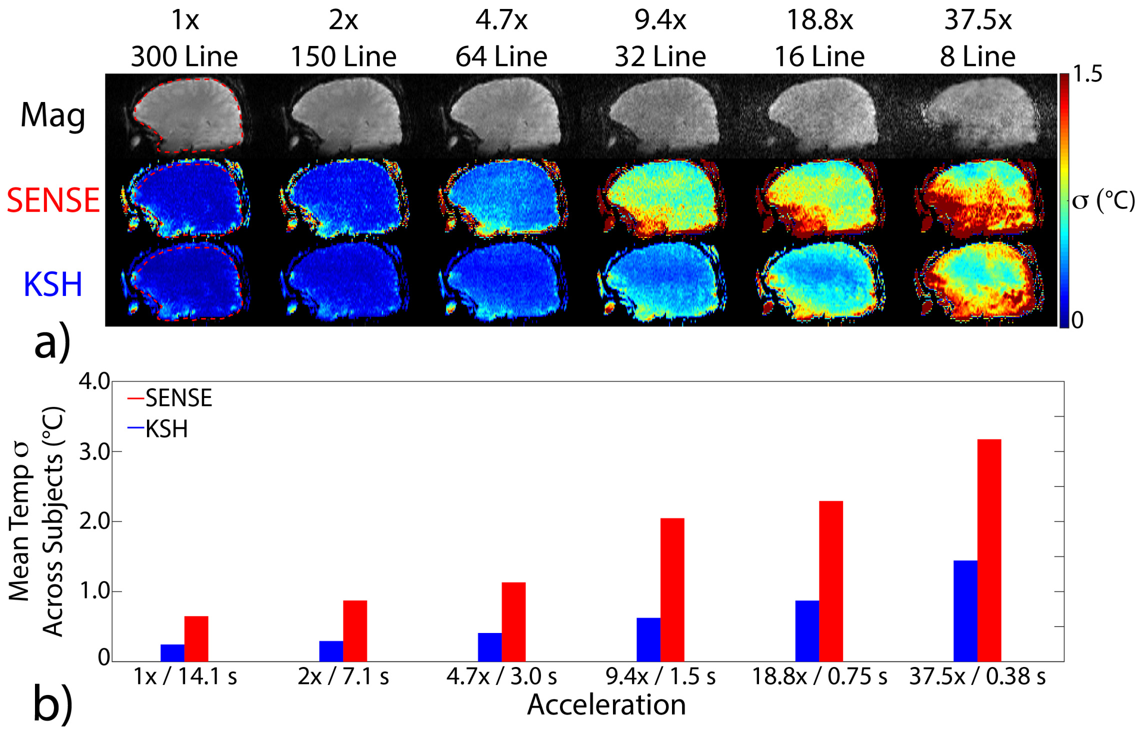

Figure 3.3: In vivo temperature precision (σ) versus acceleration factor/dynamic scan time, for a TR of 47 ms. (a) Brain magnitude images and through-time temperature standard deviation maps in one of the five volunteers are shown across acceleration factors, from 300 lines (no acceleration/14.1 s per dynamic) to 8 lines (37.5× acceleration/0.38 s per dynamic), using CG-SENSE plus image domain hybrid (SENSE) and k-space hybrid (KSH) reconstruction methods. Images are cropped A-P to display the central 22.0 cm FOV. (b) Temperature standard deviation versus acceleration factor, calculated over the brain volumes of 5 subjects. Standard deviations were calculated from brain tissue only using an automatic brain segmentation algorithm. The ROI for the subject in (a) is outlined in the 1×/no acceleration column.

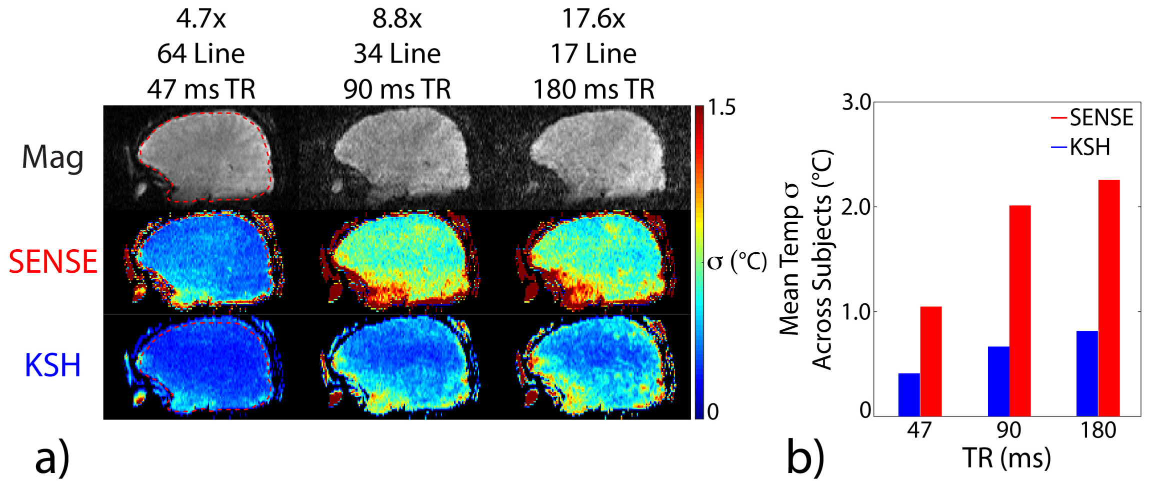

Figure 3.4: In vivo temperature precision versus TR with a fixed dynamic scan time of 3 seconds (varying acceleration). (a) Brain magnitude images and through-time temperature standard deviation maps using CG-SENSE plus image domain hybrid (SENSE) and k-space hybrid (KSH) reconstructions in one of the five volunteers across TRs (47, 90, and 180 ms). Images are cropped A-P to display the central 22.0 cm FOV. (b) Temperature standard deviation versus TR, calculated over the brain volumes of 5 subjects. The ROI for the subject in (a) is outlined in the 47 ms TR column.

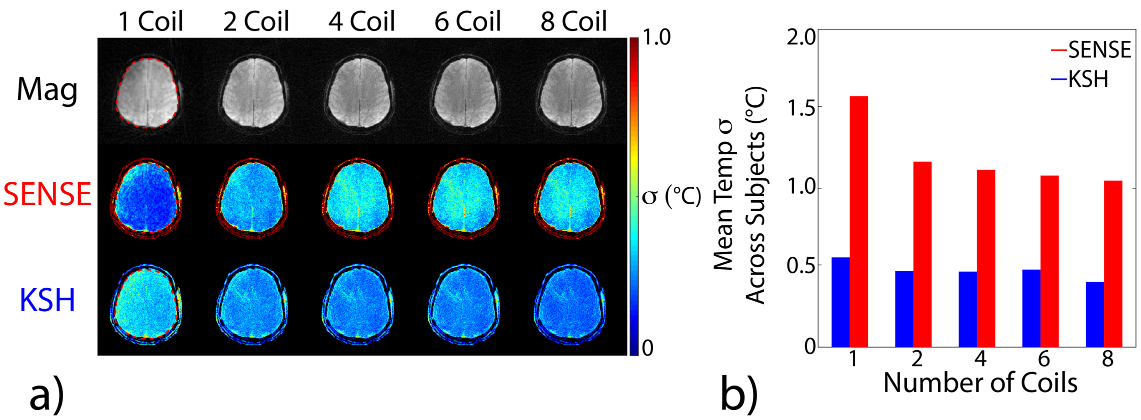

Figure 3.5: In vivo temperature precision versus number of receive coils, for TR 47 ms and 4.7× acceleration, corresponding to 3 seconds/64 radial lines per dynamic. (a) Brain magnitude images and through-time temperature standard deviation maps in one of the five volunteers across the number of receive coils. Images were cropped A-P and R-L to display the central 22.0 cm FOV. (b) Temperature standard deviation versus number of coils, calculated over the brain volumes of 5 subjects. The ROI for the subject in (a) is outlined in the 1 coil column.

per °C, so the expected pixel shifts also improve with more shots (25.1°C/px with single-shot EPI, 48.7°C/px with two shots, 78.0°C/px with three shots). An axial slice positioned for monitoring MRgFUS thalamotomy (red arrow) is also shown, which contains no visible distortions around the thalamus with any number of shots.

3.4.2 Phantom heating experiments

Figure 3.8 shows phantom images and temperature maps acquired during focused ultrasound sonication across acceleration factors, and Figure 3.9 plots k-space hybrid-reconstructed temperature in the hottest voxel versus time with no acceleration/14.1 seconds per image, and 4.7× acceleration/3.0 seconds per image. k-Space hybrid peak heat temperature maps perpendicular to the ultrasound beam in 3D SoS EPI are very similar up to acceleration factors of 37.5× (8 lines per dynamic or 0.38 s). CG-SENSE plus image domain hybrid temperature maps are also similar up to an acceleration factor of 4.7× (64 lines per dynamic or 3.0 s), but due to undersampling of the higher spatial frequencies, the hot spot is blurred out and temperature is underestimated at higher factors. Figure 3.9 shows that the longer reconstruction window of the 300-line k-space hybrid reconstruction blurs out the temporal evolution of the hottest voxel's temperature, which in particular results in a higher initial temperature and a lower peak temperature (34.9°C versus 36.2°C)

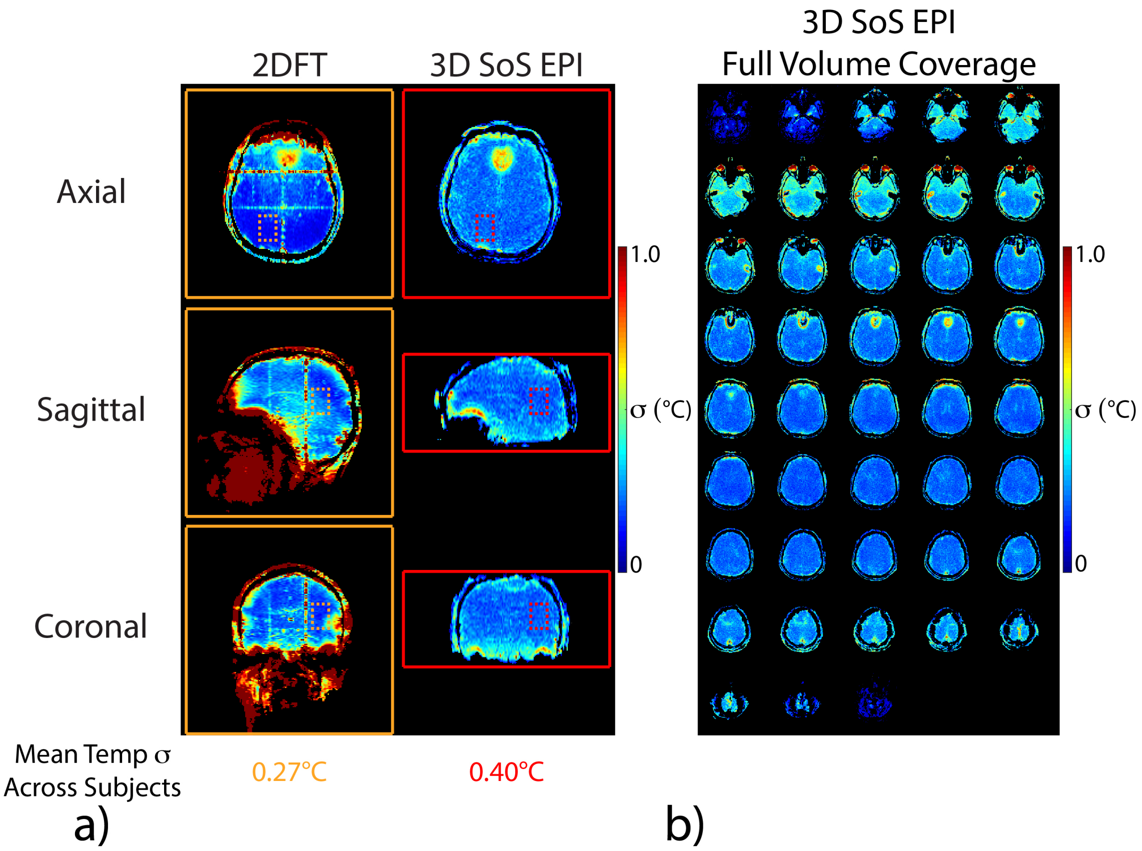

Figure 3.6: In vivo temperature precision and spatial coverage of 3D SoS EPI compared to standard 2DFT single-slice temperature mapping. (a) Through-time temperature standard deviation maps in one of five volunteers from each sequence, in axial, sagittal, and coronal slice orientations. 3D SoS EPI maps were reconstructed at a 3.3 second dynamic scan time matched to 2DFT (4.3× acceleration factor/69 radial lines per dynamic). Images were not cropped; solid lines indicate the FOV of each acquisition. Temperature standard deviation calculated over all 5 subjects was 0.4°C for 2DFT and 0.27°C for 3D SoS EPI. For 2DFT, temperature standard deviation was calculated in ROIs (dashed lines) that excluded artifacts and brain edges. (b) Illustration of the overall brain coverage of the 3D SoS EPI sequence, displayed in axial orientation.

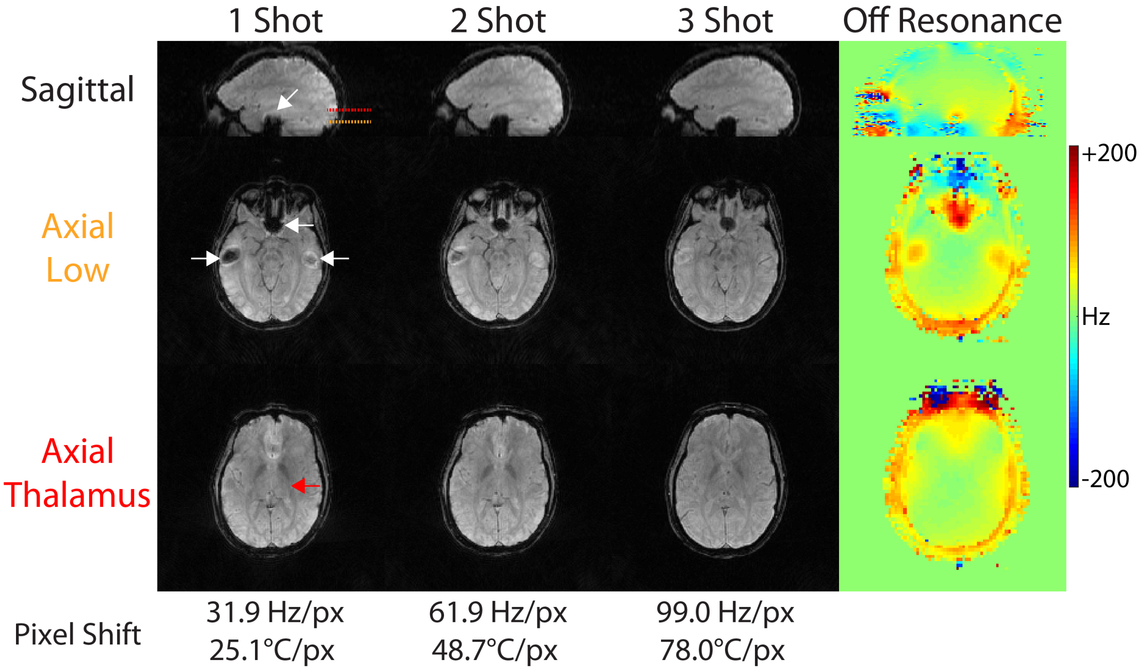

Figure 3.7: Minimizing in vivo off-resonance distortions in 3D SoS EPI with multishot acquisitions. Due to its relatively low pixel bandwidth in the EPI phase-encode dimension (31.9 Hz), single-shot EPI suffers from signal dropouts in regions with large off-resonance, such as near the sinuses (white arrows). This is mitigated when the 3D SoS EPI readout is divided into multiple shorter shots. There are no visible distortions at any multishot factor in the region targeted for thalamotomy (red arrow).

compared to a 64-line reconstruction.

3D SoS EPI and 2DFT temperature maps in a plane parallel to the ultrasound beam are compared in Figure 3.10a, and profiles through the middle of the hot spot in each dimension are plotted in Figure 3.10b. 3D SoS EPI maps are shown with and without chemical shift (CS) compensation in the EPI phase encode dimension (the vertical dimension in Figure 3.10a). The full width at half maximum of the hot spot was 11.5 mm parallel to the beam/3.7 mm perpendicular to the beam for 2DFT (peak temperature 33.3°C), 13.1 mm parallel/4.2 mm perpendicular for 3D SoS EPI (peak temperature 34.4°C), and 13.1 mm parallel/4.1 mm perpendicular for 3D SoS EPI after CS correction (peak temperature 34.5°C). The differences in full width at half maximum between 3D SoS EPI and 2DFT are less than the encoded voxel size in each dimension, and are likely due to a slightly wider imaging point spread function for the 3D SoS EPI reconstructions. As expected, chemical shift correction shifted the hot spot by approximately one voxel (2.75 mm) in the phase encode dimension, so that its peak better lined up with the 2DFT temperature profile, which was acquired with a higher pixel bandwidth (60 Hz/px or 47.2°C/pixel

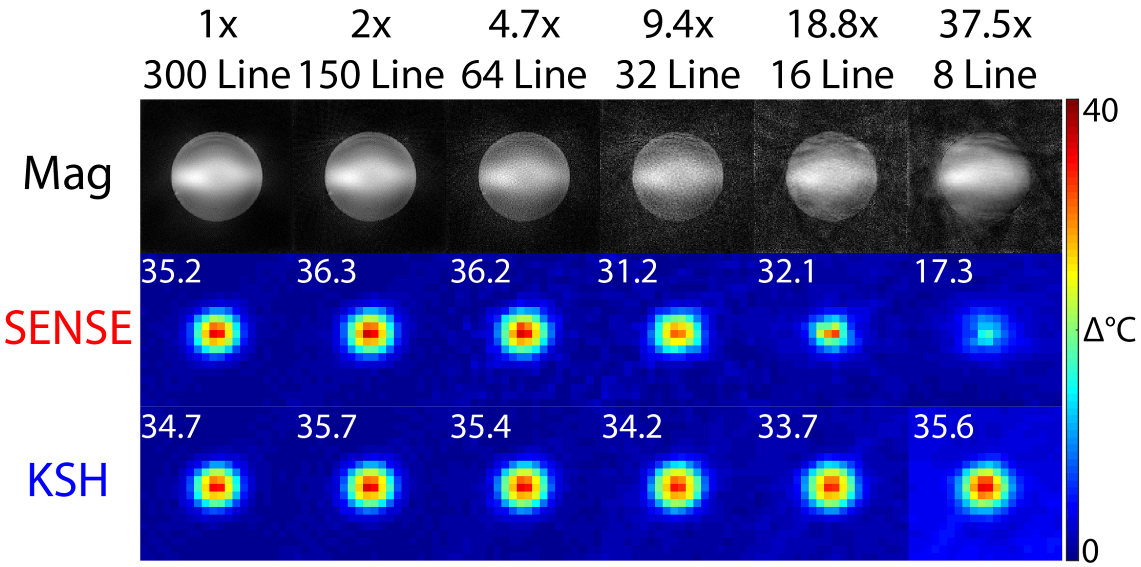

Figure 3.8: Phantom heating versus acceleration factor. Peak heat temperature maps perpendicular to the ultrasound beam reconstructed across acceleration factors, from 300 lines (no acceleration/14.1 s per dynamic) to 8 lines (37.5× acceleration/0.38 s). The inset numbers report peak temperature in the hottest voxel for each reconstruction. Temperature maps were cropped F-H and R-L to display the central 9.5 cm FOV. Magnitude images were not cropped and display the entire 28.0 cm.

in 2DFT vs. 31.9 Hz/px or 25.1°C/pixel in 3D SoS EPI). The Supporting Information Video shows entire 2DFT and 3D SoS EPI time series temperature maps, and can be downloaded from https://bitbucket.org/wgrissom/epi_stackofstars_thermometry. The top row in the video shows maps from a single 3D SoS EPI slice matching a 2DFT slice taken parallel to the ultrasound beam. A maximal intensity projection volume rendering of the 3D SoS EPI acquisition volume is displayed with temperature overlaid in the bottom row, and is rotated over a range of viewing angles. With slice-parallel processing, each 3D SoS EPI volume took 3.4±0.8 s (averaged across dynamics) to reconstruct using CG-SENSE plus image domain hybrid; k-space hybrid took 80.7±14.2 s. Compute times were not recorded for the in vivo temperature error reconstructions since that version of the algorithm would not be used during treatment.

3.5 Discussion

3D SoS EPI combines non-Cartesian radial sampling in-plane and Cartesian EPI sampling through-plane. EPI in the slice dimension provides rapid slice sampling of a volume k-space. Successive EPI planes are spaced by the golden angle, producing radial spokes in a 3D stack-of-stars k-space. Golden angle spacing approximately evenly distributes radial spokes, regardless of the width of the

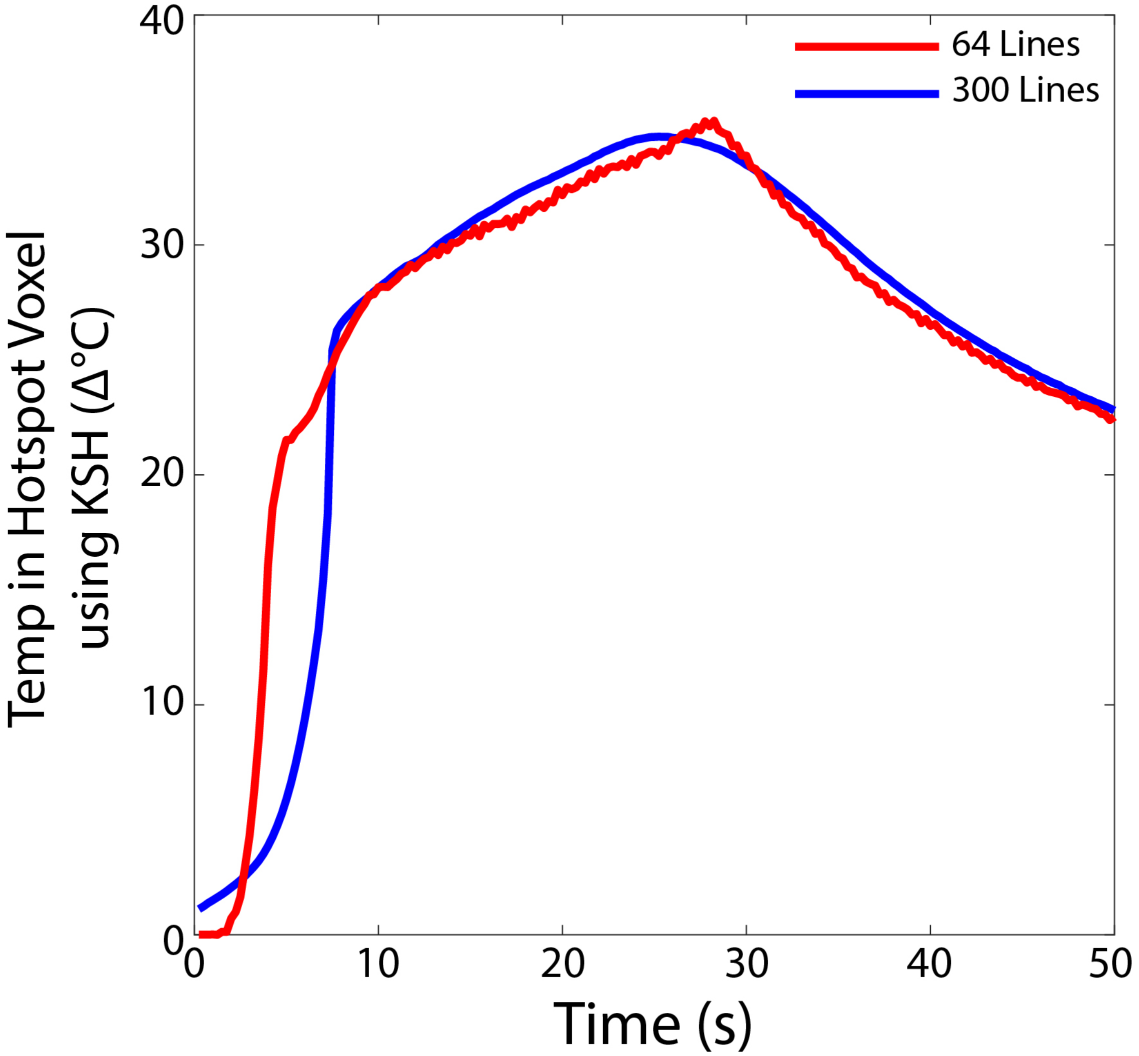

Figure 3.9: Phantom temperature curves for 300 lines (14.1 s per dynamic) and 64 lines (3 s per dynamic), in the hottest voxel.

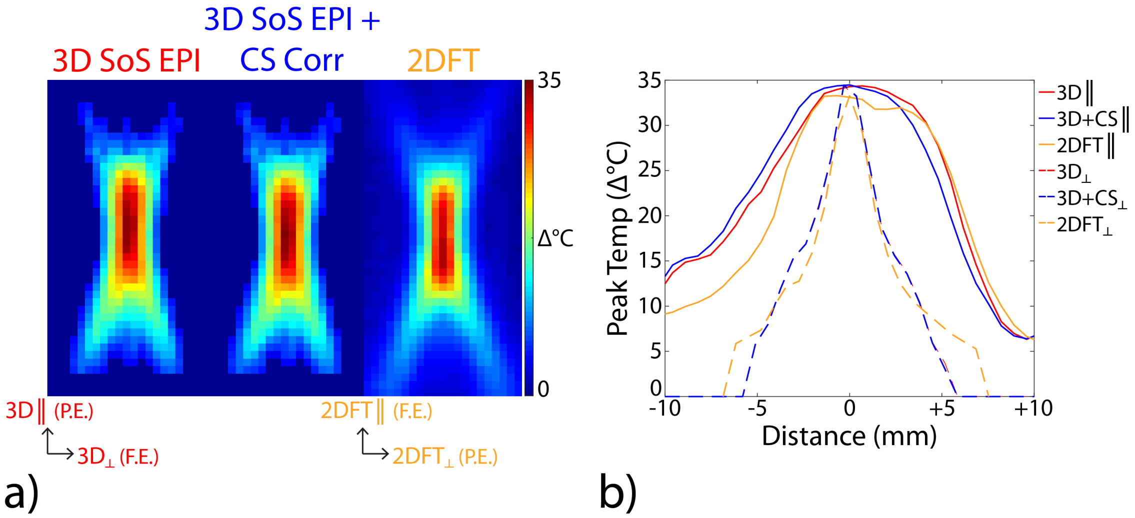

Figure 3.10: Phantom heating spatial profiles. (a) 3D SoS EPI and 2DFT peak heat temperature maps parallel to the ultrasound beam, which propagates in the vertical dimension. 3D SoS EPI maps are shown before and after CS correction, which is applied in the EPI phase-encode/vertical dimension. Temperature maps were cropped to display the central 5.4 cm × 2.3 cm FOV. The encoding directions for each pulse sequence are labeled and were chosen so that chemical shift artifacts accrued in the same direction in both scans (parallel to ultrasound beam propagation). (b) Heating profiles at peak heat in the center of the hot spot, parallel (∥) and perpendicular (⊥) to ultrasound propagation. CS correction shifted the 3D SoS EPI temperature profile by approximately one pixel (1.5 mm) in the parallel dimension.

reconstruction window [162]. This enables the length and position of the reconstruction window to be determined retrospectively. Furthermore, unlike 2DFT scans and conventional 3D EPI and spiral scans, 3D SoS EPI samples the center of k-space in every TR, so a sliding window reconstruction will not miss the peak of the heating curve (a clinically important parameter [97]). In this work, in vivo experiments characterized the dependence of temperature precision on acceleration factor, TR, and number of receive coils. Phantom heating experiments were also performed using a clinical MRgFUS system. Both sets of experiments compared the sequence to a standard single-slice 2DFT temperature mapping sequence.

Two approaches to reconstructing 3D SoS EPI temperature maps were compared. The first was CG-SENSE image reconstruction followed by image domain hybrid temperature estimation, and the second was the k-space hybrid method. The first approach comprised separate image reconstruction and temperature estimation steps, which is the more familiar and widely-available workflow. It also required less compute time than k-space hybrid, so it could be more readily implemented on a scanner for real-time use. However, its temperature uncertainty was always higher than k-space hybrid's, and its maximum acceleration was more limited. This is because CG-SENSE reconstructed a completely new image at each dynamic, without leveraging prior data. In comparison, k-space hybrid directly fits a phase-shifted fully-sampled baseline image to the k-space data. This resulted in lower errors due to undersampling and consequently lower temperature uncertainty. In practice, this translates to higher acceleration factors and/or the requirement of fewer receive coils, with the tradeoff of longer computation times. Thus, in the near term, CG-SENSE plus image domain hybrid reconstruction is better suited for real-time use with moderate acceleration, while k-space hybrid is better suited for retrospective use with higher acceleration. Temporally-constrained reconstruction may represent a middle ground between these two strategies [110].

In vivo experiments showed that k-space hybrid and CG-SENSE plus image domain hybrid temperature reconstructions achieved a temperature uncertainty better than or near 1.0°C up to a clinically representative dynamic scan time of 3 seconds [97], with k-space hybrid providing lower uncertainty at all factors and better than 1.0°C uncertainty down to a 0.75 second dynamic scan time. Temperature maps with no visible errors were also obtained with both methods down to a 3 second dynamic scan time in phantom MRgFUS heating experiments, with k-space hybrid providing high quality maps down to a 752 ms second dynamic scan time. We found that temperature uncertainty increased when TR was increased while maintaining a fixed 3 second dynamic scan time, suggesting that the benefit of higher signal with longer TRs is offset by the concomitant reduction in signal averaging and errors from increased k-space undersampling. The temperature precisions of the reconstructions were tolerant to a small number of receive coils, which is important since imaging in MRgFUS is presently receive coil-limited since the transducer must be closest to the body. Current clinical neuro MRgFUS systems either use a single-channel body coil for reception, or an eight-channel receive coil that sits outside the transducer and provides limited spatial encoding capability. As expected, the uncertainty of the reconstructions did increase as the number of coils decreased, though it remained better than 0.5°C.

MR thermometry for transcranial MRgFUS neurosurgery is currently based on a single-slice 2DFT sequence [97]. 3D SoS EPI (reconstructed at a matched dynamic scan time) achieved slightly worse temperature uncertainty (0.4°C across all subjects) than 2DFT (0.27°C), but this tradeoff enabled volumetric brain coverage and the uncertainty was still much better than 1.0°C. Furthermore, to our knowledge, no other temperature imaging sequence provides volumetric thermometry with equivalent spatiotemporal resolution. While scans were not performed with a clinical transcranial MRgFUS system in this work, the in-plane FOV of the 3D SoS EPI scan is large enough to accommodate the water bath of the ExAblate Neuro system (InSightec Ltd., Haifa, Israel), and matched the FOV of the 2DFT scan which was set based on that system. The in vivo comparison to 2DFT also indicated that 3D SoS EPI may be less sensitive to brain and blood pulsations, though due to its lower through-slice bandwidth it may be more sensitive to off-resonance changes caused by motion such as nodding, which changes the off-resonance distribution around the sinuses. However, in practice MRgFUS treatments use a stereotactic frame to immobilize the head which minimizes such motion. Since our experiments were not performed with a clinical transcranial MRgFUS system, we cannot make absolute assertions about 3D SoS EPI temperature standard errors for actual systems. We expect that errors would be larger on actual systems, principally due to larger distances between receive coils and the head. However, one can reasonably expect that the relative performance of 3D SoS EPI to single-slice 2DFT (the standard clinical sequence) would be preserved when moving to a clinical system.

A weakness of the present implementation of 3D SoS EPI is its relatively low pixel bandwidth in the phase encode dimension, which in the present study was the head-foot dimension. This led to through-plane distortions in brain regions above the sinuses and ear canals, and a shift (approximately one pixel) of the peak of the hot spot in the phantom experiment. As demonstrated, these distortions and hot spot shifts are most easily addressed using multishot scans, which increase pixel bandwidth by a factor equal to the number of shots. However, this comes at the cost of scan time. If multiple receive coils are available across the slice dimension, parallel imaging acceleration in that dimension would also increase pixel bandwidth by a factor equal to the acceleration factor. This would either necessitate a full 3D image/temperature reconstruction, or a k-space-domain parallel imaging reconstruction such as GRAPPA to fill in missing data in the phase encode dimension prior to in-plane radial reconstruction [178]. We also demonstrated that a previously-described chemical shift compensation method can correct hot spot displacement in the slice dimension. Real-time implementations of that algorithm are available [163]. Another possible source of 3D SoS EPI image and temperature map distortions is readout delays and line-to-line phase shifts that cause ghosting in the phase encode dimension. These were addressed in the current implementation by acquiring non-phase-encoded reference scans for each EPI plane and estimating correction terms from them that were applied to the phase-encoded data [174]. Though it was not observed in the current implementation, radial scans also often suffer from trajectory errors that cause projections to miss the center of k-space. These could be compensated using an automatic trajectory correction method that estimates the errors from the data itself, based on data consistency between projections [179, 180]. Finally, we note that Svedin et al have also explored 3D golden angle radial acquisitions for MR thermometry [181, 182]. Specifically, they developed a 3D golden angle acquisition for thermometry in the breast. Compared to the 3D SoS EPI scan described here, the authors traded off volumetric coverage for the ability to separate water and fat images and measure T_2^*, which may enable thermometry in fat. They used the phase at the center of k-space for respiration correction, and reconstructed images using a radial keyhole technique; the same reconstruction could be applied to 3D SoS EPI.

3.6 Conclusion

We proposed and validated a hybrid radial-EPI temperature mapping pulse sequence that can acquire temperature maps with volumetric brain coverage and 1.5 mm × 1.5 mm (in-plane) × 2.75 mm (through-plane) spatial resolution. High frame rates can be obtained using either the k-space hybrid temperature reconstruction method or a standard CG-SENSE plus image domain hybrid method.

Chapter 4

Optical tracking-guided MR-ARFI for targeting ultrasonic neuromodulation

4.1 Abstract

Purpose:

To implement MR-acoustic radiation force imaging (MR-ARFI) for targeting transcranial magnetic resonance-guided focused ultrasound (MRgFUS) neuromodulation experiments in living non-human primates.

Methods:

A spin echo magnetic resonance-acoustic radiation force imaging (MR-ARFI) pulse sequence was implemented at 7 Tesla for imaging the acoustic pressure field from a single-element transcranial MRgFUS transducer operated at 802 kHz. An optical tracking system was used to project the estimated location of the beam onto pre-acquired images of the target. The motion-encoding gradients (MEGs) were aligned with the ultrasound propagation axis, and the imaged slice was prescribed at the location of the acoustic focus obtained via optical tracking. Displacement images were acquired in a tissue-mimicking phantom with the transducer rotated in six different configurations to simulate targeting in vivo. We then used optical tracking to project the estimated location of the beam onto pre-acquired images of two healthy adult female macaque monkeys (M fascicularis) and target the transducer to the right somatosensory network (S1 areas 3a/3b) through intact skull. Displacement images were acquired to verify transcranial ultrasound delivery prior to ultrasonic neuromodulation experiments performed with low frequency FUS at 250 kHz.

Results:

The method was validated in phantoms, which showed that MR-ARFI-derived displacement sensitivity is maximized when the MR-ARFI MEGs were maximally aligned with the FUS propagation direction across several different transducer configurations. MR-ARFI scans showed evidence of focal displacements in the targeted brain region in vivo, which scaled with acoustic power (0.49-

1.20 μm). When the MEGs were oriented off-axis, the measured displacement was reduced, suggesting that proper MEG alignment is required to optimize transcranial displacement sensitivity. Subsequent functional MRI (fMRI) scans showed activation in areas corresponding to positive MR-ARFI signal.

Conclusion:

Optical tracking-guided MR-ARFI is a feasible beam localization method for targeting ultrasonic neuromodulation experiments in living subjects.

4.2 Introduction

Advances in the field of neuromodulation have provided researchers with tools for examining how widespread brain circuits contribute to normal human behavior, and how they may be altered in the setting of neuropsychiatric disease [183]. Transcranial focused ultrasound (FUS) has the potential to become a highly specific, non-invasive technology for neuromodulation [10]. FUS uses an ultrasound transducer to generate high acoustic pressures at a focused location, without affecting intervening tissue. Recent preclinical studies [184] and early human trials [5–8] have shown that ultrasound can selectively alter neuronal activity, depending on sonication parameters like frequency and exposure time [185]. As a neuromodulation technology, FUS is unique in that it is both highly specific and non-invasive. The focus location is determined by the transducer geometry and can be positioned and steered electronically without repositioning the subject or hardware. Unlike other neuromodulation technologies, FUS can be integrated with magnetic resonance imaging (MRI) scanners for image guidance and combined functional magnetic resonance imaging (fMRI) and neuromodulation [186]. MRI-guided transcranial FUS is already FDA-approved for ablative thalamotomy in essential tremor [2, 158].

Prior to applying FUS, knowledge of the location of the acoustic focus must be obtained to verify that the ultrasound beam is reaching its intended target. For ablative procedures, small temperature rises in the target tissue tracked with MR thermometry pulse sequences have been used to determine where the FUS beam is within the brain [13]. However, off-target heating in the near- and far-fields of the ultrasound transducer can have deleterious effects [52, 187]. Human brain function is also known to be sensitive to fluctuations in brain temperature [188]. Given these concerns, a beam localization method that does not rely on temperature increases is desirable for FUS applications. For example, optical tracking has been used to target the FUS beam [186, 189, 190]. Optical tracking is used to determine the location of the ultrasound transducer relative to the targeted location, so that the estimated location of the acoustic focus (e.g., based on focal length or optically tracked hydrophone measurements in a water tank) can be projected onto an image of the target. This method does not require any energy to be deposited in the brain. However, it requires a pre-acquired anatomical image of the subject to be registered to the subject's anatomy in situ. Errors introduced in this registration step propagate to the targeted location of the beam, which could be significantly displaced if misregistration occurs. Also, these methods do not not account for aberrations that may be induced by the skull. Simulations of the FUS transmitting through the skull can be performed with CT-derived acoustic property maps to estimate the focus location [126]. However, these parameter maps are both subject skull-specific [51] and also depend on the X-ray energy and reconstruction kernel of the measured Hounsfield units (HU) [147]. Additionally, accurate simulations can require long computation times.

MR-acoustic radiation force imaging (MR-ARFI) pulse sequences can localize the acoustic focus prior to FUS procedures [76]. In MR-ARFI, motion-encoding gradients are used to encode the tissue displacement response to a short ultrasound excitation ($\approx$ ms) into the phase of an MR image. The acoustic radiation force is proportional to the local acoustic intensity of the ultrasound beam, so monitoring displacement via MR-ARFI provides a non-invasive tool to both localize the acoustic focus and to calibrate beam intensity. Unlike current beam localization methods, which predict the focus location based on simulations that are registered to the experiment, MR-ARFI is non-parametric and does not require a priori knowledge of skull acoustic properties, but rather can localize the beam in situ prior to any FUS application. MR-ARFI-derived displacement measurements have been validated in small animal in vivo studies, with ultrasound imaging-derived measurements as the gold standard [77]. Also, ex vivo studies in human cadavers have shown that sufficient sensitivity to displacement can be achieved beyond intact skull with MR-ARFI using commercial transcranial FUS transducers [142].

The goal of the present study is to detect and visualize the transcranial FUS beam with MR-

ARFI in living non-human primates. To maximize displacement sensitivity, we developed an optical tracking method to ensure that the MR-ARFI motion-encoding gradients are aligned with the FUS propagation direction and with the imaged slice prescribed at the optically tracked location of the acoustic focus. The methods described here address the need to determine the precise location of the FUS beam's interaction with brain tissue during transcranial FUS stimulation, and are generally applicable to all transcranial FUS procedures. We present these methods in the context of minimizing FUS exposure during FUS neuromodulation, where freely moveable transducers are increasingly being used and have created a need to image the estimated focal location with MR-ARFI. Notably, this study was informed by simulations of pressure fields and thermal deposition in the skull and brain prior to implementation, which are discussed in published aspects of this work [95].

4.3 Methods

4.3.1 Pulse sequence

All MR imaging was performed on a 7 Tesla Philips Achieva human research scanner (Philips Healthcare, Best, NL). Displacement images were acquired using an optically tracked 2D spin echo MR-ARFI pulse sequence, which is shown in Figure 4.1. Unipolar trapezoidal motion-encoding gradients (MEGs) were placed before and after the refocusing RF pulse to generate ARFI contrast [76]. The MEGs were set to 3 ms in duration and with maximum gradient strength (40 mT/m) on their plateaus, which resulted in low diffusion-weighting (b-value $\approx$ 9.3 s/mm). Imaging parameters were: 12.0×12.0 cm^2 FOV; 60×60 matrix; 2.0×2.0 mm^2 voxel size; 1 slice; 2.0 mm slice thickness; echo time (TE)/repetition time (TR) 17/1000 ms; 2D multi-shot echo-planar imaging (EPI) readout with 5 lines per TR. A custom 6 cm surface coil integrated with the transducer's coupling cone was used for transmit/receive.

In each TR, a TTL pulse was sent from the scanner to the FUS waveform generator to trigger a sonication. Sonications were synchronized with the rewinder MEG using a trigger offset of -2 ms to allow displacement to reach a steady state [84]. Sonications were performed at 802 kHz for 4.5 ms (3609 cycles) with an acoustic pressure (maximum free field of 2.81 MPa) that would not be expected to exceed a temperature increase greater than 1 °C or MI greater than 1.1 within the

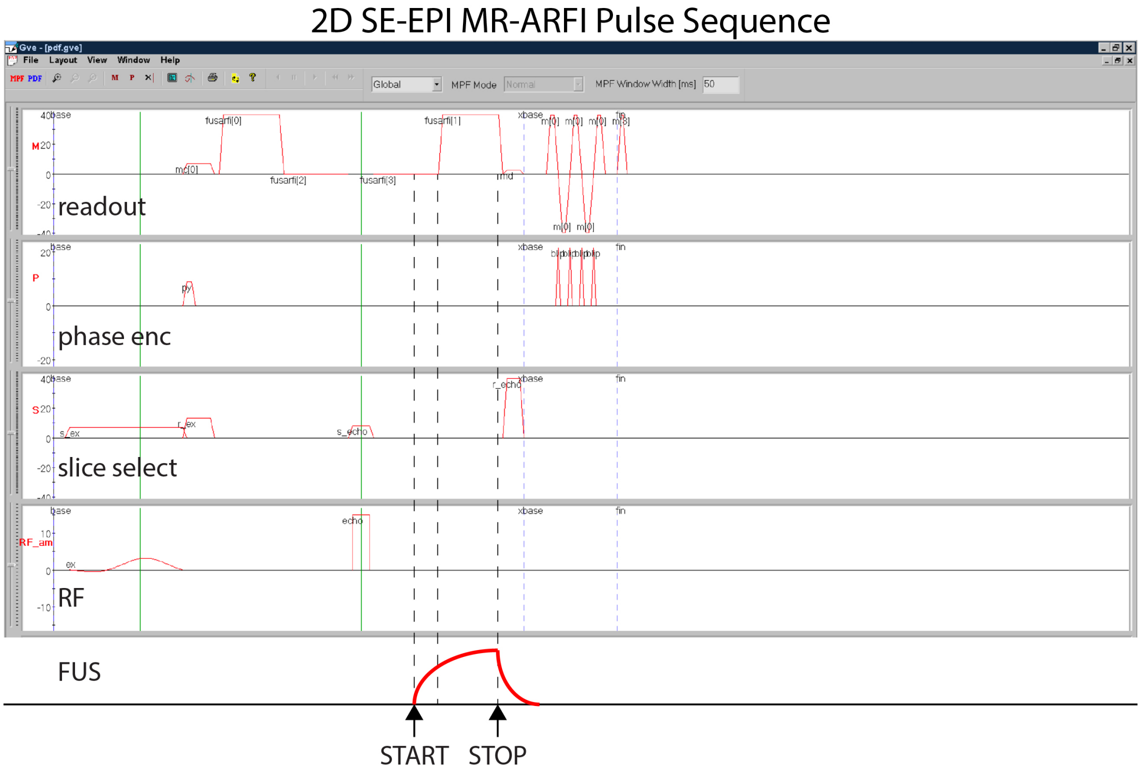

Figure 4.1: 2D SE-EPI MR-ARFI pulse sequence (Philips PPE Output). Displacement images were acquired using an optically tracked 2D spin echo-echo-planar imaging (SE-EPI) MR-ARFI pulse sequence. Unipolar trapezoidal motion-encoding gradients (MEGs) were placed around the refocusing RF pulse to generate ARFI contrast. The MEGs were set to 3 ms in duration and with maximum gradient strength (40 mT/m). MEGs could be prescribed independently of the slice orientation, so that displacement could be encoded in any slice and along any direction specified by optical tracking. Sonications were synchronized with the rewinder MEG using a trigger offset of -2 ms to record displacement in a steady state. Four phase images with switched polarity MEGs and with or without a sonication were acquired to reconstruct one displacement image, which took 4.0 minutes to acquire.

brain based on acoustic simulations and hydrophone experiments described elsewhere [95].

Four phase images with switched polarity MEGs and with or without a sonication were acquired in an interleaved fashion ($\phi_{\text{FUS On}+}$, $\phi_{\text{FUS Off}+}$, $\phi_{\text{FUS On}-}$, $\phi_{\text{FUS Off}-}$). Each phase image was acquired with five averages. Since the ultrasound PRF is specified by the TR of the pulse sequence, we used a relatively long TR of 1000 ms (1 Hz PRF) to maintain a low duty cycle. In total, 120 sonications were performed at a duty cycle of 0.2%, with a total scan time of 4.0 minutes to produce one displacement image. Displacement images were reconstructed using complex phase subtraction ($\Delta x = \angle(\phi_{\text{FUS On}+} \cdot \phi^*_{\text{FUS Off}+} \cdot (\phi_{\text{FUS On}-} \cdot \phi^*_{\text{FUS Off}-})^*)/2\gamma G\tau$, where γ is the gyromagnetic ratio, G is the gradient strength, and τ is the gradient duration). Images were reconstructed offline in MATLAB 2017a (MathWorks, Natick, MA).

4.3.2 Optically tracked MRgFUS

Since the transducer is freely-movable and manually positioned over the targeted region, prescribing the MEGs for MR-ARFI requires precise knowledge of the slice offset and angulation of the transducer along the anterior-posterior (AP or ±x), right-left (RL or ±y), and superior-inferior (SI or ±z) cardinal axes. We used optical tracking to ensure that the MEGs were aligned with the FUS propagation direction and that the imaged slice was prescribed at the optically tracked location of the acoustic focus. Previous efforts have described how optical tracking can be used to estimate the focus location and target the FUS beam [96, 186]. This procedure uses a Polaris Vicra optical tracking system (Northern Digital Inc., Ontario, CAN). An MRI-compatible rigid body tracker is mounted to the patient bed and serves as the global reference location. Another body tracker is mounted to the transducer as the tracked location. Multimodality fiducial markers (IZI Medical Products, Maryland, USA) are placed near the focus location. The fiducials are localized in image space using a 3D fast spoiled gradient-recalled echo T1-weighted high-resolution isotropic volume examination (THRIVE) pulse sequence (voxel size $0.4 \times 0.4 \times 1$ mm^3, TE/TR 1.89 ms/4 ms). The fiducials are manually identified in the T1-weighted image stack using 3DSlicer (http://www.slicer.org/). In front of the optical tracking camera, the fiducials are localized in physical space using a reflective positioning stylus and recorded in 3DSlicer. Finally, these are registered to the fiducials' image locations, yielding a physical-to-image space transform. The transducer can then be freely rotated in physical space, with 3DSlicer reporting the slice offset and angulation required to prescribe the MR-ARFI scan with maximum displacement sensitivity.

4.3.3 Phantom experiments

To simulate the targeting of arbitrary brain regions with our optically tracked MR-ARFI pulse sequence, and to demonstrate the need to align the MR-ARFI MEGs with the FUS propagation direction via optical tracking, displacement images were acquired in an ex vivo agarose phantom designed to mimic brain tissue acoustic properties (1% agarose, 4% graphite, and 10% n-propanol in water). For these experiments, the transducer housing was rigidly attached to a cylindrical phantom mold, and the transducer-phantom apparatus was mounted on a plastic tabletop with a three-axis stereotactic frame. In this way, our sonications could be targeted in any physical orientation. Targeting of the transducer-phantom apparatus is demonstrated in Figures 4.2 and 4.3. To fabricate the phantom, 5 grams of food-grade agarose powder was added to a 450 mL beaker of cold water. The beaker was heated in a microwave until it boiled. Twenty grams of 400 grit graphite powder (Panadyne Inc, Montgomeryville, PA) was then added, and after about 5 minutes of cooling, 50 mL of n-propanol was added to the agarose-graphite phantom mixture. The transducer housing was partially filled with 1% agarose in water and allowed to set before the phantom mixture was poured into the housing and phantom mold. Displacement images were acquired using our optically tracked MR-ARFI pulse sequence after translating and rotating the transducer to a slice offset and angulation about the AP, RL, and/or SI cardinal axes. The transducer was positioned in one of six physical orientations: No rotation; 29° about SI only; 48° about SI only; 21° about RL only; 30° about SI and 25° about RL; and 34° about SI and 19° about RL. Four displacement images were acquired per transducer orientation: MEGs aligned along AP only; RL only; SI only; and aligned with the FUS propagation axis as determined by optical tracking.

4.3.4 In vivo experiments

Two healthy adult female macaque monkeys (M fascicularis) were scanned with the approval of the Institutional Animal Care and Use Committee (IACUC) at Vanderbilt University and in accordance with all relevant guidelines and regulations. For these experiments, a previously developed experimental platform for targeted ultrasonic neuromodulation in non-human primates was used [96, 186]. Animals were sedated and positioned in a three-axis stereotactic frame with consistent physiological monitoring for the duration of the experiments. The experimental setup is shown in Figure 4.4a. The location of the FUS beam was first determined using the optical tracking protocol described above (Sec 4.3.2), which is summarized in Figure 4.4b. This information was used to target the transducer on the right somatosensory network (S1 areas 3a/3b). Transcranial displacement images were acquired with our optically tracked MR-ARFI pulse sequence, ensuring that the MEGs were aligned with the FUS propagation direction and with the imaged slice prescribed at the optically tracked location of the acoustic focus. In one living macaque, we acquired additional displacement images aligned with the beam but with the acoustic pressure reduced by 20% and 40%, to provide an estimate of displacement sensitivity at low acoustic powers. As a negative

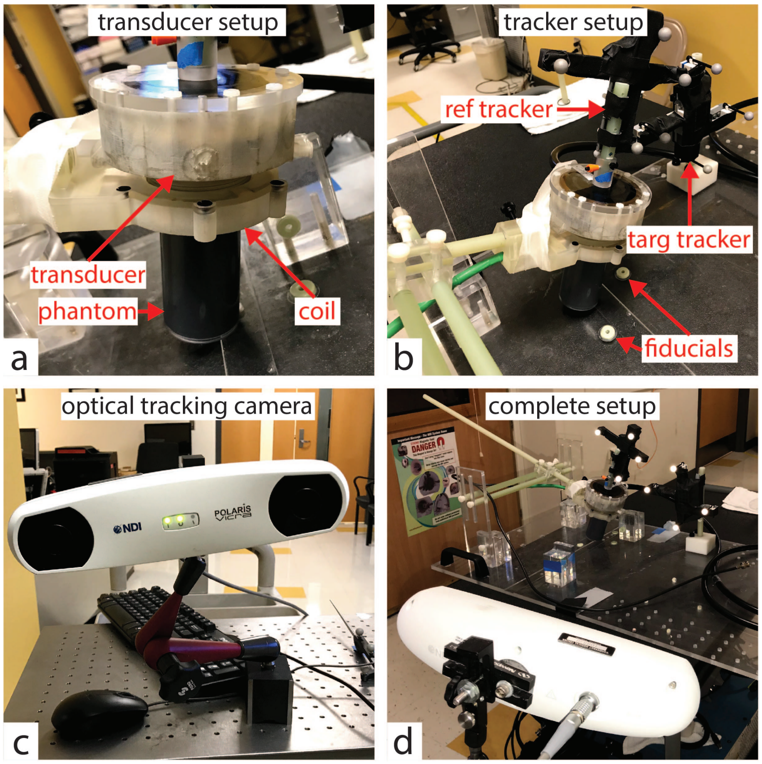

Figure 4.2: Optically tracked MR-ARFI in phantoms with simulated targeting. (A) To simulate the targeting of arbitrary brain regions with our optically tracked MR-ARFI pulse sequence, and to demonstrate the need to align the MR-ARFI MEGs with the FUS propagation direction via optical tracking, displacement images were acquired in an ex vivo agarose phantom designed to mimic brain tissue acoustic properties (1% agarose, 4% graphite, and 10% n-propanol in water). The transducer housing was rigidly attached to a cylindrical phantom mold, and the transducer-phantom apparatus was mounted on a plastic tabletop with a three-axis stereotactic frame. In this way, our sonications could be targeted in any physical orientation. (B) An MRI-compatible rigid body tracker is mounted to the patient bed and serves as the global reference location. Another body tracker is mounted to the transducer as the tracked location. Multimodality fiducial markers (IZI Medical Products, Maryland, USA) are placed near the focus location. (C) The optical tracking procedure uses a Polaris Vicra optical tracking system (Northern Digital Inc., Ontario, CAN). (D) The complete optical tracking-based targeting experimental setup is shown. In sight of the optical tracking camera, the location of the transducer is determined relative to the phantom, so that the estimated location of the acoustic focus (with the transducer location now known) could be projected onto pre-acquired images of the phantom.

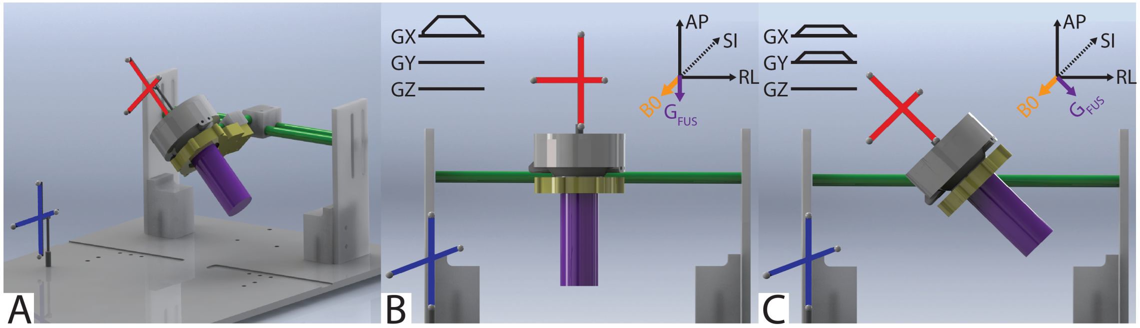

Figure 4.3: Targeting with an optically tracked FUS transducer. (A) A spherically-focused single-element FUS transducer (gray) was used to sonicate a tissue-mimicking brain phantom (purple). An MRI-compatible rigid body tracker was mounted to the patient bed (blue), and another body tracker was mounted to the transducer (red). As shown, the phantom mold was rigidly attached to the transducer housing. The transducer-phantom apparatus was mounted on a three-axis stereotactic frame (green) so that sonications could be performed in any physical orientation. (B,C) Demonstrate how the location of the transducer was obtained via optical tracking and used to align the MR-ARFI motion-encoding gradients (MEGs) with the FUS propagation direction (G_{FUS}).

control, we also acquired displacement images in one living macaque with the MEGs oriented off axis (i.e., 45° and 90° away from the FUS propagation direction). Displacement images without FUS application were also acquired as a negative control. Subsequent insonation of the somatosensory network with low frequency FUS was performed at 250 kHz, with concurrent functional MRI (fMRI) readouts of blood oxygenation level dependent (BOLD) signal in the targeted brain region. Details of the specific FUS stimulation paradigm follow previous work [186].

In a separate experiment, sonications were performed in one animal using the same acoustic parameters for MR-ARFI, but monitored with an MR thermometry pulse sequence to provide an in vivo estimate on brain temperature changes during MR-ARFI. Temperature images were acquired using a 2D gradient-recalled echo thermometry pulse sequence [13]. Imaging parameters were: 10.0 × 10.0 cm^2 FOV; 50 × 50 matrix; 2.0 × 2.0 mm^2 voxel size; 5 slices; 2.0 mm slice thickness; TE/TR 10/25 ms; 2D single-shot EPI readout. Temperature images were reconstructed in MATLAB using the hybrid multibaseline subtraction and referenceless method [170].

4.4 Results

4.4.1 Phantom experiments

To test whether optical tracking could predict MEG angle, we placed the transducer at varied angles relative to MEG direction and applied sound to a phantom known to absorb sound and

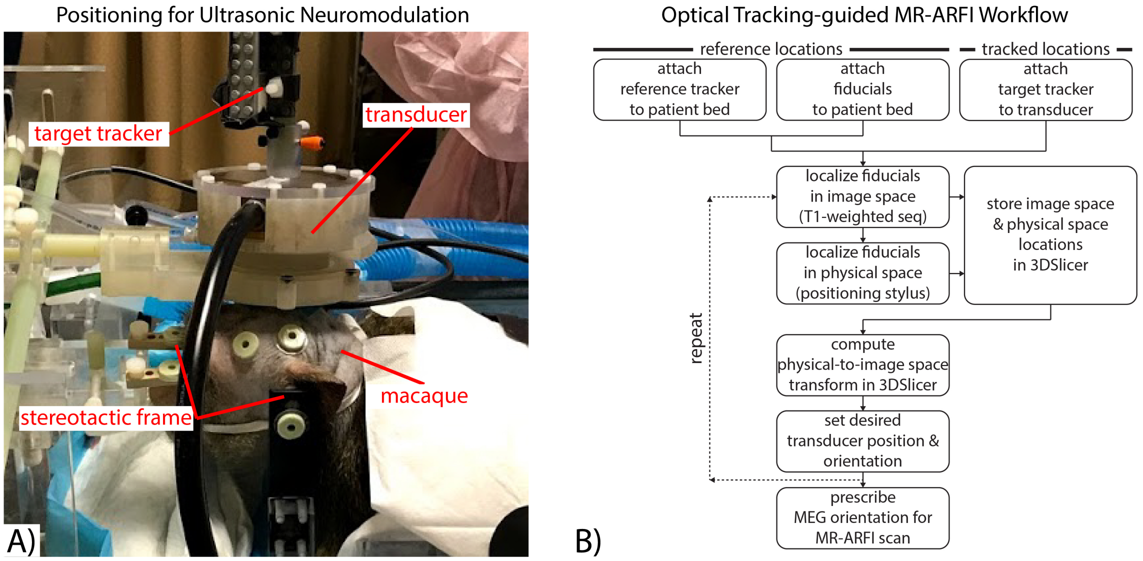

Figure 4.4: MR-guided ultrasonic neuromodulation experimental setup. (a) In vivo transducer positioning. With optical tracking guidance, the MRgFUS transducer was positioned to target the right S1 areas 3a/3b through intact skull of living macaque brain (M fascicularis). (b) Optical tracking protocol. Using 3DSlicer, a physical-to-image space transform was computed so that the location of the transducer could be determined in physical space relative to MRI coordinates. This information was used to prescribe MEG orientations parallel to the ultrasound propagation axis to maximally encode displacement via MR-ARFI.

deform similarly to tissue. Displacement maps acquired in the agar and graphite phantom using our optically tracked MR-ARFI pulse sequence in each MEG and transducer/phantom orientation show micron-scale displacement at the expected location of the ultrasound focus 4.5. Figure 4B reports mean focal displacements in a 3 × 3 pixel ROI at the focus for each MEG and transducer orientation pair. In every transducer orientation, the measured displacement was highest when the MEGs were prescribed along the FUS propagation direction using the optical tracking method. At matched acoustic output, the range of detected displacements was low when MEGs were prescribed via optical tracking (1.33-1.41 μm; mean ± SD = 1.37 ± 0.04 μm), suggesting that the optically-tracked alignment of the MEG can be used to improve SNR.

4.4.2 In vivo experiments

Figure 4.6 shows transcranial displacement images acquired using our optically tracked MR-ARFI pulse sequence in a living macaque. We measured a mean focal displacement of 1.20 μm at the highest acoustic power that was applied, which corresponds to a de-rated peak negative pressure (PNP) of 0.90 MPa in the brain (free-field PNP = 2.81 MPa). Using the MEG orientation deter-

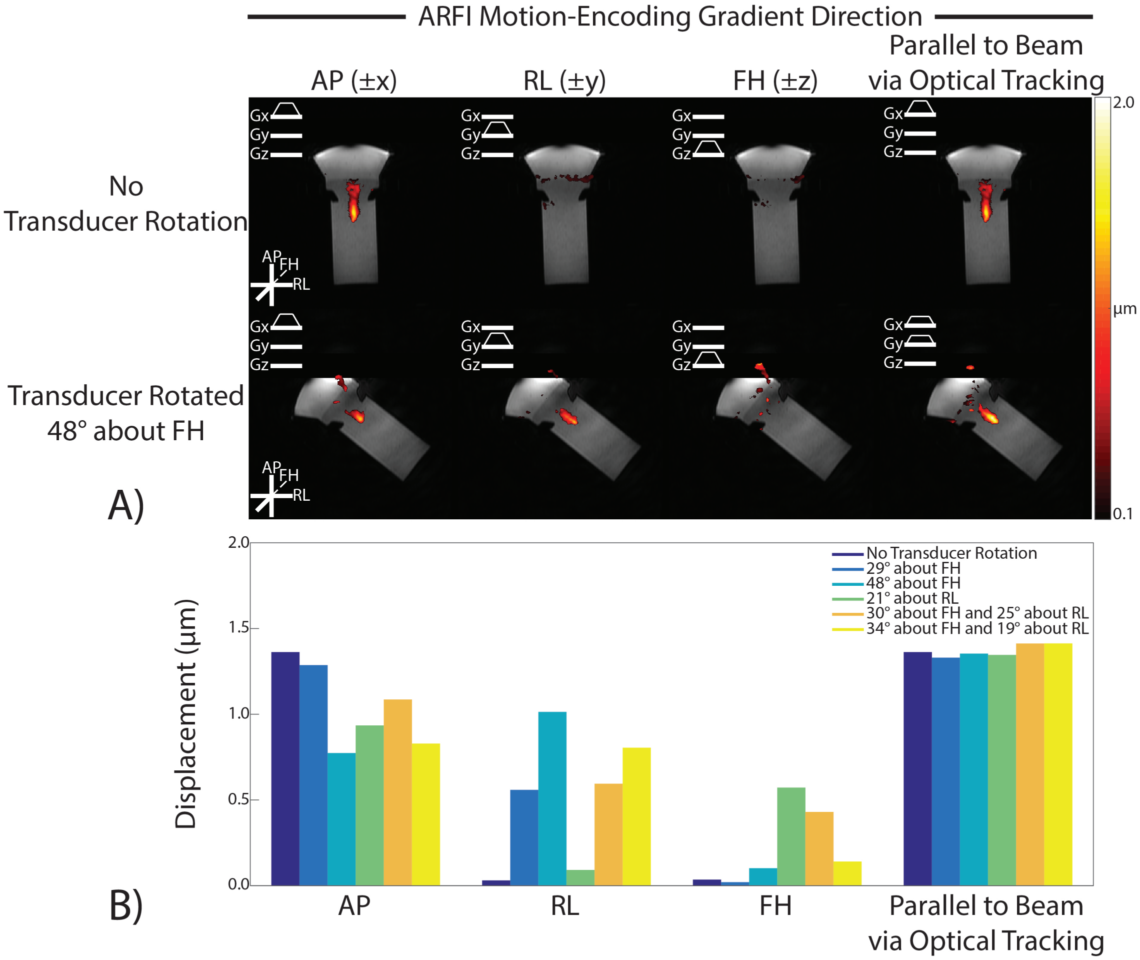

Figure 4.5: Optical tracking-based alignment of MR-ARFI motion-encoding gradients (MEGs) with the FUS propagation direction in a phantom. (A) MR-ARFI displacement maps for an oblique rotation of the FUS transducer. Maps were shown with the MEGs prescribed along the cardinal axes and along the optical tracking-determined propagation direction. (B) Mean displacement measured by MR-ARFI at the focus for each MEG orientation and each transducer rotation. The highest mean displacement is detected when the MEG is aligned with the FUS propagation direction obtained via optical tracking. Mean focal displacement was computed in a 3 × 3 px ROI at the acoustic focus.

mined by optical tracking, we reduced the power and measured decreasing displacement values to estimate the detection threshold during in vivo imaging with MR-ARFI. These results are shown in Figure 4.7. The smallest displacement we detected was 0.49 μm at a power level generating a de-rated PNP of 0.54 MPa in the brain (free-field PNP = 1.68 MPa). Negligible displacement was obtained in the negative control image, where no FUS was applied (0.09 μm). We acquired additional displacement images in one living macaque with the MEGs oriented away from the FUS propagation axis and a de-rated PNP of 0.72 MPa (free-field PNP = 2.25 MPa), which are shown in Figure 4.8. With the gradients rotated off-axis, the mean focal displacement decreased from 1.12 μm (parallel to the beam) to 0.14 μm (perpendicular to the beam).

A representative brain temperature image acquired in one living macaque at a de-rated PNP of 0.72 MPa (free-field PNP = 2.25 MPa) is shown in Figure 4.9a. A plot of the mean focal temperature is shown in red in Figure 4.9b. These results indicate that no significant brain temperature rise could be detected at the focus via MRI-based temperature monitoring when acoustic parameters designed for MR-ARFI were used. In the brain near the skull, we detected approximately a 0.2 °C rise. We did not observe macroscopic evidence of cavitation-induced skin lesions in either monkey in the region where FUS entered the skull.

Figure 4.10 illustrates the entire workflow of the proposed beam localization methods prior to ultrasonic neuromodulation experiments with concurrent fMRI readouts in the targeted brain region. Optical tracking-derived (in blue and yellow) and MR-ARFI-derived (in green) pressure maps are displayed as contours on a representative BOLD activation map during insonation of the somatosensory cortex at 250 kHz. Good spatial agreement was seen with both targeting methods and corresponded to areas with significant activation.

4.5 Discussion

Through simulation and phantom studies, we identified FUS parameters that can be used to transcranially induce displacements in brain tissue and developed methods to measure this displacement with MR-ARFI. We used this system to non-invasively localize the focus of a therapeutic FUS transducer by measuring ARF-induced displacements within a 4-minute scan time in living macaque brains at 7 T MRI. Our work demonstrates the feasibility of using MR-ARFI to map

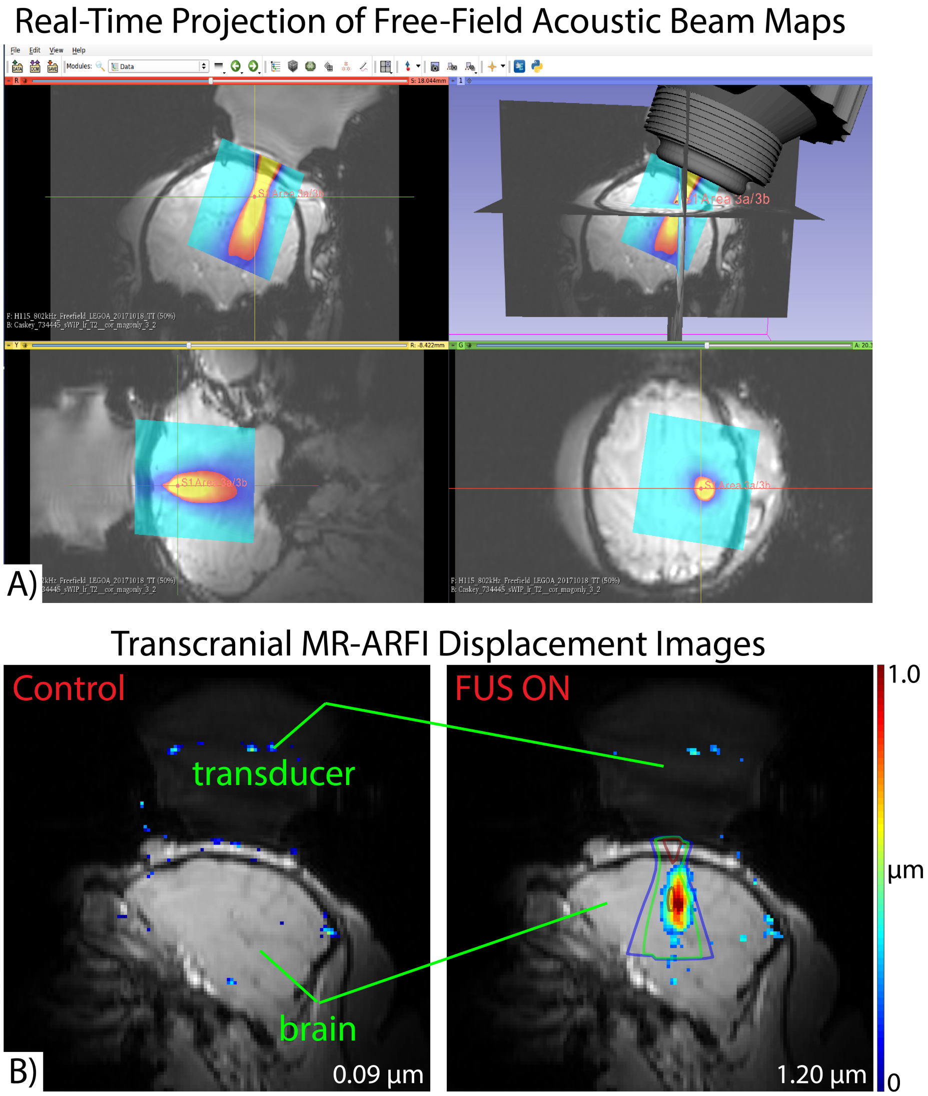

Figure 4.6: Targeting ultrasonic neuromodulation with optical tracking-guided MR-ARFI. (a) Real-time projection of free-field acoustic beam maps in 3DSlicer. A physical-to-image space transform was computed with optical tracking so that the free-field beam could be projected onto anatomical MRI images of macaque brain acquired in situ. This information was used to target the right S1 areas 3a/3b. No ultrasound was delivered during this part of the targeting procedure. (b) Representative transcranial MR-ARFI displacement images in one animal. MR-ARFI scans were performed targeting the right S1 areas 3a/3b in living macaque brain after insonation at a low duty cycle (0.2%). The acoustic focus can be observed in the displacement image with a peak value of 1.20 μm. Negligible displacement was observed in the control experiment without FUS application (0.09 μm). Free-field beam maps are overlaid in contours (thresholded at 5% (blue), 10% (green), and 25% (red) of peak pressure) and show good spatial agreement with MR-ARFI.

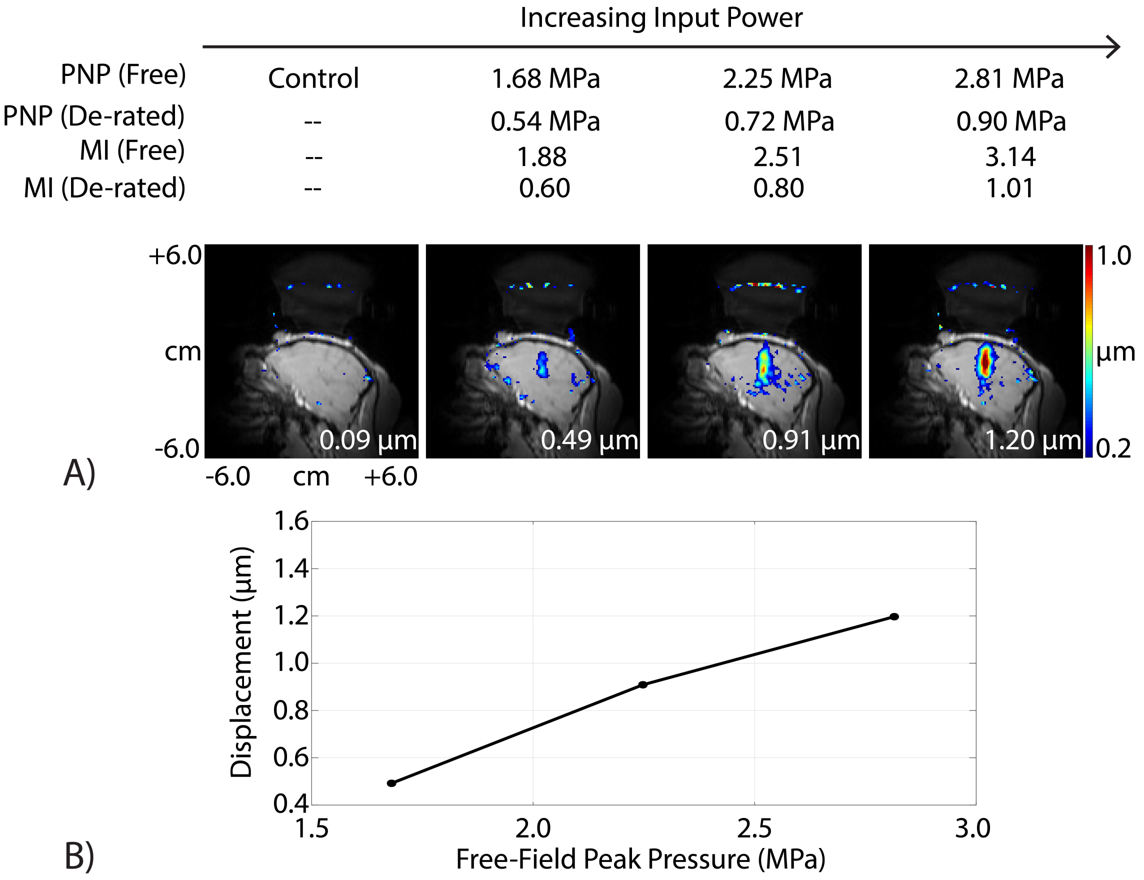

PNP (Free)	Control	1.68 MPa	2.25 MPa	2.81 MPa
PNP (De-rated)	--	0.54 MPa	0.72 MPa	0.90 MPa
MI (Free)	--	1.88	2.51	3.14
MI (De-rated)	--	0.60	0.80	1.01

Figure 4.7: Transcranial MR-ARFI displacement scales with input power. (A) Displacement images were obtained with our optically tracked MR-ARFI pulse sequence in vivo at different input powers. (B) Peak transcranial displacement shown as a function of input power. The measured displacement increased with increasing pressure. At the lowest pressure tested (estimated 0.54 MPa in the brain), a peak displacement of 0.49 μm was obtained. This demonstrates that detectable displacement is feasible at pressures that are not expected to generate cavitation in the brain.

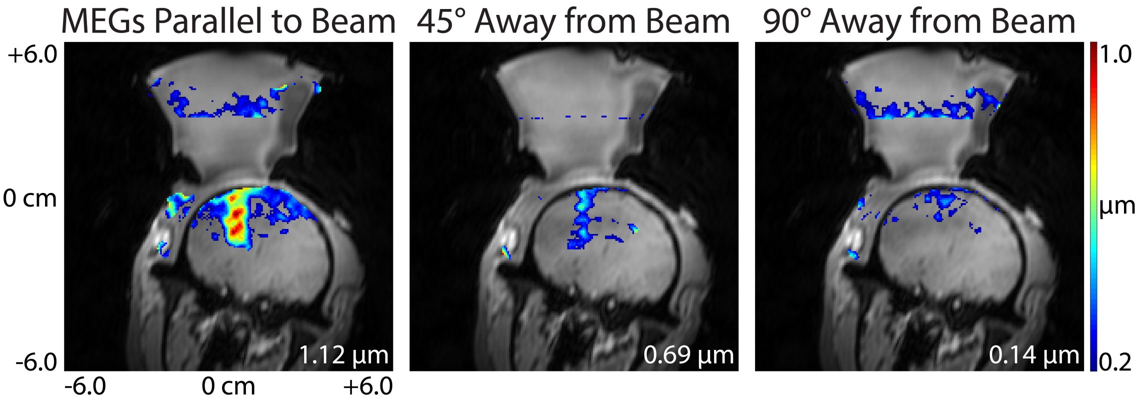

Figure 4.8: Optical tracking-based alignment of MR-ARFI MEGs with the FUS propagation direction in vivo. Displacement images were acquired with the MEGs aligned parallel to the beam (left), 45° away from the beam (middle), and 90° away from the beam (right). When the MEGs were prescribed off-axis, the measured displacement reduced, indicating that MR-ARFI requires proper MEG alignment to optimize displacement sensitivity.

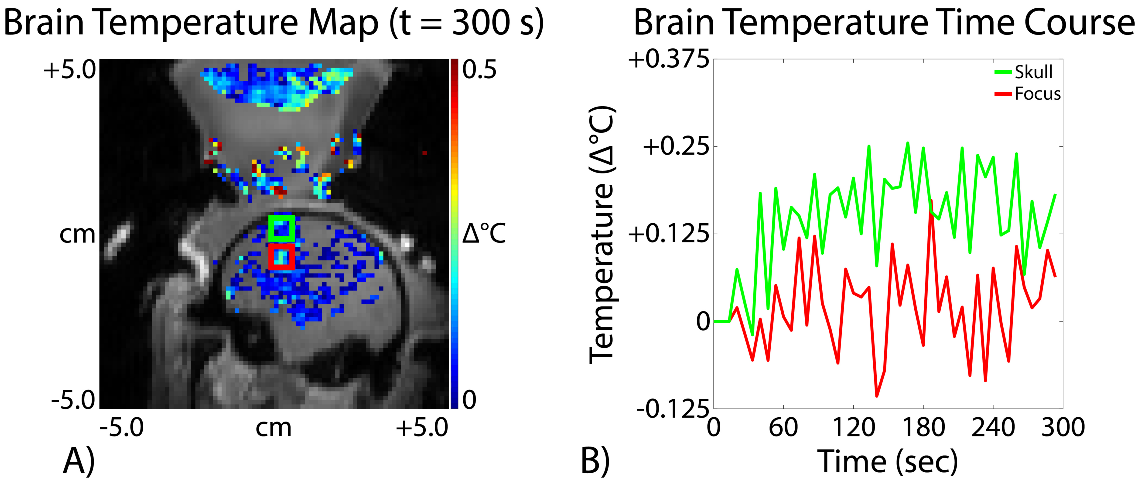

Figure 4.9: MR thermometry in a living macaque using MR-ARFI sonication parameters. (A) A representative in vivo brain temperature map shows that no significant temperature rise could be detected using sonication parameters designed for MR-ARFI. (B) The brain temperature time course at the acoustic focus (red) and near the skull (green) is shown. Mean focal temperature was computed in a 3 × 3 px ROI.

the FUS beam transcranially in a large animal and localize its focus in conjunction with structural imaging-based neuronavigation via optical tracking. Much prior work has established MR-ARFI in phantoms [76]; our study demonstrates transcranial MR-ARFI in a survival imaging session in the brain of a large animal with intact skull with surrounding tissues of skin, soft tissue, and muscle.

Localizing the ultrasound focus with MR-ARFI should ideally deposit as little FUS energy as possible. Maximizing sensitivity of the MR sequence allows for detection of smaller displacements for a fixed acoustic intensity. To encode micron-scale displacements, MEGs with high gradient strengths and long durations are required to accrue detectable phase shifts into the reconstructed MR-ARFI displacement image. To maximize sensitivity to the ARF-induced phase change, MR-ARFI is typically implemented by complex phase subtraction of two spin echo MR acquisitions obtained with switched polarity MEGs [76]. Additional subtraction of an acquisition without ultrasound application has been shown to minimize motion-induced phase contributions unrelated to the ARF (e.g., respiration) [81]. Echo-planar imaging (EPI)-based sequences have also been used to rapidly encode displacement images while minimizing ultrasound energy deposition [78]. In this work, we further developed the MR-ARFI pulse sequence using an optical tracking system to predict the transducer orientation so that the MR-ARFI MEGs could be pre-

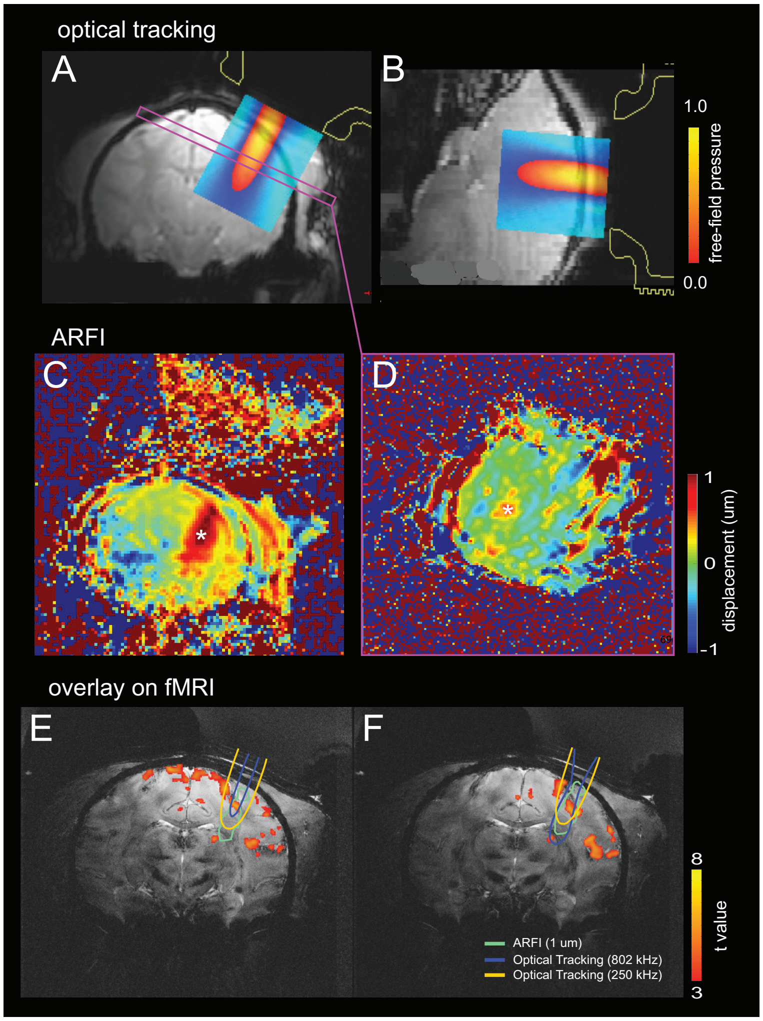

Figure 4.10: Beam localization methods for ultrasonic neuromodulation with concurrent fMRI readouts. (A) and (B) illustrate optical tracking-based targeting of the free-field acoustic beam on the targeted brain region, projected on (A) coronal and (B) sagittal brain slices of a pre-acquired anatomical MRI volume. No sonications are performed during this step. (C) and (D) show transcranial displacement images after insonation via MR-ARFI, encoded in (C) coronal and (D) axial brain slices which show the acoustic pressure field in situ. Our proposed MR-ARFI pulse sequence uses optical tracking to estimate the slice location of the acoustic focus and the angulation(s) of the beam propagation axis so that displacement can be maximally encoded along that direction. White asterisks indicate the acoustic focus location. (E) and (F) demonstrate good spatial agreement between displacement map contours (thresholded at 1.0 μm (light green)) and free-field beam map contours (thresholded at 50% peak pressure for the 250 kHz (yellow) and 802 kHz beams (blue)) in two separate T2*-weighted coronal brain slices with BOLD activation readouts shown during ultrasonic neuromodulation (thresholded at $t = 3$ (red)).

scribed along the FUS propagation axis and the slice could be located at the predicted focus. We showed in living macaques that knowledge of the transducer orientation can improve displacement sensitivity without requiring any additional sonications. In our experience, a spin echo multi-shot EPI acquisition strategy provided the best balance between scan time and image quality for our application. Previous efforts in MR-ARFI pulse sequence development might be considered for future directions. Both single-shot EPI [78] and steady-state free precession [85] pulse sequences have been proposed to further reduce scan time for MR-ARFI, though these acquisitions are highly sensitive to geometric distortions, especially at 7 T. Encoding schemes that use bipolar gradients [81] or alternating triggers to the transducer (i.e., triggering the sonication on either the forward gradient or the gradient rewinder) [83] have also been shown to improve phase stability. Volumetric imaging strategies for MR-ARFI have also been proposed [86, 87, 89]. A custom surface coil was used for transmit/receive due to the lack of an integrated body/volume coil in our 7.0 Tesla MRI scanner. We fabricated a 6 cm surface coil integrated with the transducer's coupling cone specifically for this imaging application so that the SNR would be maximized near the acoustic focus in the desired target location of our non-human primate subjects. In our in vivo MR-ARFI acquisitions, we obtained an SNR of 14.94 (where SNR = peak focal displacement/STD of noise displacement), which was sufficient to clearly observe the acoustic focus in vivo.

During the MR-ARFI sequence, a low duty cycle (e.g. long TR and short FUS pulse) was required to avoid heating that could lead to adverse bioeffects in the brain, the skull, and the scalp. In our study, we minimized heating by using the lowest FUS intensity and shortest pulse duration needed to generate detectable displacement and separating the FUS pulses in time with a TR of 1 second (overall duty cycle of 0.23%). The TR must be short enough to acquire a displacement map in a practical time frame. While tissue damage can occur with large temperature changes, it is possible that even small temperature changes in the brain can change neurological function temporally, which would be undesirable during neuromodulation studies [188]. In our study, heating in the brain was less than 0.1 °C in MR thermometry images derived from phase maps acquired during MR-ARFI, which is consistent with simulations. Optimization of the FUS sonication parameters were performed in a separate study [95].

4.6 Conclusion

This work has demonstrated that optical tracking-guided MR-ARFI is feasible beam localization method for targeting ultrasonic neuromodulation in living subjects. This method will directly benefit the field of MR-guided transcranial focused ultrasound, especially for therapies performed at nominally low intensities where potential bioeffects must be minimized (e.g., neuromodulation, drug delivery).

4.7 Appendix

4.7.1 Author contribution statement

Aspects of the work described in this Dissertation Chapter were included in a shared first authorship manuscript published in Scientific Reports [95]. S.J. designed and programmed the optically tracked MR-ARFI pulse sequence, with subsequent implementation and optimization of the sequence on ex vivo and in vivo platforms. M.P. designed and performed experiments related to safety testing, using in silico and ex vivo platforms to estimate and minimize potential bioeffects related to MR-ARFI prior to insonation in living animals.

Chapter 5

Rapid autofocusing of FUS acoustic pressure fields using MR-ARFI with spatially coded emissions

5.1 Abstract

Purpose:

To refocus transcranial MRgFUS acoustic pressure fields using MR-ARFI with a fewer number of required acquisitions.

Methods:

A multi-voxel MR-ARFI-based autofocusing algorithm that fits a set of pre-calibrated MR-ARFI-derived pressure field measurements to pressure fields acquired in situ using magnitude least-squares optimization is proposed. Acoustic simulations were used to derive a set of four amplitude- and phase-based aberration patterns to evaluate the multi-voxel refocusing algorithm to the canonical single voxel MR-ARFI-based refocusing algorithm. Ex vivo experiments with programmed aberrations that mimic those induced by the skull were performed using a preclinical transcranial MRgFUS system at 650 kHz. The single and multi-voxel refocusing algorithm were implemented to estimate the required aberration corrections needed to refocus the acoustic pressure field.

Results:

Multi-voxel refocusing provided better refocusing quality than the single voxel algorithm in every simulated target tested. The algorithm was tolerant to acceleration, up to when as few as N acquisitions were included in the least-squares fit vs. $4N$ acquisitions for the single voxel method. Ex vivo experiments showed that a set of N MR-ARFI images can be used to refocus the acoustic pressure field and recover displacement to within 98% of what was obtained free-field.

Conclusion:

Multi-voxel MR-ARFI-based refocusing enables rapid aberration correction of transcranial MRg-

FUS acoustic pressure fields.

5.2 Introduction

Magnetic resonance-guided focused ultrasound (MRgFUS) has many potential neurological applications [1]. Non-invasive ablative thalamotomy via high intensity FUS is an FDA-approved treatment option for patients with essential tremor [2] and tremor-dominant Parkinsonism [3]. Successful opening of the blood-brain barrier (BBB) [4] and neuromodulation of various brain circuitry [5–8] has been demonstrated in early human trials with low intensity FUS.

In transcranial MRgFUS applications, hemispherical transducers with large apertures relative to the size of the human skull are used to distribute energy over the skull surface and minimize ultrasound-induced heating [63, 64]. This design additionally minimizes the challenge of focusing ultrasound through the skull, since most of the incident waves will be orthogonal to the skull surface for targets close to the geometric center of the transducer. However, overcoming skull-induced aberrations of the acoustic pressure field remains a significant challenge [191]. Skull-induced aberrations are particularly severe when focusing off-center and/or close to the skull surface, which has fundamentally limited the treatment envelope of current transcranial MRgFUS targeting [16–18].

Commercial MRgFUS systems use phased array transducers with hundreds of elements to focus an acoustic pressure field through the skull [11, 12]. Each element is electronically driven with its own voltage waveform, with the goal of keeping each complex-valued acoustic pressure wave matched in amplitude and phase at the targeted focus location. In this way, aberrations of the acoustic pressure field caused by the skull can be compensated. The use of preoperative computed tomography (CT) scans to estimate skull acoustic properties is the standard aberration correction method [123]. Established CT-based refocusing methods use a software implementation of the wave equation in order to simulate transcranial ultrasound propagation through a CT-derived acoustic skull model. A set of element-wise amplitude and phase corrections that nominally maximize constructive wave interference at the target is produced for subsequent insonation in situ. Depending on the acoustic solver that is used, CT-based refocusing methods can take hours to produce a set of aberration corrections for a single target [126]. Systematic variations in the assigned medium properties can result in significant changes in the simulated results [148, 149]. In addition, a registration step is required to align the CT referential frame to MR, which could introduce additional errors if the transducer model is not properly aligned to the patient's skull in situ. CT scans also contain ionizing radiation, which is undesirable.

Recently, adaptive focusing algorithms via MR-acoustic radiation force imaging (MR-ARFI) have been proposed to refocus the acoustic pressure field in situ [91]. MR-ARFI pulse sequences map the incident tissue displacement (proportional to acoustic intensity) generated by the radiation force field from a propagating ultrasound wave [76]. Studies with ex vivo human skull fragments have shown superior corrections with MR-ARFI-based adaptive focusing, compared to the canonical hydrophone-based or CT-based refocusing methods [91, 93]. However, current approaches require $4N$ MR-ARFI scans to compute aberration corrections in situ (where N is the number of array elements). Reported scan times (2 hours/512 elements) are too long for practical in vivo use [142].

In this work, we describe and validate a rapid autofocusing method which can recover the complex-valued aberrations with many fewer MR-ARFI images. We fit a set of pre-calibrated pressure field maps to the acquired images in a "multi-voxel" magnitude least-squares approach. We propose a simulation workflow for deriving realistic skull-induced aberrations from publicly available datasets of an intact human skull for evaluating this and other aberration correction algorithms. We evaluated our multi-voxel MR-ARFI-based refocusing algorithm in simulations with a human skull in four different targets, with comparison to the canonical virtual time reversal and MR-based adaptive focusing algorithms in each case. Finally, we evaluated multi-voxel refocusing with a transcranial MRgFUS transducer in ex vivo phantom experiments with programmed aberrations that emulate those induced by the skull.

5.3 Methods

5.3.1 Theory

For a phased array transducer of N elements, the observed pressure at a spatial location $\vec{r}$ is the sum of N individual complex-valued acoustic pressure fields:

$$p(\vec{r}) = \sum_{n=1}^{N} p_n(\vec{r}) = \sum_{n=1}^{N} P_n(\vec{r})\, e^{j\phi_n(\vec{r})}, \tag{5.1}$$

where p_n is the complex pressure field radiated by element n with an incident pressure amplitude of P_n and phase of ϕ_n. The contribution of element n is attenuated in amplitude (A_n) and/or phase shifted (Φ_n) if an aberrator is present in the path of wave propagation:

$$\tilde{p}(\vec{r}) = \sum_{n=1}^{N} A_n\, p_n(\vec{r})\, e^{j\Phi_n} = \sum_{n=1}^{N} a_n\, p_n(\vec{r}), \tag{5.2}$$

where a_n represents the complex amplitude and phase aberration for element n. In most MRgFUS applications, acoustic waves interact with tissue via biophysical processes like heating and the radiation force, which are linked to the temporal average intensity:

$$\tilde{I}(\vec{r}) = \frac{\langle \tilde{p}^2 \rangle}{\rho c} = \frac{1}{2\rho c}\left| \sum_{n=1}^{N} a_n\, p_n(\vec{r}) \right|^2, \tag{5.3}$$

where ρ is the density, and c is the sound speed in the supporting medium. Unfortunately, relative phase differences between elements cannot be determined from a single magnitude-only intensity measurement. Energy-based methods like iterative optimization [43] ($\approx 20N$ emissions) or adaptive focusing [139] ($4N$ emissions) can be implemented to estimate amplitude and phase shifts between elements from a set of intensity measurements performed in situ. The iterative method sweeps through a set of $[-\pi, +\pi]$ candidate phase shifts between a reference element and every other element in the array to identify a phase correction that maximizes wave intensity at the acoustic focus. Focal optimization is performed using radiation force-derived intensity measurements, which have been validated with MR-ARFI for MR-based aberration correction [93]. Energy-based adaptive focusing is a more efficient aberration correction method that is based on the maximization of wave intensity for different spatially coded emissions. It exploits a physical-to-logical element basis transformation to improve focal SNR by defining linear combinations of the elements (e.g., according to the Hadamard matrix). In total, $4N$ spatially coded emissions are performed in situ to derive a set of amplitude and phase aberrations that can be inverted to refocus the acoustic pressure field. MR-based adaptive focusing only uses knowledge of the intensity at the acoustic focus via MR-ARFI (typically only a few image voxels) [141], so this method is henceforth referred to as the "single-voxel" method.

In this work, determining element-wise aberrations is cast as an optimization problem:

$$\hat{\mathbf{a}} = \underset{\mathbf{a}}{\operatorname{argmin}} \left\| \mathbf{y} - |\mathbf{Pa}| \right\|^2, \tag{5.4}$$

where $y_i = \tilde{p}(\vec{r_i})$, $\mathbf{P}_{i \times n} = p_n(\vec{r_i})$, and $\hat{\mathbf{a}} \approx \{a_n\}_{n=1}^{N}$. The overall refocusing procedure is summarized in Figure 5.1. The complex-valued pressure fields $\mathbf{P}$ are first measured for a given transducer and tissue type. This step is performed without an aberrator present ("free-field") either in simulations or ex vivo experiments via iterative optimization or adaptive focusing. Then, the aberrated pressure field $\tilde{I}(\vec{r})$ is measured in situ. The square root of the intensity measurement is used in the fit since $\tilde{I}(\vec{r}) \approx |\tilde{p}(\vec{r})|^2$. The estimated aberrations $\hat{\mathbf{a}}$ are recovered by solving the problem in Eqn 5.4 with magnitude least squares optimization:

```
$\hat{\mathbf{y}} \leftarrow [\sqrt{|y_1|} \ldots \sqrt{|y_{N_s}|}]^T$
repeat
    $\hat{\mathbf{a}} = (\mathbf{P}'\mathbf{P})^{-1}\mathbf{P}'\hat{\mathbf{y}}$                    (5.5)
    $\hat{\mathbf{y}} = [\sqrt{|y_1|}e^{j\angle\{\mathbf{P}\hat{\mathbf{a}}\}_1} \ldots \sqrt{|y_{N_s}|}e^{j\angle\{\mathbf{P}\hat{\mathbf{a}}\}_{N_s}}]^T$
until Stop criterion met
```

The set of correcting amplitudes and phases $\hat{\mathbf{a}}^{-1}$ are applied to each element to refocus the acoustic pressure field. This method benefits from beam illuminations across the entire pressure field since aberrations are estimated from pressure measurements in multiple voxels (N_s) jointly, and is henceforth referred to as the "multi-voxel" method.

5.3.2 Deriving skull-induced aberrations from simulations

Computational modeling of transcranial MRgFUS was performed in order to derive a set of phase aberrations that would closely simulate ultrasound propagation in the human skull. Simulations were performed using the k-Wave Toolbox in MATLAB (The Mathworks, Natick, MA), which is a full-wave acoustic solver that is widely used to model transcranial ultrasound propagation [129, 130]. The acoustic models used in this study were constructed from publicly available image

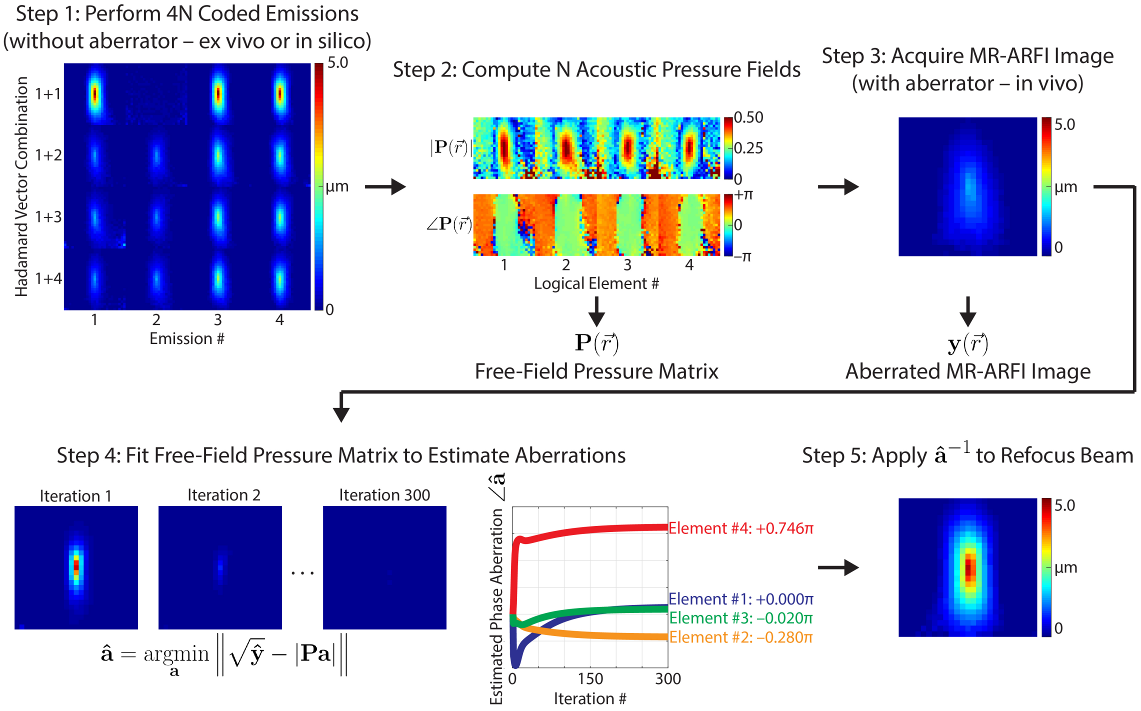

Figure 5.1: The multi-voxel refocusing algorithm. The multi-voxel refocusing algorithm fits a set of pre-calibrated pressure field maps to the aberrated MR-ARFI image acquired in vivo. It uses magnitude least-squares optimization to derive a set of aberration corrections that can be inverted to refocus the acoustic pressure field.

datasets from the Visible Human Project (VHP), which contain whole-body CT and MR images of human cadavers [192]. Studies have used these datasets to establish acoustic modeling methods [193].

Head images from one adult female cadaver were used for all simulations. T1-weighted brain images (0.86 × 0.86 × 4.00 mm voxel spacing, 256 × 256 × 33 matrix size, 17 ms/600 ms TE/TR) were skull-stripped followed by affine registration to a standardized space using the MNI152 template in FSL [194]. Images were upsampled to 0.50 mm^3 voxel spacing prior to registration. We defined four simulation targets with relevant brain circuitry for transcranial MRgFUS therapy: the anterior cingulate cortex (ACC) and posterior cingulate cortex (PCC) (two deep brain targets), and the left precentral gyrus (L PreCG) and postcentral gyrus (L PoCG) (two superficial targets) [195]. The cingulate gyrus was chosen in lieu of subcortical structures due to the focal length of the transducer used for experiments. Cortical masks were derived from the Harvard-Oxford Cortical Atlas for automated probabilistic segmentation of the VHP brain volume within MNI space [196]. The masks were projected into MR space using the inverse transform of the affine registration computed earlier. The centroid voxel of each volumetric mask was chosen as the target location for subsequent simulations.

Acoustic parameters were derived from CT data following standard methods [126, 193]. The skull was extracted using a threshold of 450 Hounsfield units (HU) and remaining tissue in the simulation grid was assumed to be homogeneous. Spatial maps of skull acoustic properties were computed from tissue porosity (Φ), which decreases with HU:

$$\begin{aligned} \Phi(\mathrm{HU}) &= 1 - \frac{\mathrm{HU}}{1000} \\ \rho(\Phi) &= \rho_{\mathrm{skull}} - (\rho_{\mathrm{skull}} - \rho_{\mathrm{water}}) \times \Phi \\ c(\Phi) &= c_{\mathrm{skull}} - (c_{\mathrm{skull}} - c_{\mathrm{water}}) \times \Phi \\ \alpha_{\mathrm{skull}}(\Phi) &= \alpha_{\mathrm{skull\,min}} + (\alpha_{\mathrm{skull\,max}} - \alpha_{\mathrm{skull\,min}}) \times \Phi^{\beta}, \end{aligned} \tag{5.6}$$

where ρ is the voxel-wise density (ρ_{water} = 1000 and ρ_{skull} = 2100 kg/m^3), c is the sound speed (c_{water} = 1500 and c_{skull} = 2900 m/s), α_{skull} is the absorption in the skull ($\alpha_{\mathrm{skull\,min}}$ = 1.33 and $\alpha_{\mathrm{skull\,max}}$ = 53.33 dB/cm/MHz), and β is a constant equal to 0.5 [193]. These equations assume a linear relationship between porosity (filled with water) and Hounsfield units, so Φ is close to 0 in most soft tissues and 1 in bone.

A 128-element phased array transcranial MRgFUS transducer (Image Guided Therapy, Bordeaux, FR) customized for ultrasonic neuromodulation in non-human primates was modeled in k-Wave and used for subsequent phantom experiments [197]. The transducer has a focal length of 7.2 cm, an opening diameter of 10.3 cm (f/0.7), and a center frequency of 650 kHz. Sonications were performed for 10 cycles (15.38 μs, dt = 50 ns or 30.77 points per period). A spatial discretization of 0.5 mm^3 was used, which resulted in 4.56 points per wavelength in tissue and 9.54 in bone. These parameters were chosen to balance computational burden with numerical accuracy [130]. The grid size was $480 \times 480 \times 270$ voxels and 1955 time steps (97.75 μs), which took $\approx$ 2.9 min per simulation with GPU acceleration (NVIDIA GeForce RTX 2080 Ti, Turing architecture). Simulations were performed on the Advanced Computing Center for Research and Education HPC Cluster (Vanderbilt University, Nashville, TN) on GPU-dedicated compute nodes.

To obtain the voxel locations of the four simulation targets (ACC, PCC, L PreCG, L PoCG) in CT space, the CT brain images (0.49 × 0.49 × 1.00 mm voxel spacing, 512 × 512 × 209 matrix size, 120 kVp, 170 mAs) were upsampled to 0.5 mm^3 voxels and registered to MR space in 3DSlicer using SlicerElastix [198]. The targeted location within each volumetric mask was the centroid voxel (registered from MNI to MR space using the workflow described earlier). These voxel locations were then projected into CT space using the inverse transform computed in this step. Simulations were performed in native CT space to preserve the highest achievable spatial resolution in the skull. The transducer was translated in the simulation domain to be coaxial with the target and rotated so that the skull was approximately tangential to the incident waves [68].

The propagation of a 10-cycle wavefront emitted from an acoustic source placed at the target location was simulated in k-Wave. The distorted wavefront was numerically recorded at the element locations after propagation through the skull. Differences in amplitude and phase between the received signals represent the element-wise complex-valued aberrations induced by the skull [119]. This procedure is exploited in virtual time reversal [126], in which the received signals are time-reversed and re-emitted to produce constructive wave interference back at the acoustic source. Here, the signals were recorded for each of the targeted locations to derive a set of four unique phase aberration patterns and used as input for subsequent experiments. Relative phase differences between elements were extracted in the frequency domain following FFT of the time-resolved data. This simulation workflow can be replicated with code soon to be available on our website (https://bitbucket.org/wgrissom).

5.3.3 Refocusing experiments in simulations

Three refocusing methods for transcranial MRgFUS aberration correction were evaluated in simulations: virtual time reversal, the single-voxel method, and the multi-voxel method. Virtual time reversal is the standard aberration correction method [124]. The derived phase aberration patterns were programmatically conjugated to refocus the acoustic pressure field in situ. Waves received first are emitted last, and vice versa. The peak pressure was computed after refocusing to evaluate the effectiveness of the aberration correction algorithm for each target.

The single voxel method was simulated using $4N$ spatially coded emissions [141]:

$$\begin{aligned} \mathbf{s}_i^a &= \frac{1}{2}(\mathbf{h}_1 + \mathbf{h}_i) & \mathbf{s}_i^c &= \frac{\sqrt{2}}{2}(\mathbf{h}_1 + j\mathbf{h}_i) \\ \mathbf{s}_i^b &= \frac{1}{2}(\mathbf{h}_1 - \mathbf{h}_i) & \mathbf{s}_i^d &= \frac{\sqrt{2}}{2}(\mathbf{h}_1 - j\mathbf{h}_i), \end{aligned} \tag{5.7}$$

where $\mathbf{H} = [\mathbf{h}_1 \ldots \mathbf{h}_N]$ is a set of independent emission column vectors that define the transmit functions for the ith logical element. In practice, $\mathbf{H}$ is given by the Hadamard matrix so that every emission transmits the full power capability of the array (i.e., $|\mathbf{s}_i|$ is always 1 for at least half of the elements). The complex-valued pressure fields were computed through intact skull in a 1 cm^3 mean ROI at the focus (20 voxels) according to [141] following decomposition of the Hadamard-coded transmit functions. In total, $4 \times 128 = 512$ simulations were performed to estimate phase corrections for one target. Spatial maps of intensity were computed by taking the mean square of the time-resolved pressure in each voxel in order to simulate MR-ARFI-derived measurements of temporal average intensity.

The proposed multi-voxel method was implemented in simulations by first computing the free-field complex-valued pressure fields ($\mathbf{P}$ in Eqn 5.4; 512 simulations per target). This was performed using the same procedure for the single-voxel method, but without the skull in the simulation grid. Then, the pressure field was simulated with the aberrator ($\mathbf{y}$) to estimate the skull-induced aberrations ($\hat{\mathbf{a}}$) with magnitude least squares optimization. In this experiment, the aberrated pressure field measurements used for fitting were those already acquired for the single voxel method, which were performed through intact skull via spatially coded intensity measurements. Prior to fitting, $\mathbf{P}$ was programmatically shifted in phase by the same phase shift used to generate each coded emission so that we could jointly estimate aberrations from a large number of voxels (20 voxels $\times$ 512 coded emissions = 10240 voxels). No additional calibrations were required. We evaluated the performance of the multi-voxel method using fewer simulated intensity measurements in the least-squares fit. We first estimated aberrations using all of the spatially coded emissions ($4N$ or 512 images). Then, we kept the emissions corresponding to the first $2N$ (256 images), N (128 images), $N/2$ (64 images), and $N/4$ (32 images) column vectors of the Hadamard matrix, and evaluated the effectiveness of the aberration corrections for each target.

5.3.4 Refocusing experiments in phantoms

The previously described 128-element phased array transducer was used to sonicate a human brain tissue-mimicking phantom (0.5% agar/4% graphite) in a water tank. Sonications were performed at 650 kHz for 10 ms (6500 cycles) at an acoustic power generating a free-field peak negative pressure of 4.8 MPa (MI = 5.95). Displacement images were acquired using a spin echo 2D MR-ARFI sequence implemented on a 7 Tesla scanner (Philips Achieva, Philips Healthcare, Best, NL) [95], with parameters: FOV/matrix/voxel size 120x120x4 mm^3/60x60x1/2x2x4 mm^3; TE/TR 29/500 ms; 18° flip angle. A volume head coil was used for transmit/receive (Nova, Nova Medical Inc, Wilmington, USA). Repeated unipolar MEGs were used for ARFI encoding, with gradient duration/strength 10 ms/40 mT/m. The second MEG was synchronized with an ultrasound emission using TTL outputs to trigger the transducer. Displacement images were reconstructed by complex subtraction of four phase images with opposite MEG polarities and with FUS turned on or off. One displacement image took 2.25 minutes to acquire and required 120 sonications. Two dummy displacement images were acquired afterward, resulting in a duty cycle of 0.89%. Images were reconstructed offline in MATLAB 2019a (MathWorks, Natick, MA).

The phase aberration patterns derived in simulations were used to evaluate the single voxel method and the multi-voxel method with MR-ARFI. We compared refocusing quality in both methods using the aberration pattern derived from one of the deep brain targets (PCC). Transducer elements were grouped into 8 logical elements (16 physical elements per logical element) using same-size k-means clustering of the phase aberrations [199]. This paradigm was chosen to reduce problem complexity while generating a set of logical elements that when driven together would closely emulate the skull. The mean phase aberration across an individual logical element grouping (computed in simulations) was programmatically added to each physical element prior to transmission. We demonstrate the effectiveness of this dimensionality reduction technique in a separate simulation study.

The single voxel method was implemented to recover the programmed aberrations using 4 spatially coded emissions per logical element (8 logical elements × 4 MR-ARFI acquisitions per element = 32 MR-ARFI acquisitions or 72.0 min scan time). We used the displacement measured in a 20 voxel mean ROI at the acoustic focus to estimate phase corrections. For multi-voxel-based refocusing, the complex-valued pressure fields generated by each logical element were first computed using the single-voxel method but without programmed aberrations (32 MR-ARFI acquisitions). The aberrated pressure field measurements used for fitting were those already acquired for the single voxel method (like in the simulation experiment), so no additional acquisitions were performed. We evaluated the performance of the multi-voxel method using fewer aberrated MR-ARFI images in the least-squares fit. We first estimated aberrations using all of the spatially coded emissions (4*N* or 32 images). Then, we identified the "best set" of *N* or 8 candidate images by iteratively reducing the number of aberrated images that went into the fit by eliminating the images that produced aberration corrections with the worst RMSE against what was programmed. We attempted to refocus the acoustic pressure field using the phase corrections computed by the single-voxel method and the multi-voxel method.

5.4 Results

5.4.1 Simulation experiments

Figure 5.2 shows volumetric visualizations of the MR- and CT-based human brain volumes from the Visible Human Project following atlas-based segmentation in FSL. The ACC (blue), PCC (cyan), L PrCG (red), and L PoCG (yellow) were automatically segmented using this method. The segmented volumes were registered to CT space using SlicerElastix for subsequent simulations in k-Wave. The results of that registration are shown as a volume rendering in the top right portion of the figure, and qualitatively indicate good registration between the two image volumes. The simulation grids for each of the targeted locations are shown in Figure 5.3 (left), where the estimated amplitude and phase aberrations were computed following virtual time reversal (shown on the right). Significant spatial heterogeneities in the aberrations are observed, both within and between the four different targeted locations.

Figure 5.4 shows simulated RMS pressure maps and beam profile plots before and after refocusing the beam with virtual time reversal. In every target, virtual time reversal significantly increased the peak pressure through intact skull (ACC: 1.27 to 1.83 MPa; PCC: 1.18 to 2.28 MPa; L PrCG: 0.45 to 1.05 MPa; L PoCG: 0.67 to 1.23 MPa). In addition, no targeting errors were observed following refocusing when compared to the location of the free-field beam. This was an especially significant improvement in targets like the ACC, which was displaced by 7.5 mm (15 voxels) without any aberration correction applied. Figure 5.5 shows simulated RMS pressure maps after refocusing the beam with 8 logical elements derived from same-size k-means clustering of the phase aberrations. These results indicate that as few as $N/16$ aberration corrections can be estimated and applied to refocus the acoustic pressure field with comparable refocusing quality to refocusing with all of the array elements individually.

Figure 5.6 shows the estimated element-wise amplitude and phase aberrations following single and multi-voxel MR-ARFI-based refocusing in simulations through intact skull. The magnitude error of the complex-valued aberrations is shown in Figure 5.7 and was computed as the deviation from the aberration estimates with virtual time reversal. In every target, both refocusing algorithms estimated aberrations that closely matched what was derived with virtual time reversal, except in the PCC, where the single voxel method was unable to reliably estimate the amplitude aberrations. The RMSE of the estimates is plotted in Figure 5.8 as a bar plot for all of the targeted locations. The multi-voxel method performed as well as the single-voxel method when as few as N simulated acquisitions were included in the least-squares fit. The refocused RMS pressure maps are shown in Figure 5.9, and the beam profiles are shown in Figure 5.10. Both the single and the multi-voxel method successfully refocused the acoustic pressure field in every target tested. The single voxel method refocused the peak pressure to within 97.4% (L PrCG) and 96.6% (L PoCG) in the superficial brain targets compared to what was refocused with virtual time reversal, but only 87.0% (ACC) and 78.4% (PCC) in the deep brain targets. These results are reflected in the error plots shown earlier (Figure 5.7), where the amplitude aberrations were not reliably estimated by the single voxel method in these targets. Conversely, the multi-voxel method refocused the peak pressure better than the single voxel method in every target up to when N acquisitions were used in the least-squares fit. When as few as $N/4$ (32 images) were included in the fit, the algorithm still performed better than when no refocusing was used in every target.

5.4.2 Phantom experiments

Figure 5.11 show representative MR-ARFI displacement images acquired using our transcranial MRgFUS transducer before and after programmed aberrations were applied. The programmed

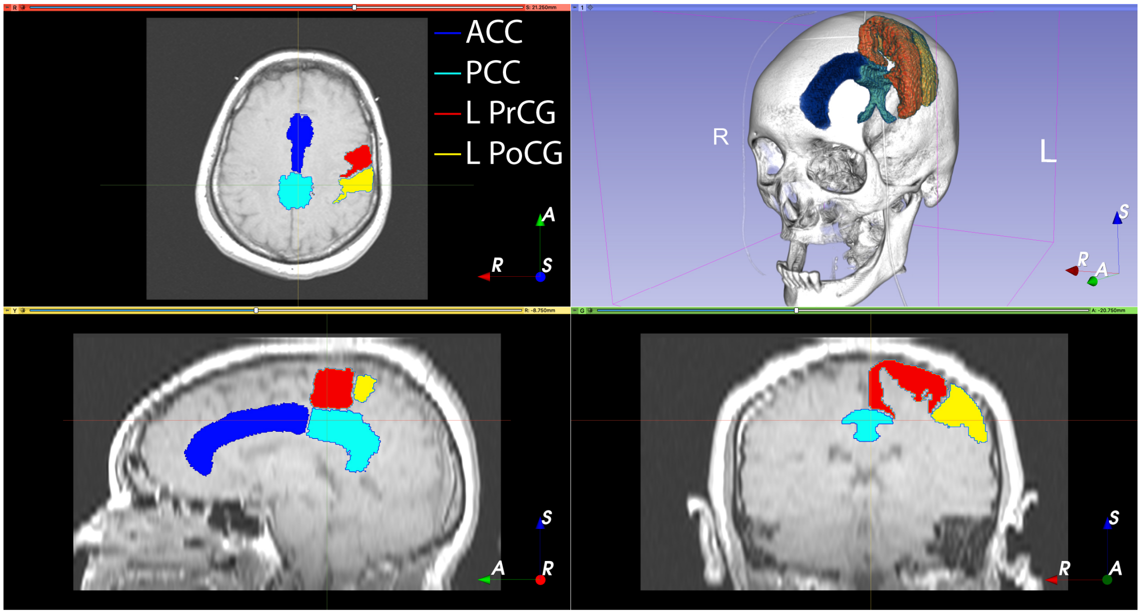

Figure 5.2: Targeted brain volumes from the Visible Human Project. Publicly available MR- and CT-based image datasets were downloaded from the Visible Human Project and displayed for volume visualization in 3DSlicer. Atlas-based segmentation was performed in FSL to automatically identify segmented regions of the anterior cingulate cortex (ACC), posterior cingulate cortex (PCC), left precentral gyrus (L PrCG), and left postcentral gyros (L PoCG) for subsequent acoustic simulations with the k-Wave Toolbox in MATLAB. These brain regions were registered from MR to CT space using the SlicerElastix module in 3DSlicer. They are shown as a volume rendering in the top right portion of the figure.

skull reduced the measured peak displacement in the tissue-mimicking phantom by 50.6%. Figure 5.12 compares phase aberration estimates obtained by the canonical single-voxel MR-ARFI-based refocusing method and our proposed multi-voxel method. When all $4N$ or 32 images were included in the least-squares fit to the pre-calibrated free-field pressure field measurements, the multi-voxel method recovered the programmed aberrations with similar RMSE to the single-voxel method. We were able to identify a set of N or 8 images that when included in the least-squares fit, these images actually provided a better estimate of the programmed aberrations than either the single voxel method or the multi-voxel method with all $4N$ candidate images from the spatially coded emissions included in the least-squares fit. This represents a 75% reduction in the number of required acquisitions for MR-ARFI-based refocusing. The computed aberration corrections were applied to refocus the programmed aberrations, and the resulting beam maps and profiles are shown in Figure 5.13. Both the single voxel method and the multi-voxel method with $4N$ fitted images refocused the peak displacement to within 70% of what was obtained in the free-field beam map. However, multi-voxel-based refocusing with N images provided the best refocusing effectiveness,

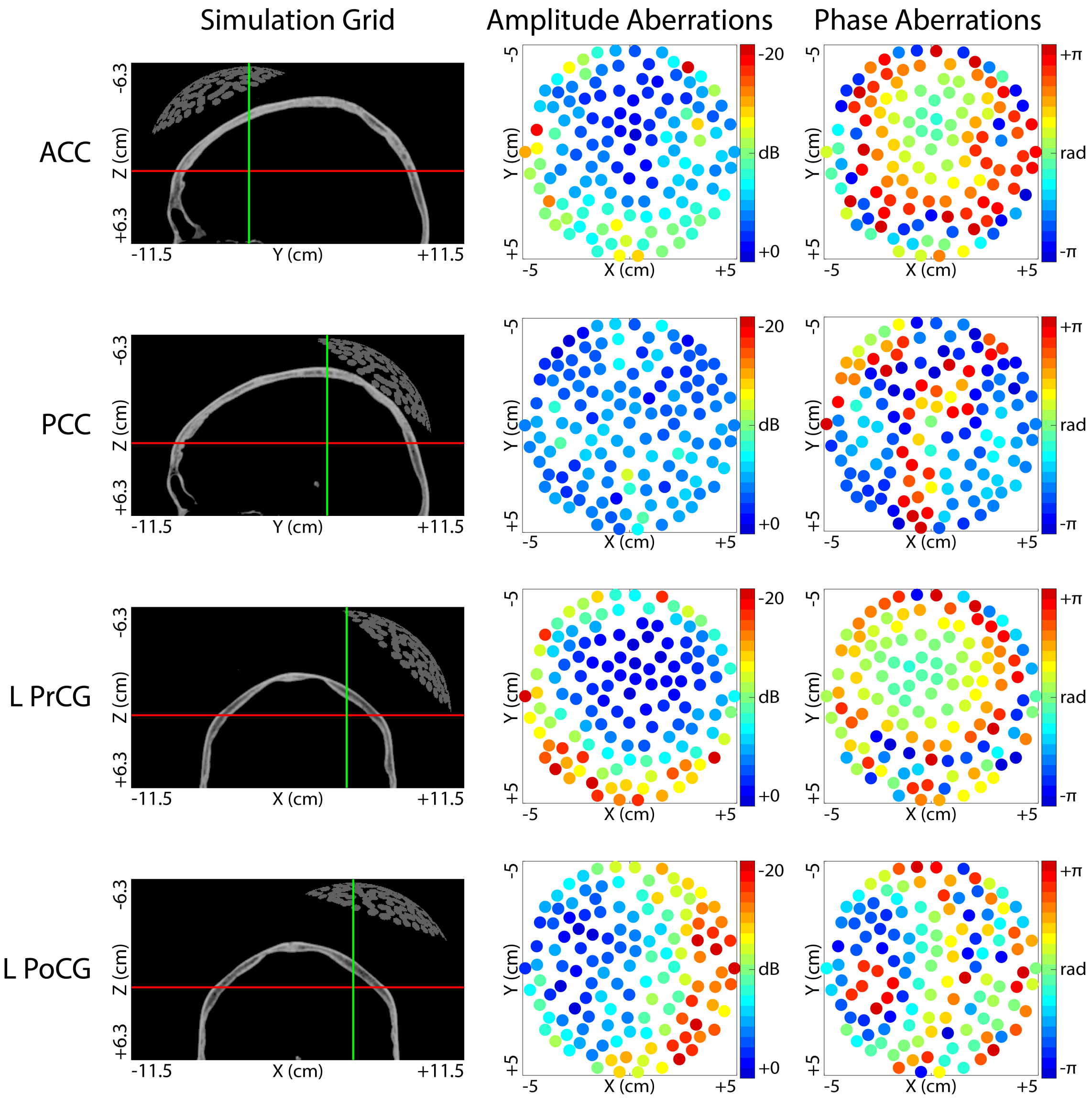

Figure 5.3: Estimated amplitude and phase aberrations in four targeted brain regions. Following registration of MR and CT data sets in 3DSlicer, the targeted locations of four brain regions (ACC, PCC, L PrCG, and L PoCG) were identified in CT space and used for acoustic simulations via virtual time reversal to estimate the set of amplitude and phase aberrations observed when targeting in each respective brain region. The amplitude aberration patterns are scaled such that the element experiencing the least amplitude aberration was assigned a relative amplitude of 1 (or 0 dB). The phase aberration patterns are shown relative to the central element of the transducer, which was assigned a relative phase aberration of 0 rad.

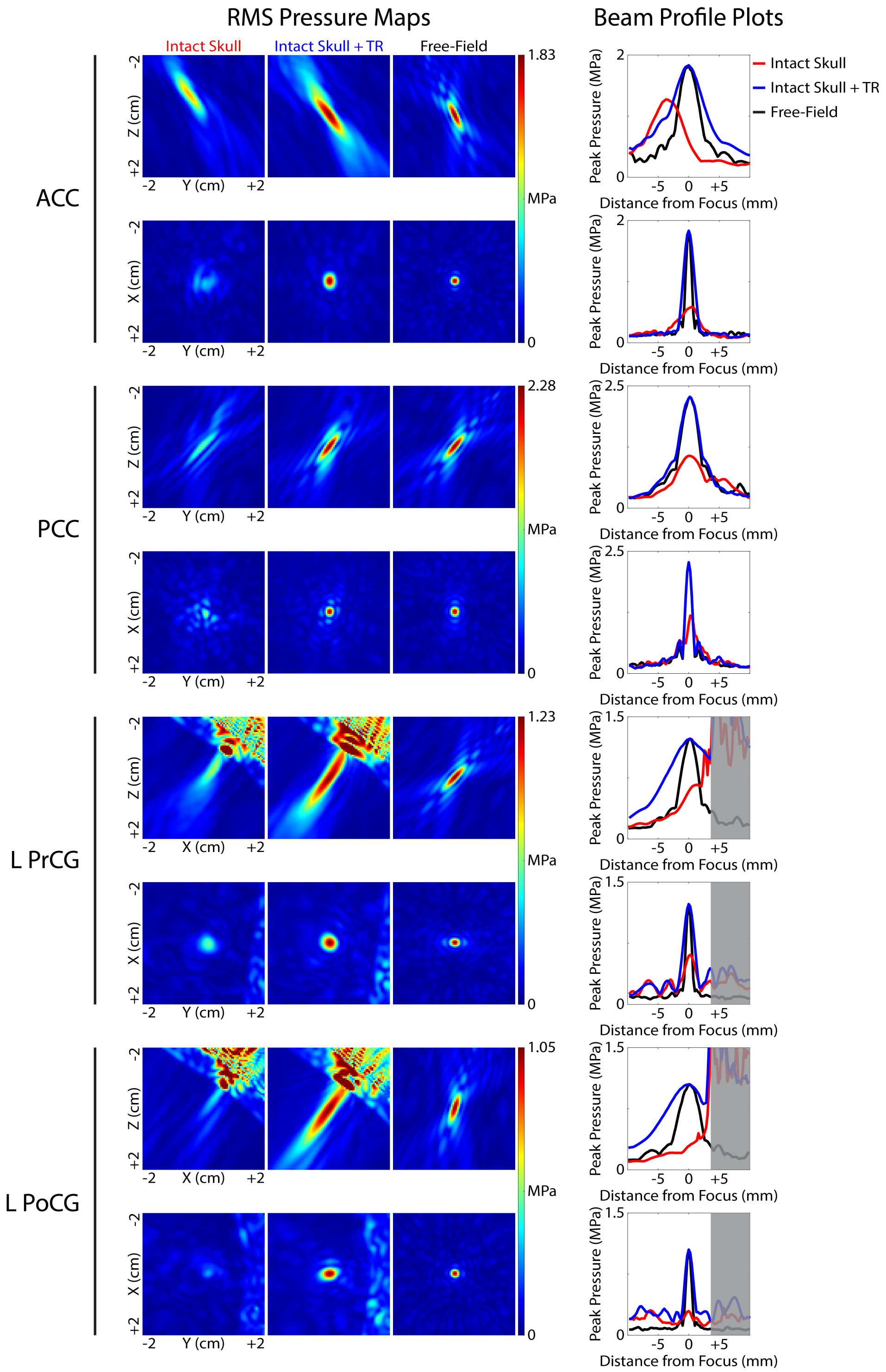

Figure 5.4: RMS pressure maps and beam profile plots before and after virtual time reversal. Virtual time reversal was applied in the four simulated target regions to refocus the acoustic pressure field. The aberration correction procedure refocused the peak pressure in every single case, with no targeting error relative to the free-field beam. The free-field beam maps were scaled relative to the peak pressure of the refocused beam and are intended to show the beam shape relative to the aberrated and refocused beams.

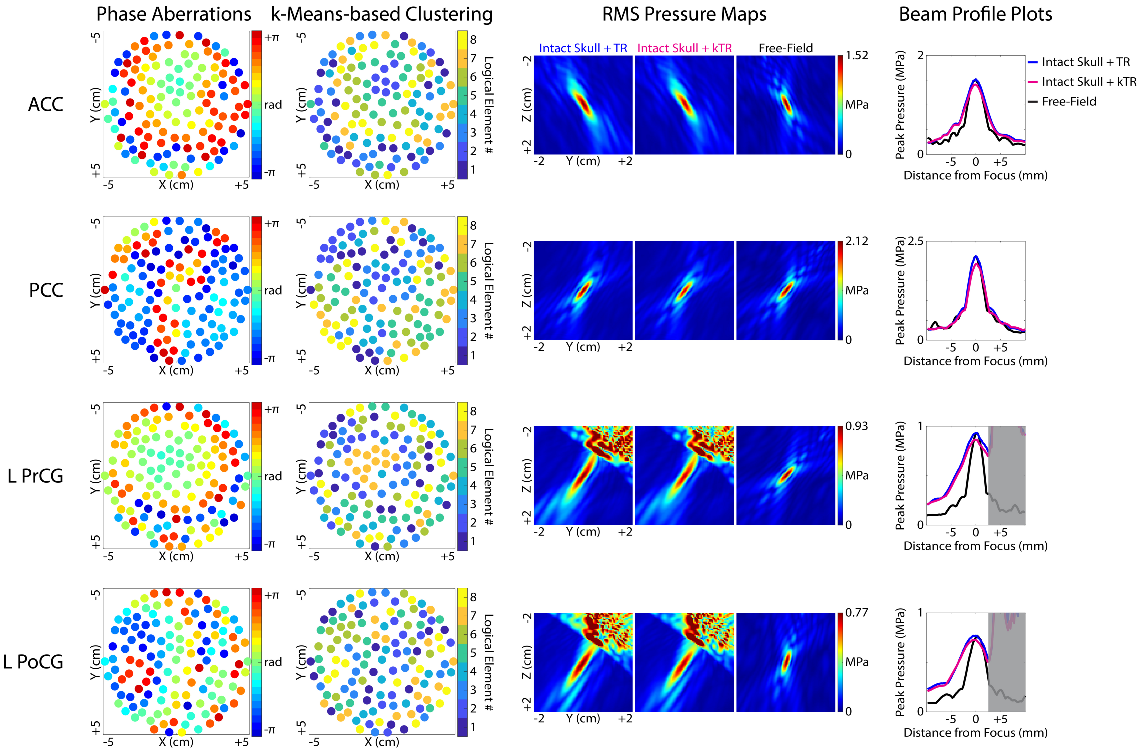

Figure 5.5: RMS pressure maps and beam profile plots with same-size k-means clustering. K-means clustering was applied to the estimated phase aberrations to produce a set of 8 logical elements that when driven together would still emulate the skull-induced aberration patterns estimated by the full array. Negligible differences were seen when refocusing with a fewer number of logical elements, which reduces problem complexity for aberration correction since a fewer number of elements would be required to refocus the acoustic pressure field.

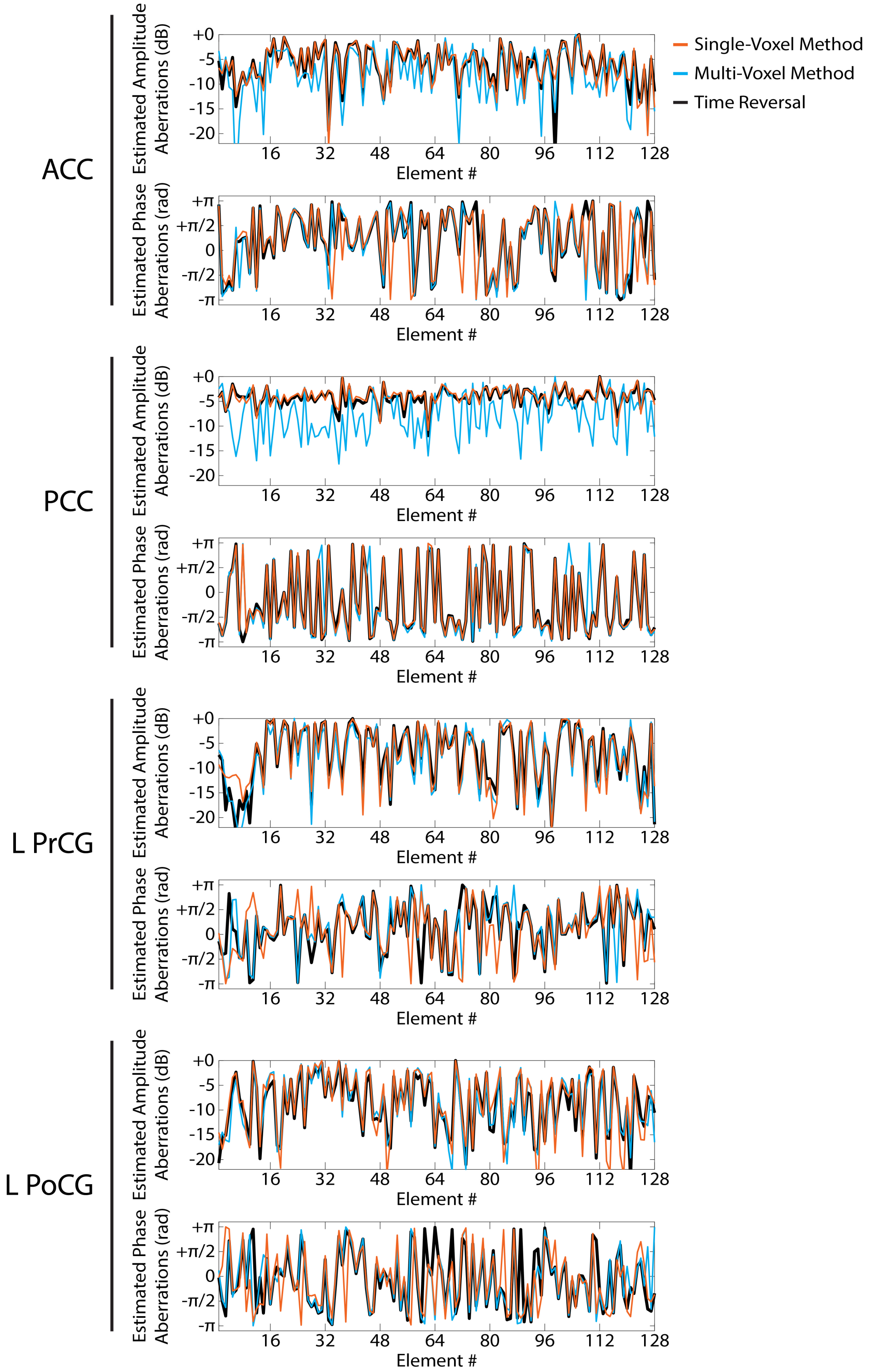

Figure 5.6: Estimated amplitude and phase aberrations with single and multi-voxel-based refocusing methods in simulations. The single and multi-voxel MR-ARFI-based refocusing methods were implemented in simulations to estimate aberrations in the four simulated targets. The estimated aberrations closely follow what was estimated with virtual time reversal.

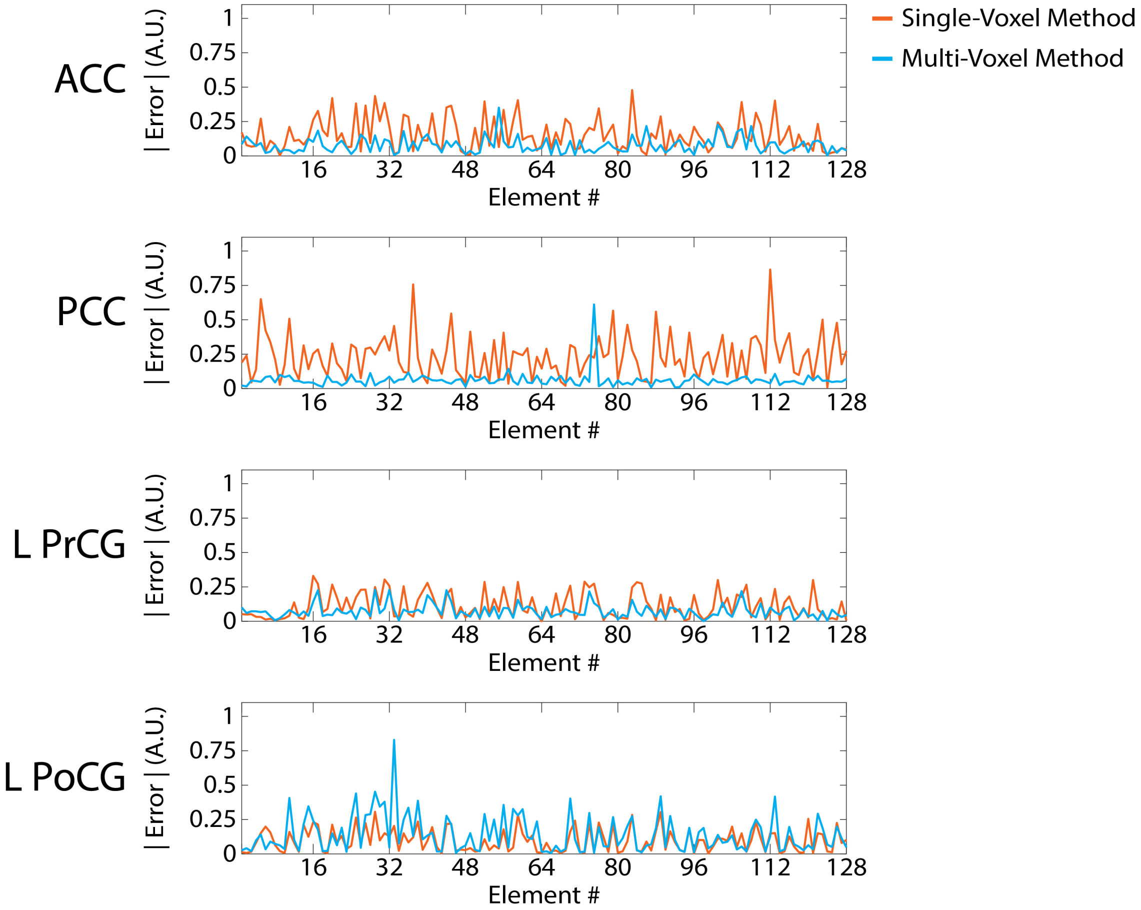

Figure 5.7: Magnitude error in estimated aberrations with single and multi-voxel-based refocusing methods in simulations. The error in the estimated aberrations computed with the single and multi-voxel MR-ARFI-based refocusing methods are shown relative to what was estimated with virtual time reversal.

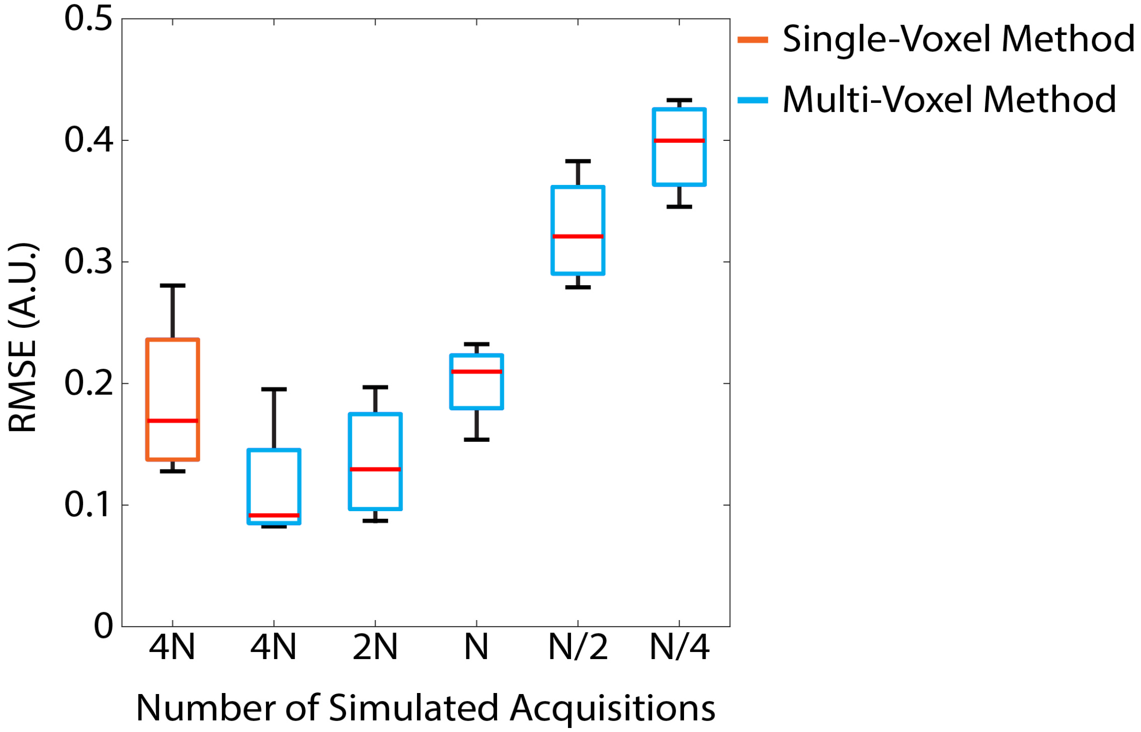

Figure 5.8: Magnitude error in estimated aberrations with single and multi-voxel-based refocusing methods in simulations (bar plot). The element-wise aberrations estimated with the single and multi-voxel MR-ARFI-based refocusing methods are shown relative to what was estimated with virtual time reversal as RMS error. Bar plots indicate the achievable RMS error across the entire range of the four different targets evaluated. In every case, the multi-voxel method refocused the acoustic pressure field with lower RMSE than the single voxel method. When a fewer number of aberrated images were included in the least-squares fit, the multi-voxel method provided comparable results to the single-voxel method up until *N* images were included in the least-squares fit.

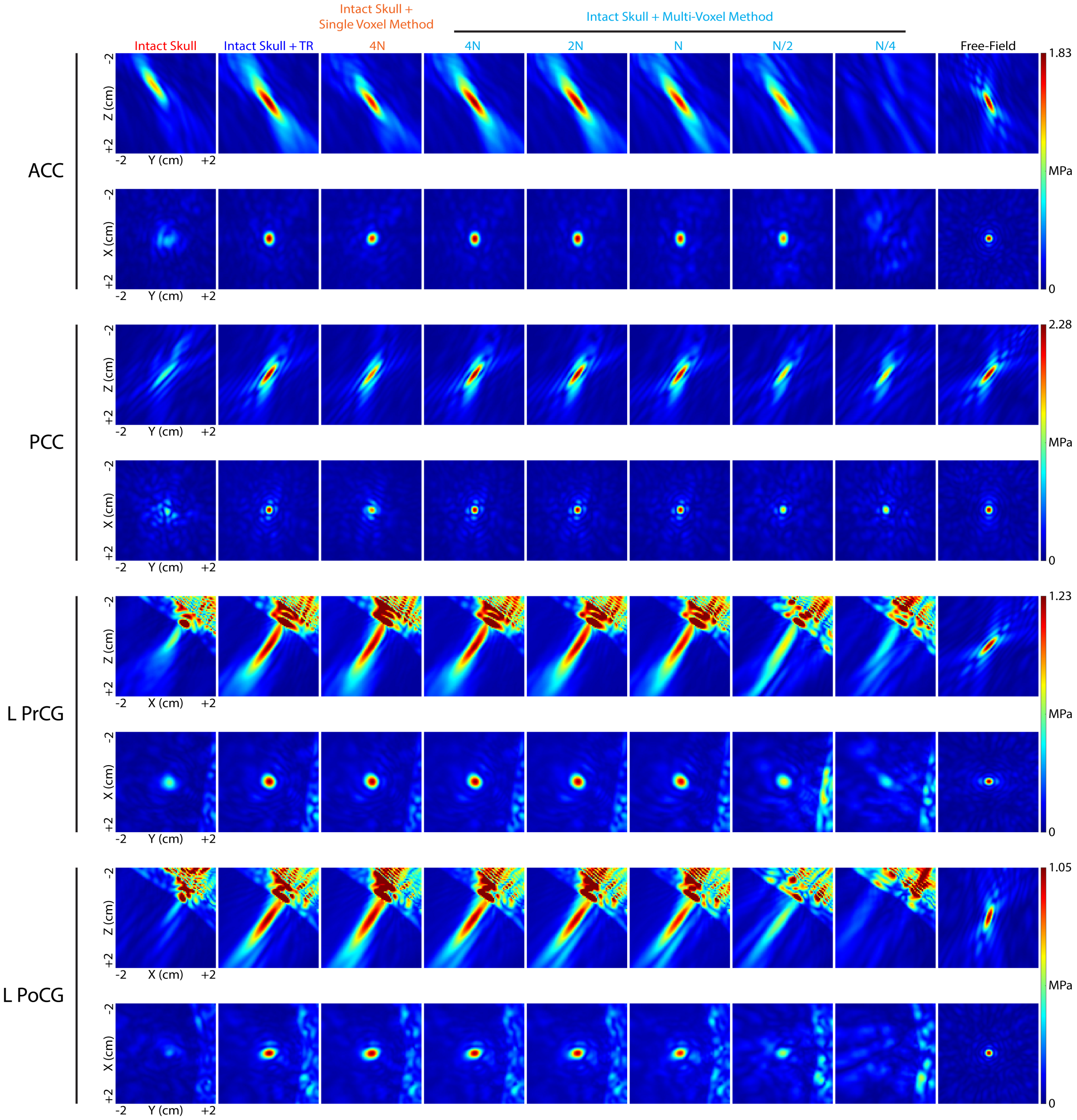

Figure 5.9: RMS pressure maps and beam profile plots before and after aberration correction. The effectiveness of virtual time reversal, the single voxel method, and the multi-voxel method for aberration correction in four simulated targets is shown in representative beam maps acquired at the focus location. All three correction algorithms successfully refocused the peak pressure better than when no aberration correction was applied through intact skull. The multi-voxel method performed better than the single voxel method up to when N images were included in the least-squares fit.

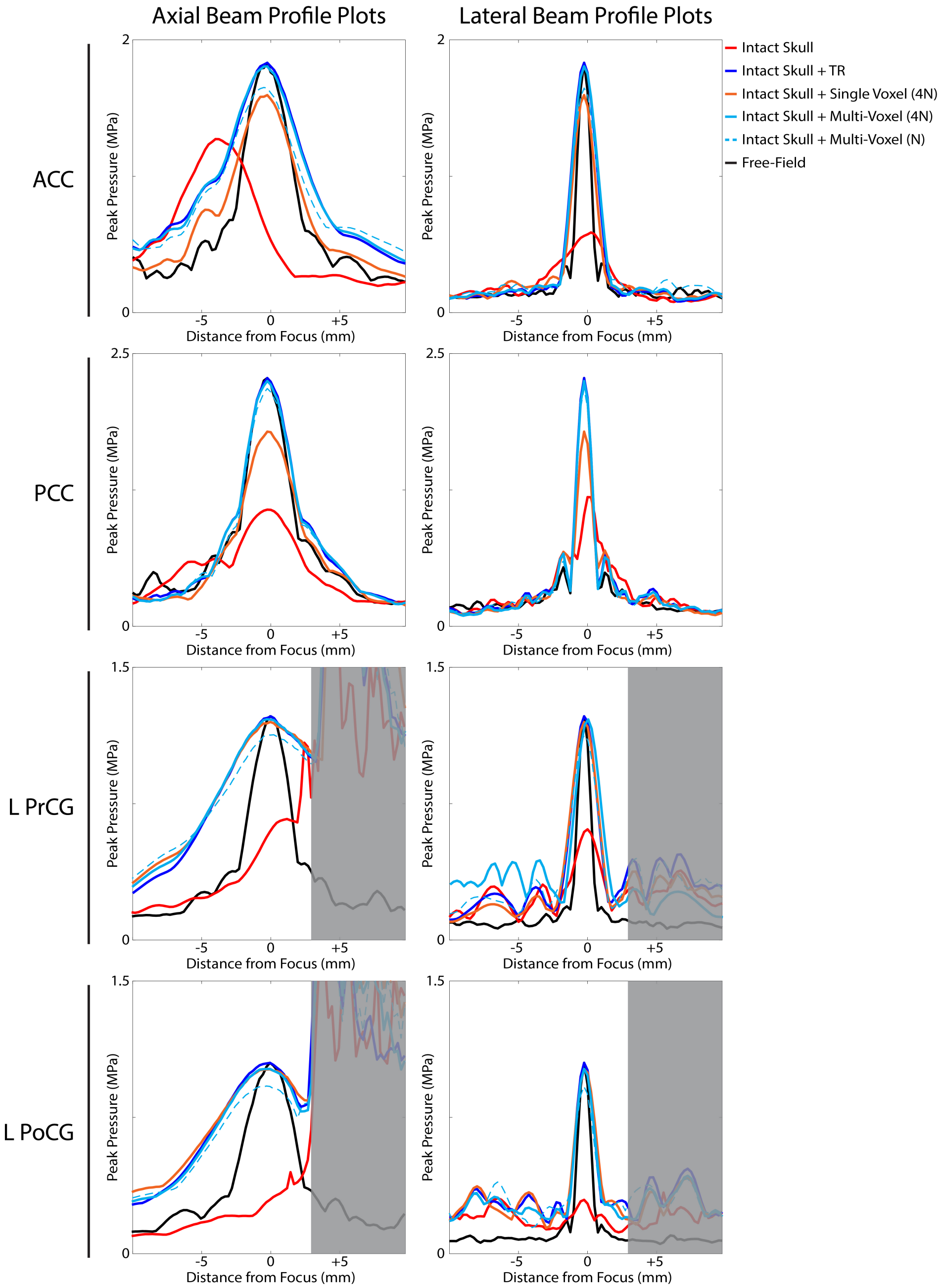

Figure 5.10: Beam profile plots before and after aberration correction. The effectiveness of virtual time reversal, the single voxel method, and the multi-voxel method for aberration correction in four simulated targets is shown in representative beam profile plots acquired at the focus location, corresponding to the beam maps in Figure 5.9.

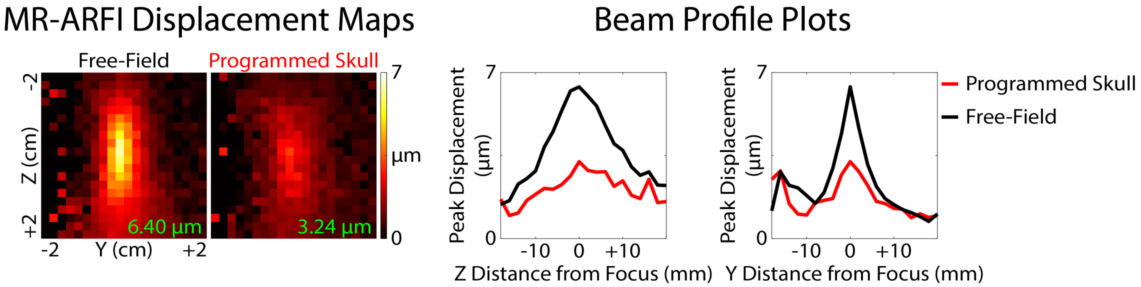

Figure 5.11: Representative MR-ARFI displacement images in an ex vivo phantom. MR-ARFI images were acquired using our transcranial MRgFUS system at 650 kHz using 10 ms sonications and a 2D spin echo MR-ARFI pulse sequence. A set of phase aberrations were programmatically applied to the transducer elements prior to transmission, which emulate skull-induced aberrations observed in the PCC (50.6% reduction in displacement).

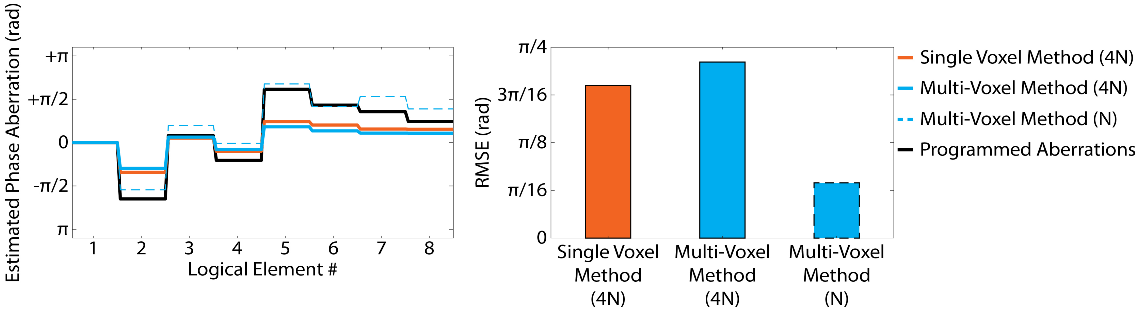

Figure 5.12: Estimating programmed aberrations with single and multi-voxel refocusing algorithms. The single and multi-voxel MR-ARFI-based refocusing algorithms were used to estimate aberrations from an acoustic pressure field programmatically aberrated in phase (black line). Both the single voxel (orange) and multi-voxel (cyan, solid) refocusing algorithms with 4*N* acquisitions (32 images) estimated the aberrations with similar RMSE compared to what was programmed. We identified a set of *N* aberrated acquisitions that estimated the programmed aberrations with even lower RMSE when the multi-voxel method was used.

which recovered 98.1% of the peak displacement.

5.5 Discussion

In this work, we provide preliminary evidence for the use of a multi-voxel algorithm for rapid aberration correction of transcranial MRgFUS acoustic pressure fields. We developed a simulation workflow for deriving skull-induced aberrations from an intact human skull and subsequently evaluating the effectiveness of MR-ARFI-based aberration correction algorithms in deep and superficial targeted brain regions. We evaluated the multi-voxel algorithm on simulated and ex vivo platforms of skull-induced aberrations, and showed that the algorithm can refocus the acoustic pressure field with as few as *N* MR-ARFI-based intensity measurements. This represents a 75% reduction in the number of acquisitions currently required for refocusing with MR-ARFI.

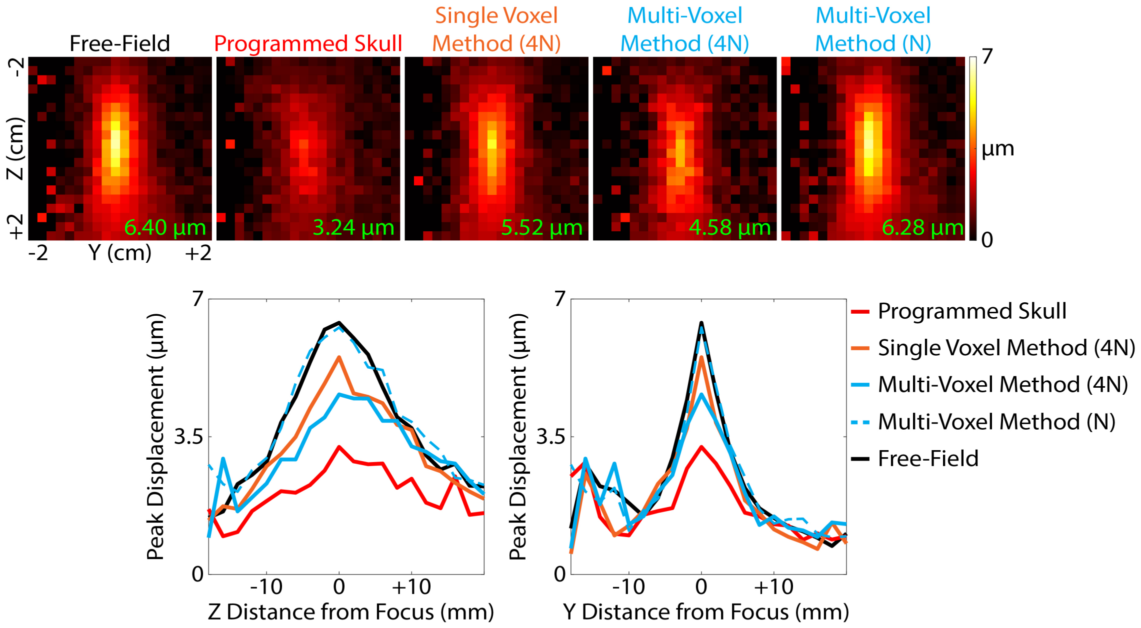

Figure 5.13: Refocusing acoustic pressure fields with single and multi-voxel refocusing. The estimated aberration corrections determined from the single and multi-voxel MR-ARFI-based refocusing algorithms were used to refocus the programmatically aberrated acoustic pressure field. Both the single and multi-voxel refocusing algorithms with $4N$ acquisitions refocused the acoustic pressure field to within 70% of the peak displacement with what was obtained free-field. However, the multi-voxel refocusing algorithm with N acquisitions provided the best refocusing quality (98% recovery of peak displacement).

Through acoustic simulations, we derived sets of complex-valued amplitude and phase aberrations from four different targeted regions in the human brain (Figure 5.3). We observed significant spatial heterogeneities in the patterns of the aberrations that were estimated, which are qualitatively in agreement with a few studies that have published patterns estimated from other human skulls [93, 142]. Both amplitude- and phase-based aberrations are generally lower in magnitude near the center of the skull where incident waves are less likely to be reflected (ACC, L PrCG). However, this is not always the case, as in the PCC, which had a relatively flat amplitude aberration across the transducer face, but a sharp phase aberration close to the center of the skull. Similarly, the L PoCG exhibits a left-to-right gradient in the magnitude of the estimated aberrations. In all cases, each of the three aberration correction algorithms tested (virtual time reversal, single voxel method, multi-voxel method) were successfully able to refocus the acoustic pressure field better than when no aberration correction was applied. Interestingly, the single voxel method had better performance in the superficial brain targets than the deeper targets (Figure 5.9). In both deep targets, the single voxel method was unable to reliably estimate the amplitude aberrations (Figure 5.7). Since the single voxel method computes the complex-valued aberrations in a mean ROI near the acoustic focus, it is possible that the spatial variations in the amplitude aberrations induced by the skull were too high to be effectively encoded by this method. The multi-voxel method is relatively insensitive to these effects, since it attempts to estimate the best set of amplitude and phase aberrations that explain the aberrated pressure field measurements induced by the skull from a large number of voxels, not just in an ROI measurement near the focus. We showed that the multi-voxel method robustly estimated aberrations when as few as N images (corresponding to the first N column vectors of the Hadamard matrix) were included in the least-squares fit. We additionally showed in simulations that same-size k-means clustering can be used to compress the estimated aberrations to just $N/16$ logical elements (Figure 5.5), which reduced problem complexity when performing subsequent ex vivo experiments ex vivo with a programmed skull.

Our ex vivo experiments with MR-ARFI-derived intensity measurements showed that the multi-voxel algorithm can refocus the MRgFUS acoustic pressure field with as few as N MR-ARFI scans (Figures 5.12 and 5.13). In our analysis, we identified the "best set" of N candidate images by iteratively eliminating the acquisitions that did not significantly contribute to the least-squares fit. Interestingly, including fewer aberrated images in the least-squares fit provided better performance than when all $4N$ images were included. This suggests that some error in the model used may be present when determining the aberration corrections with a greater number of images. For example, non-linearities in the acoustic pressure field may propagate to the MR-ARFI-derived estimates of acoustic intensity, which is assumed to follow a linear relationship [76]. In addition, even when sonicating in a linear regime, non-linearities in the tissue elastic response are known to be present [200]. The methods described in the present study would in practice require a priori knowledge of the programmed aberrations prior to the refocusing procedure. Still, we show that a set of significantly fewer candidate images than is currently required can be used to estimate aberration corrections and refocus the acoustic pressure field with excellent refocusing quality (Figure 5.13). Future work with this technique will identify more systematic ways of choosing which aberrated images to include for the fitting procedure that are valid for a number of different aberration patterns.

Adaptive focusing with MR-ARFI offers several advantages for transcranial MRgFUS aberration correction. The standard aberration correction method uses a preoperative CT scan of the patient's skull to derive element-wise amplitude and phase corrections that refocus the acoustic pressure field through the skull. Eliminating the need for CT-based aberration correction would benefit treatment planning for several reasons. Both CT-based refocusing methods (ray-tracing, virtual time reversal) are parametric and require a priori knowledge of skull acoustic properties. Established methods use empirical assumptions of wave propagation that were largely derived from ex vivo human skull fragments [48, 123]. Studies have shown that the relationship between skull acoustic properties and CT-derived Hounsfield units is not straightforward, since it varies with photon energy and reconstruction method [147]. Comparisons between simulated and experimental treatment efficiencies have revealed the need for skull-specific acoustic models, which is limited by the availability of patient data to validate such models [50, 51, 53]. Depending on the acoustic solver that is used, CT-based refocusing can take hours to produce one set of amplitude and phase corrections per targeted focus location [126]. In addition, a registration step is required to align the CT referential frame to MR, which could introduce simulation errors if the transducer model is not properly aligned to the patient's skull in situ. Systematic variations in assigned medium properties result in significant changes in the simulated results [148, 149]. CT scans also contain ionizing radiation, which is undesirable in transcranial MRgFUS studies with healthy controls. Conversely, MR-guided focusing enables immediate feedback of focusing quality. It makes no assumptions of acoustic properties in the supporting medium, and thus can produce a set of amplitude and phase corrections for any aberrator configuration to refocus the acoustic pressure field in situ.

Ongoing work in this field is aimed at improving the efficiency of adaptive focusing, either by reducing acquisition times and/or the number of required intensity measurements to compute the complex-valued aberration corrections. The first demonstration of MR-ARFI-based refocusing in a clinical MRgFUS environment required 1536 Hadamard-coded emissions (384 elements × 4) and took 2 hours of acquisition time to refocus the acoustic pressure field [142]. Since then, Zernike polynomials have been proposed to replace the canonical Hadamard basis transformation. One study showed that the number of Zernike-derived emissions required to approximate a set of skull-induced aberrations represented a small fraction of the number of elements ($\approx 0.8N$). Unfortunately, the aberration corrections in that study were largely derived from simulations, so its performance in situ is unknown [143]. Another study showed that random calibration measurements could be fit in a least-squares sense to the complex-valued free-field pressure transmission matrix to further improve refocusing efficiency. Again, this study derived aberration corrections from simulated acquisitions of MR-ARFI, so its true benefit is unknown. Also, it did not recognize that displacement is proportional to temporal average intensity, which is a quantity that does not contain phase information [144]. Efficient adaptive focusing with MR-ARFI has been achieved with a rapid EPI pulse sequence acquisition. One study estimated aberration corrections from 64 groups of 4 elements (256 physical elements) in less than 10 minutes using an EPI pulse sequence optimized for MR-ARFI. However, it used a short TR of 44 ms to obtain a short acquisition time, which resulted in a high duty cycle (2.3%) and unacceptable heat deposition at the focus (4.86 °C) [145]. A hybrid MR-ARFI/simulation approach has also been proposed, but it requires a separate simulation step, and its benefit was minimal in the setting of skull-induced aberrations (< 0.1 rad improvement in phase) [146]. In the present study, we show that aberration corrections may be estimated from many fewer pressure field measurements in situ after fitting to pre-acquired complex-valued pressure fields via magnitude least squares optimization. This method benefits from beam illuminations across the entire pressure field since aberrations are estimated from pressure measurements in multiple voxels jointly (the "multi-voxel" method).

5.6 Conclusion

We proposed and validated a multi-voxel MR-ARFI-based aberration correction method that can refocus transcranial MRgFUS acoustic pressure fields with as few as N MR-ARFI scans. The method was evaluated in simulated and ex vivo models of human skull-induced aberrations and performed better than the canonical single voxel MR-ARFI-based refocusing method, which requires $4N$ MR-ARFI scans.

Chapter 6

Conclusion

6.1 Contributions of this work

Advancements in magnetic resonance imaging (MRI)-based targeting methods have been presented for guiding transcranial MR-guided focused ultrasound (MRgFUS) applications during high intensity ablation treatments via volumetric thermometry pulse sequences (3D SoS EPI; Chapter 3), and also during low intensity neuromodulatory treatments via MR-acoustic radiation force imaging (MR-ARFI) pulse sequences with optical tracking-based neuronavigation (Chapter 4). In addition, a rapid aberration correction method is described that uses pre-calibrated MR-ARFI-derived intensity measurements fit to a set of a few aberrated measurements acquired in situ via magnitude least squares optimization in order to focus ultrasound through the skull (Chapter 5). The methods described in this dissertation are generally applicable to any MRgFUS platform when concurrent MRI guidance is available during treatment.

6.2 Future work

6.2.1 Enabling in vivo aberration corrections with the multi-voxel algorithm

We have demonstrated that the multi-voxel algorithm can be used to refocus transcranial MRgFUS acoustic pressure fields with many fewer MR-ARFI-derived intensity measurements than are currently required. The algorithm benefits from a set of complex-valued pressure field calibrations that are pre-acquired from separate in silico or ex vivo experiments. We have already developed a workflow for deriving the complex-valued pressure field matrix in acoustic simulations with an actual human skull, and furthermore demonstrated a benefit when multi-voxel refocusing was used to refocus the pressure field compared to the canonical single voxel method. Future work with this algorithm will develop methods to use the pressure fields computed from an in silico implementation of the transducer with the aberrated images that are derived in vivo via MR-ARFI. Aberration corrections that use a hybrid simulation/MR-ARFI-based approach have already been proposed [146], though the existing technique uses an iterative strategy that continuously acquires MR-ARFI images until the simulations agree with what was acquired experimentally. The methods proposed here would use the simulated pressure fields to perform magnitude least-squares optimization with a single set of aberrated MR-ARFI images. The MR-ARFI-derived pressure fields are expected to be broader than what is computed in simulations, due to the viscoelastic properties of the tissue in response to an applied radiation force field; we observed this effect in the present study, where the beam width was much larger experimentally than what was computed in simulations. Future work will adapt methods that can better model the MR-ARFI-derived intensity measurements in simulations so that they agree with what is acquired experimentally [200].

6.2.2 Pressure field calibrations with multi-focus sonications

Phased array transducers enable flexible control of focusing for transcranial MRgFUS applications. For example, the acoustic focus can be steered from its geometric location, or multi-focus sonications can be generated in order to improve treatment efficiency and/or enhance specificity beyond what is capable with a single focus. We have already shown that the proposed multi-voxel MR-ARFI-based refocusing algorithm benefits from beam illuminations across the entire pressure field, since it uses magnitude least squares optimization over a large number of voxels to estimate aberration corrections. Future work with this algorithm will establish the efficacy of the algorithm when steered and/or multi-focus sonications are used to calibrate the pressure field.

6.2.3 Dimensionality reduction techniques for rapid pressure field calibrations

Dimensionality reduction is a classic machine learning task that can reduce problem complexity when working with high-dimensional data sets [201]. Since the number of elements in a typical transcranial MRgFUS transducer phased array design is in the hundreds to thousands (e.g., 1024 elements for the Insightec ExAblate Neuro), element-wise modeling of the transducer is not practical in a short time frame. We have shown that strategies like k-means clustering can be used to reduce the number of aberration corrections required to refocus the acoustic pressure field by a factor of $N/16$ with existing aberration correction methods. Future work with the proposed methods will investigate the efficacy of other dimensionality reduction techniques for determining the optimal set of logical elements that can represent the full array but with fewer driving functions.

REFERENCES

[1]Krishna V, Sammartino F, Rezai A. A review of the current therapies, challenges, and future directions of transcranial focused ultrasound technology. JAMA Neurology 2018;75:246.

[2]Elias WJ, Lipsman N, Ondo WG, Ghanouni P, Kim YG, Lee W, Schwartz M, Hynynen K, Lozano AM, Shah BB, et al. A randomized trial of focused ultrasound thalamotomy for essential tremor. N Engl J Med 2016;375:730–739.

[3]Bond AE, Shah BB, Huss DS, Dallapiazza RF, Warren A, Harrison MB, Sperling SA, Wang XQ, Gwinn R, Witt J, Ro S, Elias WJ. Safety and efficacy of focused ultrasound thalamotomy for patients with medication-refractory, tremor-dominant parkinson disease. JAMA Neurology 2017; 74:1412.

[4]Lipsman N, Meng Y, Bethune AJ, Huang Y, Lam B, Masellis M, Herrmann N, Heyn C, Aubert I, Boutet A, Smith GS, Hynynen K, Black SE. Blood–brain barrier opening in alzheimer's disease using MR-guided focused ultrasound. Nature Communications 2018;9.

[5]Hameroff S, Trakas M, Duffield C, Annabi E, Gerace MB, Boyle P, Lucas A, Amos Q, Buadu A, Badal JJ. Transcranial ultrasound (TUS) effects on mental states: A pilot study. Brain Stimulation 2013;6:409–415.

[6]Legon W, Sato TF, Opitz A, Mueller J, Barbour A, Williams A, Tyler WJ. Transcranial focused ultrasound modulates the activity of primary somatosensory cortex in humans. Nat Neurosci 2014;17:322–9.

[7]Mueller J, Legon W, Opitz A, Sato TF, Tyler WJ. Transcranial focused ultrasound modulates intrinsic and evoked EEG dynamics. Brain Stimulation 2014;7:900–908.

[8]Lee W, Kim H, Jung Y, Song IU, Chung YA, Yoo SS. Image-guided transcranial focused ultrasound stimulates human primary somatosensory cortex. Scientific Reports 2015;5.

[9]Lynn JG, Zwemer RL, Chick AJ, Miller AE. A NEW METHOD FOR THE GENERATION

AND USE OF FOCUSED ULTRASOUND IN EXPERIMENTAL BIOLOGY. The Journal of General Physiology 1942;26:179–193.

[10]Therapeutic Ultrasound. Springer-Verlag GmbH, 2015. URL https://www.ebook.de/de/product/25161978/therapeutic_ultrasound.html.

[11]Clement GT, Sun J, Giesecke T, Hynynen K. A hemisphere array for non-invasive ultrasound brain therapy and surgery. Physics in Medicine and Biology 2000;45:3707–3719.

[12]Hynynen K, Clement GT, McDannold N, Vykhodtseva N, King R, White PJ, Vitek S, Jolesz FA. 500-element ultrasound phased array system for noninvasive focal surgery of the brain: A preliminary rabbit study with ex vivo human skulls. Magnetic Resonance in Medicine 2004; 52:100–107.

[13]Rieke V, Pauly KB. MR thermometry. J Magn Reson Imaging 2008;27:376–390.

[14]Odéen H, Parker DL. Magnetic resonance thermometry and its biological applications – physical principles and practical considerations. Progress in Nuclear Magnetic Resonance Spectroscopy 2019;110:34–61.

[15]MRI-Guided Focused Ultrasound Surgery. Taylor & Francis Inc, 2007. URL https://www.ebook.de/de/product/6647250/mri_guided_focused_ultrasound_surgery.html.

[16]Eames MDC, Hananel A, Kassell NF, Snell JW. Intracranial treatment envelope mapping of transcranial focused ultrasound. AIP, 2012; .

[17]Monteith S, Sheehan J, Medel R, Wintermark M, Eames M, Snell J, Kassell NF, Elias WJ. Potential intracranial applications of magnetic resonance–guided focused ultrasound surgery. Journal of Neurosurgery 2013;118:215–221.

[18]Odéen H, de Bever J, Almquist S, Farrer A, Todd N, Payne A, Snell JW, Christensen DA, Parker DL. Treatment envelope evaluation in transcranial magnetic resonance-guided focused ultrasound utilizing 3d MR thermometry. Journal of Therapeutic Ultrasound 2014;2:19.

[19]Bloch F. Nuclear induction. Physical Review 1946;70:460–474.

[20]Nishimura DG. Principles of Magnetic Resonance Imaging.

[21]URL http://web.eecs.umich.edu/~dnoll/BME516/mri1.pdf.

[22]Bernstein MA, King KF, Zhou XJ. Handbook of MRI pulse sequences. Massachusetts: Academic Press; 2004. 1040 p.

[23]Comprehensive Biomedical Physics. Elsevier, 2014. URL https://www.amazon.com/Comprehensive-Biomedical-Physics-Anders-Brahme/dp/0444536329?SubscriptionId=AKIAIOBINVZYXZQZ2U3A&tag=chimbori05-20&linkCode=xm2&camp=2025&creative=165953&creativeASIN=0444536329.

[24]Thomas L (Research Professor BUMAUS Department of Biomedical Engineering. Diagnostic Ultrasound Imaging: Inside Out. Elsevier Science Publishing Co Inc, 2013. URL https://www.ebook.de/de/product/18809997/thomas_l_research_professor_department_of_biomedical_engineering_boston_university_ma_usa_szabo_diagnostic_ultrasound_imaging_inside_out.html.

[25]Physical Properties of Tissues. Elsevier, 1990.

[26]URL https://www.fda.gov/media/71100/download.

[27]Wells P. Absorption and dispersion of ultrasound in biological tissue. Ultrasound in Medicine & Biology 1975;1:369–376.

[28]Goss S, Frizzell L, Dunn F. Ultrasonic absorption and attenuation in mammalian tissues. Ultrasound in Medicine & Biology 1979;5:181–186.

[29]Sapareto SA, Dewey WC. Thermal dose determination in cancer therapy. International Journal of Radiation Oncology Biology Physics 1984;10:787–800.

[30]Yarmolenko PS, Moon EJ, Landon C, Manzoor A, Hochman DW, Viglianti BL, Dewhirst MW. Thresholds for thermal damage to normal tissues: An update. International Journal of Hyperthermia 2011;27:320–343.

[31]Apfel RE. 7. acoustic cavitation. In Methods in Experimental Physics, Elsevier, pp. 355–411. 1981;.

[32]Apfel RE. Acoustic cavitation: a possible consequence of biomedical uses of ultrasound. The British journal of cancer Supplement 1982;5:140–146.

[33]McDannold N, Vykhodtseva N, Hynynen K. Targeted disruption of the blood–brain barrier with focused ultrasound: association with cavitation activity. Physics in Medicine and Biology 2006; 51:793–807.

[34]Flynn HG. Generation of transient cavities in liquids by microsecond pulses of ultrasound. The Journal of the Acoustical Society of America 1982;72:1926–1932.

[35]Apfel RE, Holland CK. Gauging the likelihood of cavitation from short-pulse, low-duty cycle diagnostic ultrasound. Ultrasound in Medicine & Biology 1991;17:179–185.

[36]Vykhodtseva N, Hynynen K, Damianou C. Histologic effects of high intensity pulsed ultrasound exposure with subharmonic emission in rabbit brain in vivo. Ultrasound in Medicine & Biology 1995;21:969–979.

[37]McDannold NJ, Vykhodtseva NI, Hynynen K. Microbubble contrast agent with focused ultrasound to create brain lesions at low power levels: MR imaging and histologic study in rabbits. Radiology 2006;241:95–106.

[38]Torr GR. The acoustic radiation force. American Journal of Physics 1984;52:402–408.

[39]Starritt HC, Duck FA, Humphrey VF. Forces acting in the direction of propagation in pulsed ultrasound fields. Physics in Medicine and Biology 1991;36:1465–1474.

[40]Nightingale KR, Palmeri ML, Nightingale RW, Trahey GE. On the feasibility of remote palpation using acoustic radiation force. The Journal of the Acoustical Society of America 2001;110:625–634.

[41]Moises Levy RS Henry Bass. Handbook of Elastic Properties of Solids, Liquids, and Gases, Four-Volume Set.

[42]Nightingale K, Soo MS, Nightingale R, Trahey G. Acoustic radiation force impulse imaging: in vivo demonstration of clinical feasibility. Ultrasound in Medicine & Biology 2002;28:227–235.

[43]Urban M, Bernal M, Greenleaf J. Phase aberration correction using ultrasound radiation force and vibrometry optimization. IEEE Transactions on Ultrasonics, Ferroelectrics and Frequency Control 2007;54:1142–1153.

[44]Callé S, Remenieras JP, Matar OB, Hachemi ME, Patat F. Temporal analysis of tissue displacement induced by a transient ultrasound radiation force. The Journal of the Acoustical Society of America 2005;118:2829–2840.

[45]Palmeri M, Sharma A, Bouchard R, Nightingale R, Nightingale K. A finite-element method model of soft tissue response to impulsive acoustic radiation force. IEEE Transactions on Ultrasonics, Ferroelectrics and Frequency Control 2005;52:1699–1712.

[46]Palmeri ML, Nightingale KR. Acoustic radiation force-based elasticity imaging methods. Interface Focus 2011;1:553–564.

[47]Sarvazyan AP, Rudenko OV, Swanson SD, Fowlkes J, Emelianov SY. Shear wave elasticity imaging: a new ultrasonic technology of medical diagnostics. Ultrasound in Medicine & Biology 1998;24:1419–1435.

[48]Fry FJ, Barger JE. Acoustical properties of the human skull. The Journal of the Acoustical Society of America 1978;63:1576–1590.

[49]Pinton G, Aubry JF, Bossy E, Muller M, Pernot M, Tanter M. Attenuation, scattering, and absorption of ultrasound in the skull bone. Medical Physics 2011;39:299–307.

[50]Pulkkinen A, Werner B, Martin E, Hynynen K. Numerical simulations of clinical focused ultrasound functional neurosurgery. Physics in Medicine and Biology 2014;59:1679–1700.

[51]Vyas U, Ghanouni P, Halpern CH, Elias J, Pauly KB. Predicting variation in subject thermal response during transcranial magnetic resonance guided focused ultrasound surgery: Comparison in seventeen subject datasets. Medical Physics 2016;43:5170–5180.

[52]Schwartz ML, Yeung R, Huang Y, Lipsman N, Krishna V, Jain JD, Chapman MG, Lozano AM, Hynynen K. Skull bone marrow injury caused by MR-guided focused ultrasound for cerebral functional procedures. Journal of Neurosurgery 2019;130:758–762.

[53]Hughes A, Huang Y, Schwartz ML, Hynynen K. The reduction in treatment efficiency at high acoustic powers during MR -guided transcranial focused ultrasound thalamotomy for essential tremor. Medical Physics 2018;45:2925–2936.

[54]Ghanouni P, Pauly KB, Elias WJ, Henderson J, Sheehan J, Monteith S, Wintermark M. Transcranial MRI-guided focused ultrasound: A review of the technologic and neurologic applications. American Journal of Roentgenology 2015;205:150–159.

[55]Chang WS, Jung HH, Zadicario E, Rachmilevitch I, Tlusty T, Vitek S, Chang JW. Factors associated with successful magnetic resonance-guided focused ultrasound treatment: efficiency of acoustic energy delivery through the skull. Journal of Neurosurgery 2016;124:411–416.

[56]Boutet A, Gwun D, Gramer R, Ranjan M, Elias GJB, Tilden D, Huang Y, Li SX, Davidson B, Lu H, Tyrrell P, Jones RM, Fasano A, Hynynen K, Kucharczyk W, Schwartz ML, Lozano AM. The relevance of skull density ratio in selecting candidates for transcranial MR-guided focused ultrasound. Journal of Neurosurgery 2019;pp. 1–7.

[57]D'Souza M, Chen KS, Rosenberg J, Elias WJ, Eisenberg HM, Gwinn R, Taira T, Chang JW, Lipsman N, Krishna V, Igase K, Yamada K, Kishima H, Cosgrove R, Rumià J, Kaplitt MG, Hirabayashi H, Nandi D, Henderson JM, Pauly KB, Dayan M, Halpern CH, Ghanouni P. Impact of skull density ratio on efficacy and safety of magnetic resonance–guided focused ultrasound treatment of essential tremor. Journal of Neurosurgery 2019;pp. 1–6.

[58]Pouratian N, Baltuch G, Elias WJ, Gross R. American society for stereotactic and functional neurosurgery position statement on magnetic resonance-guided focused ultrasound for the management of essential tremor. Neurosurgery 2019;.

[59]Pinton G, Aubry JF, Fink M, Tanter M. Numerical prediction of frequency dependent 3d maps of mechanical index thresholds in ultrasonic brain therapy. Medical Physics 2011;39:455–467.

[60]Fry FJ, Goss SA. Further studies of the transkull transmission of an intense focused ultrasonic beam: Lesion production at 500 kHz. Ultrasound in Medicine & Biology 1980;6:33–38.

[61]Xu Z, Carlson C, Snell J, Eames M, Hananel A, Lopes MB, Raghavan P, Lee CC, Yen CP, Schlesinger D, Kassell NF, Aubry JF, Sheehan J. Intracranial inertial cavitation threshold and thermal ablation lesion creation using MRI-guided 220-kHz focused ultrasound surgery: preclinical investigation. Journal of Neurosurgery 2015;122:152–161.

[62]Lu JY, Zou H, Greenleaf JF. Biomedical ultrasound beam forming. Ultrasound in Medicine & Biology 1994;20:403–428.

[63]Sun J, Hynynen K. The potential of transskull ultrasound therapy and surgery using the maximum available skull surface area. The Journal of the Acoustical Society of America 1999;105:2519–2527.

[64]Connor C, Hynynen K. Patterns of thermal deposition in the skull during transcranial focused ultrasound surgery. IEEE Transactions on Biomedical Engineering 2004;51:1693–1706.

[65]McDannold N, Clement GT, Black P, Jolesz F, Hynynen K. Transcranial magnetic resonance imaging– guided focused ultrasound surgery of brain tumors. Neurosurgery 2010;66:323–332.

[66]FDA. P150038Cpdf ;.

[67]White P, Clement G, Hynynen K. Longitudinal and shear mode ultrasound propagation in human skull bone. Ultrasound in Medicine & Biology 2006;32:1085–1096.

[68]Park TY, Pahk KJ, Kim H. Method to optimize the placement of a single-element transducer for transcranial focused ultrasound. Computer Methods and Programs in Biomedicine 2019; 179:104982.

[69]Ebbini E, Cain C. Multiple-focus ultrasound phased-array pattern synthesis: optimal driving-signal distributions for hyperthermia. IEEE Transactions on Ultrasonics, Ferroelectrics and Frequency Control 1989;36:540–548.

[70]Fan X, Hynynen K. Ultrasound surgery using multiple sonications—treatment time considerations. Ultrasound in Medicine & Biology 1996;22:471–482.

[71]Hertzberg Y, Naor O, Volovick A, Shoham S. Towards multifocal ultrasonic neural stimulation: pattern generation algorithms. Journal of Neural Engineering 2010;7:056002.

[72]Monteith SJ, Medel R, Kassell NF, Wintermark M, Eames M, Snell J, Zadicario E, Grinfeld J, Sheehan JP, Elias WJ. Transcranial magnetic resonance–guided focused ultrasound surgery for trigeminal neuralgia: a cadaveric and laboratory feasibility study. Journal of Neurosurgery 2013; 118:319–328.

[73]Hindman JC. Proton resonance shift of water in the gas and liquid states. The Journal of Chemical Physics 1966;44:4582–4592.

[74]Ishihara Y, Calderon A, Watanabe H, Okamoto K, Suzuki Y, Kuroda K, Suzuki Y. A precise and fast temperature mapping using water proton chemical shift. Magnetic Resonance in Medicine 1995;34:814–823.

[75]McDannold N. Quantitative MRI-based temperature mapping based on the proton resonant frequency shift: Review of validation studies. International Journal of Hyperthermia 2005;21:533–546.

[76]McDannold N, Maier SE. Magnetic resonance acoustic radiation force imaging. Medical Physics 2008;35:3748–3758.

[77]Huang Y, Curiel L, Kukic A, Plewes DB, Chopra R, Hynynen K. MR acoustic radiation force imaging: In vivo comparison to ultrasound motion tracking. Medical Physics 2009;36:2016–2020.

[78]Kaye EA, Chen J, Pauly KB. Rapid MR-ARFI method for focal spot localization during focused ultrasound therapy. Magnetic Resonance in Medicine 2010;65:738–743.

[79]Paquin R, Vignaud A, Marsac L, Younan Y, Lehéricy S, Tanter M, Aubry JF. Keyhole acceleration for magnetic resonance acoustic radiation force imaging (MR ARFI). Magnetic Resonance Imaging 2013;31:1695–1703.

[80]Ilovitsh A, Fite BZ, Ilovitsh T, Ferrara KW. Acoustic radiation force imaging using a single-shot spiral readout. Physics in Medicine & Biology 2019;64:125004.

[81]Chen J, Watkins R, Pauly KB. Optimization of encoding gradients for MR-ARFI. Magnetic Resonance in Medicine 2010;63:1050–1058.

[82]Kaye EA, Pauly KB. Adapting MRI acoustic radiation force imaging for in vivo human brain focused ultrasound applications. Magnetic Resonance in Medicine 2012;69:724–733.

[83]Mougenot C, Waspe A, Looi T, Drake JM. Variable ultrasound trigger delay for improved magnetic resonance acoustic radiation force imaging. Physics in Medicine and Biology 2015;61:712–727.

[84]Dadakova T, Krafft AJ, Özen AC, Bock M. Optimization of acoustic radiation force imaging: Influence of timing parameters on sensitivity. Magnetic Resonance in Medicine 2017;79:981–986.

[85]Zheng Y, Marx M, Miller GW, Pauly KB. High sensitivity MR acoustic radiation force imaging using transition band balanced steady-state free precession. Magnetic Resonance in Medicine 2017;79:1532–1537.

[86]de Bever JT, Odéen H, Todd N, Farrer AI, Parker DL. Evaluation of a three-dimensional MR acoustic radiation force imaging pulse sequence using a novel unbalanced bipolar motion encoding gradient. Magnetic Resonance in Medicine 2015;76:803–813.

[87]Odéen H, de Bever J, Hofstetter LW, Parker DL. Multiple-point magnetic resonance acoustic radiation force imaging. Magnetic Resonance in Medicine 2018;81:1104–1117.

[88]Auboiroux V, Viallon M, Roland J, Hyacinthe JN, Petrusca L, Morel DR, Goget T, Terraz S, Gross P, Becker CD, Salomir R. ARFI-prepared MRgHIFU in liver: Simultaneous mapping of ARFI-displacement and temperature elevation, using a fast GRE-EPI sequence. Magnetic Resonance in Medicine 2012;68:932–946.

[89]de Bever JT, Odéen H, Hofstetter LW, Parker DL. Simultaneous MR thermometry and acoustic radiation force imaging using interleaved acquisition. Magnetic Resonance in Medicine 2017; 79:1515–1524.

[90]Bour P, Marquet F, Ozenne V, Toupin S, Dumont E, Aubry JF, Lepetit-Coiffe M, Quesson B. Real-time monitoring of tissue displacement and temperature changes during MR-guided high intensity focused ultrasound. Magnetic Resonance in Medicine 2017;78:1911–1921.

[91]Larrat B, Pernot M, Aubry JF, Dervishi E, Sinkus R, Seilhean D, Marie Y, Boch AL, Fink M, Tanter M. MR-guided transcranial brain HIFU in small animal models. Physics in Medicine and Biology 2009;55:365–388.

[92]Dervishi E, Larrat B, Pernot M, Adam C, Marie Y, Fink M, Delattre JY, Boch AL, Tanter M, Aubry JF. Transcranial high intensity focused ultrasound therapy guided by 7 TESLA MRI in a rat brain tumour model: A feasibility study. International Journal of Hyperthermia 2013; 29:598–608.

[93]Hertzberg Y, Volovick A, Zur Y, Medan Y, Vitek S, Navon G. Ultrasound focusing using magnetic resonance acoustic radiation force imaging: Application to ultrasound transcranial therapy. Medical Physics 2010;37:2934–2942.

[94]Ozenne V, Constans C, Bour P, Santin MD, Valabrègue R, Ahnine H, Pouget P, Lehéricy S, Aubry JF, Quesson B. MRI monitoring of temperature and displacement for transcranial focus ultrasound applications. NeuroImage 2020;204:116236.

[95]Phipps MA, Jonathan SV, Yang PF, Chaplin V, Chen LM, Grissom WA, Caskey CF. Considerations for ultrasound exposure during transcranial MR acoustic radiation force imaging. Scientific Reports 2019;9.

[96]Chaplin V, Phipps MA, Jonathan SV, Grissom WA, Yang PF, Chen LM, Caskey CF. On the accuracy of optically tracked transducers for image-guided transcranial ultrasound. International Journal of Computer Assisted Radiology and Surgery 2019;14:1317–1327.

[97]Lipsman N, Schwartz ML, Huang Y, Lee L, Sankar T, Chapman M, Hynynen K, Lozano AM. MR-guided focused ultrasound thalamotomy for essential tremor: a proof-of-concept study. Lancet Neurol 2013;12:462–468.

[98]Köhler MO, Mougenot C, Quesson B, Enholm J, Le Bail B, Laurent C, Moonen CT, Ehnholm GJ. Volumetric HIFU ablation under 3D guidance of rapid MRI thermometry. Med Phys 2009; 36:3521–3535.

[99]Todd N, Vyas U, de Bever J, Payne A, Parker DL. Reconstruction of fully three-dimensional high spatial and temporal resolution MR temperature maps for retrospective applications. Magn Reson Med 2012;67:724–730.

[100]Marx M, Plata J, Pauly KB. Toward volumetric MR thermometry with the MASTER sequence. IEEE Trans Med Imaging 2015;34:148–155.

[101]Mulkern RV, Panych LP, Hynynen K, Jolesz FA, McDannold NJ. Tissue temperature monitoring with multiple gradient-echo imaging sequences. J Magn Reson Imaging 1998;8:493–502.

[102]Todd N, Diakite M, Payne A, Parker DL. In vivo evaluation of multi-echo hybrid PRF/T1 approach for temperature monitoring during breast MR-guided focused ultrasound surgery treatments. Magn Reson Med 2014;72:793–799.

[103]Marx M, Pauly KB. Improved MRI thermometry with multiple-echo spirals. Magn Reson Med 2016;76:747–756.

[104]Marx M, Ghanouni P, Pauly KB. Specialized volumetric thermometry for improved guidance of MRgFUS in brain. Magn Reson Med 2016. doi: 10.1002/mrm.26385.

[105]Fielden SW, Feng X, Zhao L, Miller GW, Geeslin M, Dallapiazza RF, Elias WJ, Wintermark M, Pauly KB, Meyer CH. A spiral-based volumetric acquisition for MR temperature imaging. Magnetic Resonance in Medicine 2017;79:3122–3127.

[106]Grissom WA, Allen S. Reducing temperature errors in transcranial MR-guided focused ultrasound using a reduced-field-of-view sequence. Magnetic Resonance in Medicine 2019;83:1016–1024.

[107]Todd N, Adluru G, Payne A, DiBella EV, Parker D. Temporally constrained reconstruction applied to MRI temperature data. Magn Reson Med 2009;62:406–419.

[108]Todd N, Payne A, Parker DL. Model predictive filtering for improved temporal resolution in MRI temperature imaging. Magn Reson Med 2010;63:1269–1279.

[109]Roujol S, Ries M, Quesson B, Moonen C, de Senneville BD. Real-time MR-thermometry and dosimetry for interventional guidance on abdominal organs. Magn Reson Med 2010;63:1080–1087.

[110]Todd N, Prakash J, Odéen H, de Bever J, Payne A, Yalavarthy P, Parker DL. Toward real-time availability of 3D temperature maps created with temporally constrained reconstruction. Magn Reson Med 2014;71:1394–1404.

[111]Gaur P, Grissom WA. Accelerated MRI thermometry by direct estimation of temperature from undersampled k-space data. Magn Reson Med 2015;73:1914–1925.

[112]Cao Z, Gore JC, Grissom WA. Low-rank plus sparse compressed sensing for accelerated proton resonance frequency shift MR temperature imaging. Magnetic Resonance in Medicine 2019; 81:3555–3566.

[113]Quah K, Poorman ME, Allen SP, Grissom WA. Simultaneous multislice MRI thermometry with a single coil using incoherent blipped-controlled aliasing. Magnetic Resonance in Medicine 2019; 83:479–491.

[114]Jonathan SV, Grissom WA. Volumetric MRI thermometry using a three-dimensional stack-of-stars echo-planar imaging pulse sequence. Magnetic Resonance in Medicine 2017;79:2003–2013.

[115]Svedin BT, Payne A, Parker DL. Simultaneous proton resonance frequency shift thermometry and t 1 measurements using a single reference variable flip angle t 1 method. Magnetic Resonance in Medicine 2019;81:3138–3152.

[116]Zhang L, Armstrong T, Li X, Wu HH. A variable flip angle golden-angle-ordered 3d stack-of-radial MRI technique for simultaneous proton resonant frequency shift and t 1 -based thermometry. Magnetic Resonance in Medicine 2019;82:2062–2076.

[117]Fry WJ, Mosberg WH, Barnard JW, Fry FJ. Production of focal destructive lesions in the central nervous system with ultrasound. Journal of Neurosurgery 1954;11:471–478.

[118]Fink M. Time reversal of ultrasonic fields. i. basic principles. IEEE Transactions on Ultrasonics, Ferroelectrics and Frequency Control 1992;39:555–566.

[119]Thomas JL, Fink M. Ultrasonic beam focusing through tissue inhomogeneities with a time reversal mirror: application to transskull therapy. IEEE Transactions on Ultrasonics, Ferroelectrics and Frequency Control 1996;43:1122–1129.

[120]Clement G, Hynynen K. Micro-receiver guided transcranial beam steering. IEEE Transactions on Ultrasonics, Ferroelectrics and Frequency Control 2002;49:447–453.

[121]Hynynen K, Jolesz FA. Demonstration of potential noninvasive ultrasound brain therapy through an intact skull. Ultrasound in Medicine & Biology 1998;24:275–283.

[122]Pernot M, Aubry JF, Tanter M, Boch AL, Marquet F, Kujas M, Seilhean D, Fink M. In vivo transcranial brain surgery with an ultrasonic time reversal mirror. Journal of Neurosurgery 2007; 106:1061–1066.

[123]Clement G, Hynynen K. Correlation of ultrasound phase with physical skull properties. Ultrasound in Medicine & Biology 2002;28:617–624.

[124]Jones RM, Hynynen K. Comparison of analytical and numerical approaches for CT-based aberration correction in transcranial passive acoustic imaging. Physics in Medicine and Biology 2015; 61:23–36.

[125]Clement GT, Hynynen K. A non-invasive method for focusing ultrasound through the human skull. Physics in Medicine and Biology 2002;47:1219–1236.

[126]Aubry JF, Tanter M, Pernot M, Thomas JL, Fink M. Experimental demonstration of noninvasive transskull adaptive focusing based on prior computed tomography scans. The Journal of the Acoustical Society of America 2003;113:84–93.

[127]Marquet F, Pernot M, Aubry JF, Montaldo G, Marsac L, Tanter M, Fink M. Non-invasive transcranial ultrasound therapy based on a 3d CT scan: protocol validation andin vitroresults. Physics in Medicine and Biology 2009;54:2597–2613.

[128]Kyriakou A, Neufeld E, Werner B, Székely G, Kuster N. Full-wave acoustic and thermal modeling of transcranial ultrasound propagation and investigation of skull-induced aberration correction techniques: a feasibility study. Journal of Therapeutic Ultrasound 2015;3.

[129]Treeby BE, Cox BT. k-wave: MATLAB toolbox for the simulation and reconstruction of photoacoustic wave fields. Journal of Biomedical Optics 2010;15:021314.

[130]Robertson JLB, Cox BT, Jaros J, Treeby BE. Accurate simulation of transcranial ultrasound propagation for ultrasonic neuromodulation and stimulation. The Journal of the Acoustical Society of America 2017;141:1726–1738.

[131]Vyas U, Christensen D. Ultrasound beam simulations in inhomogeneous tissue geometries using the hybrid angular spectrum method. IEEE Transactions on Ultrasonics, Ferroelectrics and Frequency Control 2012;59:1093–1100.

[132]Almquist S, Parker DL, Christensen DA. Rapid full-wave phase aberration correction method for transcranial high-intensity focused ultrasound therapies. Journal of Therapeutic Ultrasound 2016;4.

[133]Leung SA, Webb TD, Bitton RR, Ghanouni P, Pauly KB. A rapid beam simulation framework for transcranial focused ultrasound. Scientific Reports 2019;9.

[134]McDannold N, White PJ, Cosgrove R. Elementwise approach for simulating transcranial MRI-guided focused ultrasound thermal ablation. Physical Review Research 2019;1.

[135]Hynynen K, Sun J. Trans-skull ultrasound therapy: the feasibility of using image-derived skull thickness information to correct the phase distortion. IEEE Transactions on Ultrasonics, Ferroelectrics and Frequency Control 1999;46:752–755.

[136]Miller GW, Eames M, Snell J, Aubry JF. Ultrashort echo-time MRI versus CT for skull aberration correction in MR-guided transcranial focused ultrasound: In vitro comparison on human calvaria. Medical Physics 2015;42:2223–2233.

[137]Caballero-Insaurriaga J, Rodríguez-Rojas R, Martínez-Fernández R, Del-Alamo M, Díaz-Jiménez L, Ávila M, Martínez-Rodrigo M, García-Polo P, Pineda-Pardo JA. Zero TE MRI applications

to transcranial MR-guided focused ultrasound: Patient screening and treatment efficiency estimation. Journal of Magnetic Resonance Imaging 2019;50:1583–1592.

[138]Guo S, Zhuo J, Li G, Gandhi D, Dayan M, Fishman P, Eisenberg H, Melhem ER, Gullapalli RP. Feasibility of ultrashort echo time images using full-wave acoustic and thermal modeling for transcranial MRI-guided focused ultrasound (tcMRgFUS) planning. Physics in Medicine & Biology 2019;64:095008.

[139]Herbert E, Pernot M, Montaldo G, Fink M, Tanter M. Energy-based adaptive focusing of waves: application to noninvasive aberration correction of ultrasonic wavefields. IEEE Transactions on Ultrasonics, Ferroelectrics, and Frequency Control 2009;56:2388–2399.

[140]White J, Clement G, Hynynen K. Transcranial ultrasound focus reconstruction with phase and amplitude correction. IEEE Transactions on Ultrasonics, Ferroelectrics and Frequency Control 2005;52:1518–1522.

[141]Larrat B, Pernot M, Montaldo G, Fink M, Tanter M. MR-guided adaptive focusing of ultrasound. IEEE Transactions on Ultrasonics, Ferroelectrics and Frequency Control 2010;57:1734–1747.

[142]Marsac L, Chauvet D, Larrat B, Pernot M, Robert B, Fink M, Boch AL, Aubry JF, Tanter M. MR-guided adaptive focusing of therapeutic ultrasound beams in the human head. Medical Physics 2012;39:1141–1149.

[143]Kaye EA, Hertzberg Y, Marx M, Werner B, Navon G, Levoy M, Pauly KB. Application of zernike polynomials towards accelerated adaptive focusing of transcranial high intensity focused ultrasound. Medical Physics 2012;39:6254–6263.

[144]Liu N, Liutkus A, Aubry JF, Marsac L, Tanter M, Daudet L. Random calibration for accelerating MR-ARFI guided ultrasonic focusing in transcranial therapy. Physics in Medicine and Biology 2015;60:1069–1085.

[145]Mougenot C, Pichardo S, Engler S, Waspe A, Colas EC, Drake JM. A rapid magnetic resonance acoustic radiation force imaging sequence for ultrasonic refocusing. Physics in Medicine and Biology 2016;61:5724–5740.

[146]Vyas U, Kaye E, Pauly KB. Transcranial phase aberration correction using beam simulations and MR-ARFI. Medical Physics 2014;41:032901.

[147]Webb TD, Leung SA, Rosenberg J, Ghanouni P, Dahl JJ, Pelc NJ, Pauly KB. Measurements of the relationship between CT hounsfield units and acoustic velocity and how it changes with photon energy and reconstruction method. IEEE Transactions on Ultrasonics, Ferroelectrics, and Frequency Control 2018;65:1111–1124.

[148]Robertson J, Martin E, Cox B, Treeby BE. Sensitivity of simulated transcranial ultrasound fields to acoustic medium property maps. Physics in Medicine and Biology 2017;62:2559–2580.

[149]Robertson J, Urban J, Stitzel J, Treeby BE. The effects of image homogenisation on simulated transcranial ultrasound propagation. Physics in Medicine & Biology 2018;63:145014.

[150]Kobus T, McDannold N. Update on clinical magnetic resonance-guided focused ultrasound applications. Magn Reson Imaging Clin N Am 2015;23:657–667.

[151]Tempany CMC, Stewart EA, McDannold N, Quade BJ, Jolesz FA, Hynynen K. MR imaging-guided focused ultrasound surgery of uterine leiomyomas: a feasibility study. Radiology 2003; 226:897–905.

[152]Catane R, Beck A, Inbar Y, Rabin T, Shabshin N, Hengst S, Pfeffer R, Hanannel A, Dogadkin O, Liberman B, et al. MR-guided focused ultrasound surgery (MRgFUS) for the palliation of pain in patients with bone metastases–preliminary clinical experience. Ann Oncol 2006;18:163–167.

[153]Hynynen K, Pomeroy O, Smith DN, Huber PE, McDannold NJ, Kettenbach J, Baum J, Singer S, Jolesz FA. MR imaging-guided focused ultrasound surgery of fibroadenomas in the breast: a feasibility study. Radiology 2001;219:176–185.

[154]McDannold N, Clement GT, Black P, Jolesz F, Hynynen K. Transcranial magnetic resonance imaging-guided focused ultrasound surgery of brain tumors: initial findings in 3 patients. Neurosurgery 2010;66:323–332.

[155]Chopra R, Colquhoun A, Burtnyk M, N'djin WA, Kobelevskiy I, Boyes A, Siddiqui K, Foster H, Sugar L, Haider MA, et al. MR imaging-controlled transurethral ultrasound therapy for

conformal treatment of prostate tissue: initial feasibility in humans. Radiology 2012;265:303–313.

[156]Martin E, Jeanmonod D, Morel A, Zadicario E, Werner B. High-intensity focused ultrasound for noninvasive functional neurosurgery. Ann Neurol 2009;66:858–861.

[157]Jeanmonod D, Werner B, Morel A, Michels L, Zadicario E, Schiff G, Martin E. Transcranial magnetic resonance imaging-guided focused ultrasound: noninvasive central lateral thalamotomy for chronic neuropathic pain. Neurosurg Focus 2012;32:E1.

[158]Elias WJ, Huss D, Voss T, Loomba J, Khaled M, Zadicario E, Frysinger RC, Sperling SA, Wylie S, Monteith SJ, et al. A pilot study of focused ultrasound thalamotomy for essential tremor. N Engl J Med 2013;369:640–8.

[159]Magara A, Bühler R, Moser D, Kowalski M, Pourtehrani P, Jeanmonod D. First experience with MR-guided focused ultrasound in the treatment of Parkinson's disease. J Ther Ultrasound 2014; 2:11.

[160]Monteith S, Sheehan J, Medel R, Wintermark M, Eames M, Snell J, Kassell NF, Elias WJ. Potential intracranial applications of magnetic resonance-guided focused ultrasound surgery. J Neurosurg 2013;118:215–21.

[161]Kinoshita M, McDannold N, Jolesz FA, Hynynen K. Noninvasive localized delivery of Herceptin to the mouse brain by MRI-guided focused ultrasound-induced blood-brain barrier disruption. Proc Natl Acad Sci U S A 2006;103:11719–23.

[162]Winkelmann S, Schaeffter T, Koehler T, Eggers H, Doessel O. An optimal radial profile order based on the golden ratio for time-resolved MRI. IEEE Trans Med Imaging 2007;26:68–76.

[163]Gaur P, Partanen A, Werner B, Ghanouni P, Bitton R, Pauly KB, Grissom WA. Correcting heat-induced chemical shift distortions in proton resonance frequency-shift thermometry. Magn Reson Med 2016;76:172–182.

[164]McNab JA, Gallichan D, Miller KL. 3D steady-state diffusion-weighted imaging with trajectory using radially batched internal navigator echoes (TURBINE). Magn Reson Med 2010;63:235–242.

[165]Jonathan SV, Vakil P, Jeong YI, Menon RG, Ansari SA, Carroll TJ. RAZER: A pulse sequence for whole-brain bolus tracking at high frame rates. Magn Reson Med 2014;71:2127–2138.

[166]Graedel NN, McNab JA, Chiew M, Miller KL. Motion correction for functional MRI with three-dimensional hybrid radial-Cartesian EPI. Magn Reson Med 2016;13:333–43.

[167]Shrestha M, Mildner T, Schlumm T, Robertson SH, Möller H. Three-dimensional echo-planar cine imaging of cerebral blood supply using arterial spin labeling. MAGMA 2016;29:799–810.

[168]Stäb D, Bollmann S, Langkammer C, Bredies K, Barth M. Accelerated mapping of magnetic susceptibility using 3D planes-on-a-paddlewheel (POP) EPI at ultra-high field strength. NMR Biomed 2016. doi: 10.1002/nbm.3620.

[169]Pruessmann KP, Weiger M, Börnert P, Boesiger P. Advances in sensitivity encoding with arbitrary k-space trajectories. Magn Reson Med 2001;46:638–651.

[170]Grissom WA, Rieke V, Holbrook AB, Medan Y, Lustig M, Santos J, McConnell MV, Pauly KB. Hybrid referenceless and multibaseline subtraction MR thermometry for monitoring thermal therapies in moving organs. Med Phys 2010;37:5014–5026.

[171]Rieke V, Instrella R, Rosenberg J, Grissom W, Werner B, Martin E, Pauly KB. Comparison of temperature processing methods for monitoring focused ultrasound ablation in the brain. J Magn Reson Imaging 2013;38:1462–1471.

[172]Jonathan SV, Grissom WA. High-resolution whole-brain MR thermometry with a 3D EPI stack-of-stars pulse sequence. In Proceedings of the 5th International Symposium on Focused Ultrasound, North Bethesda, MD, USA, 2016. p. 8.

[173]Vakil P, Ansari SA, Hurley MC, Bhat H, Batjer HH, Bendok BR, Eddleman CS, Carroll TJ. Magnetization spoiling in radial FLASH contrast-enhanced MR digital subtraction angiography. J Magn Reson Imaging 2012;36:249–258.

[174]Schmitt F, Stehling MK, Turner R. Echo-planar imaging: theory technique and application. Berlin, Heidelberg: Springer; 1998. 662 p.

[175]Fessler J, Sutton B. Nonuniform fast fourier transforms using min-max interpolation. IEEE Trans Signal Process 2003;51:560–574.

[176]Buehrer M, Pruessmann KP, Boesiger P, Kozerke S. Array compression for MRI with large coil arrays. Magn Reson Med 2007;57:1131–1139.

[177]Smith SM. Fast robust automated brain extraction. Hum Brain Mapp 2002;17:143–155.

[178]Griswold MA, Jakob PM, Heidemann RM, Nittka M, Jellus V, Wang J, Kiefer B, Haase A. Generalized autocalibrating partially parallel acquisitions (GRAPPA). Magn Reson Med 2002; 47:1202–1210.

[179]Deshmane A, Blaimer M, Breuer F, Jakob PM, Duerk JL, Seiberlich N, Griswold MA. Self-calibrated trajectory estimation and signal correction method for robust radial imaging using GRAPPA operator gridding. Magn Reson Med 2016;75:883–896.

[180]Ianni JD, Grissom WA. Trajectory auto-corrected image reconstruction. Magn Reson Med 2016; 76:757–768.

[181]Svedin B, Parker D. Multi-echo Pseudo-Golden Angle Stack of Stars Thermometry with High Spatial and Temporal Resolution. In Proceedings of the 24th Annual Meeting of ISMRM, Singapore, 2016. Abstract number 816.

[182]Svedin B, Payne A, Parker D. In vivo evaluation of a multi-echo pseudo-golden angle stack of stars thermometry method. In Proceedings of the 25th Annual Meeting of ISMRM, Honolulu, HI, USA, 2017. Abstract number 5423.

[183]Innovative Neuromodulation. Elsevier Science Publishing Co Inc, 2017. URL https://www.ebook.de/de/product/28166292/innovative_neuromodulation.html.

[184]Deffieux T, Younan Y, Wattiez N, Tanter M, Pouget P, Aubry JF. Low-intensity focused ultrasound modulates monkey visuomotor behavior. Current Biology 2013;23:2430–2433.

[185]Naor O, Krupa S, Shoham S. Ultrasonic neuromodulation. Journal of Neural Engineering 2016; 13:031003.

[186]Yang PF, Phipps MA, Newton AT, Chaplin V, Gore JC, Caskey CF, Chen LM. Neuromodulation of sensory networks in monkey brain by focused ultrasound with MRI guidance and detection. Scientific Reports 2018;8.

[187]Fishman PS, Elias WJ, Ghanouni P, Gwinn R, Lipsman N, Schwartz M, Chang JW, Taira T, Krishna V, Rezai A, Yamada K, Igase K, Cosgrove R, Kashima H, Kaplitt MG, Tierney TS, Eisenberg HM. Neurological adverse event profile of magnetic resonance imaging-guided focused ultrasound thalamotomy for essential tremor. Movement Disorders 2018;33:843–847.

[188]Wang H, Wang B, Normoyle KP, Jackson K, Spitler K, Sharrock MF, Miller CM, Best C, Llano D, Du R. Brain temperature and its fundamental properties: a review for clinical neuroscientists. Frontiers in Neuroscience 2014;8.

[189]Kim H, Chiu A, Park S, Yoo SS. Image-guided navigation of single-element focused ultrasound transducer. International Journal of Imaging Systems and Technology 2012;22:177–184.

[190]Wu SY, Aurup C, Sanchez CS, Grondin J, Zheng W, Kamimura H, Ferrera VP, Konofagou EE. Efficient blood-brain barrier opening in primates with neuronavigation-guided ultrasound and real-time acoustic mapping. Scientific Reports 2018;8.

[191]Kyriakou A, Neufeld E, Werner B, Paulides MM, Szekely G, Kuster N. A review of numerical and experimental compensation techniques for skull-induced phase aberrations in transcranial focused ultrasound. International Journal of Hyperthermia 2013;30:36–46.

[192]Ackerman M. The visible human project. Proceedings of the IEEE 1998;86:504–511.

[193]Mueller JK, Ai L, Bansal P, Legon W. Numerical evaluation of the skull for human neuromodulation with transcranial focused ultrasound. Journal of Neural Engineering 2017;14:066012.

[194]Jenkinson M, Beckmann CF, Behrens TE, Woolrich MW, Smith SM. FSL. NeuroImage 2012; 62:782–790.

[195]Lozano AM, Lipsman N. Probing and regulating dysfunctional circuits using deep brain stimulation. Neuron 2013;77:406–424.

[196]Desikan RS, Ségonne F, Fischl B, Quinn BT, Dickerson BC, Blacker D, Buckner RL, Dale AM, Maguire RP, Hyman BT, Albert MS, Killiany RJ. An automated labeling system for subdividing the human cerebral cortex on MRI scans into gyral based regions of interest. NeuroImage 2006; 31:968–980.

[197]Chaplin V, Phipps MA, Caskey CF. A random phased-array for MR-guided transcranial ultrasound neuromodulation in non-human primates. Physics in Medicine & Biology 2018;63:105016.

[198]Pieper S, Halle M, Kikinis R. 3d slicer. In 2004 2nd IEEE International Symposium on Biomedical Imaging: Macro to Nano (IEEE Cat No. 04EX821). IEEE; .

[199]URL https://elki-project.github.io/tutorial/same-size_k_means.

[200]Payne A, de Bever J, Farrer A, Coats B, Parker DL, Christensen DA. A simulation technique for 3d MR-guided acoustic radiation force imaging. Medical Physics 2015;42:674–684.

[201]Leskovec J, Rajaraman A, Ullman JD. Mining of Massive Datasets. Cambridge University Pr., 2020. URL https://www.ebook.de/de/product/38122967/jure_leskovec_anand_rajaraman_jeffrey_david_ullman_mining_of_massive_datasets.html.